JAERI-M
83-028

EVALUATION REPORT ON CCTF CORE-I REFLOOD TESTS CI-17 (RUN 36) AND CI-20 (RUN 39)

—THERMALLY-MULTIDIMENSIONAL EFFECTS ON CORE THERMO-HYDRODYNAMICS—

February 1983

Yoshio MURAO and Tadashi IGUCHI

日本原子力研究所
Japan Atomic Energy Research Institute

JAERI-M レポートは，日本原子力研究所が不定期に公刊している研究報告書です。
入手の問合わせは，日本原子力研究所技術情報部情報資料課（〒319−11 茨城県那珂郡東海村）あて，お申しこしください。なお，このほかに財団法人原子力弘済会資料センター（〒319-11 茨城県那珂郡東海村日本原子力研究所内）で複写による実費頒布をおこなっております。

JAERI-M reports are issued irregularly.
Inquiries about availability of the reports should be addressed to Information Section, Division of Technical Information, Japan Atomic Energy Research Institute, Tokai-mura, Naka-gun, Ibaraki-ken 319-11, Japan.

編集兼発行　日本原子力研究所
印　　刷　山田軽印刷所

JAERI- M 83-028

Evaluation Report on CCTF Core-I Reflood Tests C1-17(Run 36) and C1-20(Run 39)

——— Thermally-multidimensional effects on core thermo-hydrodynamics ———

Yoshio MURAO and Tadashi IGUCHI

Division of Nuclear Safety Research,
Tokai Research Establishment, JAERI

(Received January 29, 1983)

In the safety analysis of the reflood phase of a PWR LOCA, the core thermo-hydrodynamic behavior is analyzed as a phenomena in a single channel core. In other words, the core thermo-hydrodynamic behavior is treated one-dimensionally.

In order to confirm the validity of the one-dimensional treatment, tests named Asymmetric power test C1-17(Run 36) and Asymmetric temperature test C1-20(Run 39) were performed, whose test conditions were similar to the base case test C1-5(Run 14) (the reference test for the parametric effect tests) except for the power distribution and the initial temperature distribution in core, respectively. First the results of the base case test were investigated. And the results of Asymmetric power test and Asymmetric temperature test were compared with the results of the base case test. The main conclusions are as follows:

(1) The water accumulation was observed along the whole core even above quench front almost simultaneously just after reflood initiation and almost terminated within 20 to 30 seconds. The flow pattern was recognized as a slug flow.

(2) In the lower two-thirds of the core, bottom quench was observed and the core water accumulation was one-dimensional even under the thermally asymmetric conditions.

The work was performed under Contract with the Atomic Energy Bureau of Science and Technology Agency of Japan.

(3) In the upper portion of the core, the multi-dimensional effect was observed, i.e. the top quench occurred locally.

(4) The water accumulation behavior or void fraction in the lower two-thirds of the core, i.e. our concerning region for the peak clad temperature analysis, and the core behavior for system analysis can be one-dimensionally analyzed with a representing single channel core.

Keywords: Reactor Safety, Reflood Experiment, Heat Transfer, Hydrodynamics, Loss-of-coolant Accident, Two-phase Flow, PWR

大型再冠水円筒第一次炉心試験 C1−17（Run 36），C1−20（Run 39）評価報告書 −炉心熱水力挙動に及ぼす熱的多次元効果−

日本原子力研究所東海研究所安全工学部
村尾　良夫・井口　　正

（1983年1月29日受理）

加圧水型原子炉（PWR）の冷却材喪失事故（LOCA）時の再冠水過程について安全解析を行う場合，炉心熱水力挙動は単一流路により構成された炉心内の現象として解析が行われている。云いかえれば，炉心熱水力挙動は一次元的に取扱われている。

一次元的取扱いの妥当性を確認するために，非対称出力試験C1−17（Run 36）と非対称温度試験C1−20（Run 39）と名付けられた試験を行った。それらの試験条件はそれぞれ炉心内の出力分布と初期温度分布を除き，パラメータ効果を調べるための参照用の試験である基準試験C1−5（Run 14）と同等であった。先ず，基準試験の結果を検討した。そして，非対称出力試験と非対称温度試験の結果を基準試験の結果と比較した。主要な結果は次の通りである。

(1) 再冠水開始直後に，クエンチフロントの上方を含む炉心全体にわたって，蓄水が生じた。そして，20〜30秒以内に水の蓄積が終了した。そしてこの流動様式をスラグ流であると判定した。

(2) 炉心下3分の2の部分では炉心下端からのクエンチが生じた。そして，この部分では，熱的に非対称な条件でも炉心内の蓄水は一次元的であった。

(3) 炉心のより上方の部分では多次元的な効果が現われ，炉心上端からのクエンチは局所的に生じた。

(4) 最高被覆管温度解析に対して注目している炉心下3分の2の部分では，蓄水挙動又はボイド率およびシステム解析に用いる炉心挙動を等価な単一流路により構成された炉心を用いて一次元的に解析することができる。

本報告書は，電源開発促進対策特別会計法に基づき，科学技術庁からの受託によって行った研究の成果である。

Contents

目　　次

List of tables

List of figures

I. Introduction

The objectives of this study are to confirm the validity of the one-dimensional treatment of the calculation on the core hydrodynamic behavior and the core cooling behavior.

In the safety analysis for the reflood phenomena of a PWR LOCA, the calculations of the system behavior and the hot rod temperature response are usually performed. In the system calculation, the system composed of the primary cooling system and the one-dimensional single channel core represented by the average power rod is usually used and obtained are the boundary conditions of the core, i.e. the core inlet mass flow rate, the core outlet mass flow rate, the core inlet temperature and the core inlet and outlet pressures. The obtained boundary conditions are fed to the calculation of the hot rod temperature response as inputs.

In this calculational procedure, the one-dimensional treatment of the core thermo-hydrodynamics is implicitly assumed to be valid or acceptable.

In order to confirm the validity of the assumption, some tests were performed in the Cylindrical Core Test Facility (CCTF) and the Slab Core Test Facility (SCTF). Both facilities have considerably large core and are the facilities of the Large Scale Reflood Test Program. The objectives of the program are:

(1) Demonstration of the safety margin in the current safety evaluation analysis on the effectiveness of the Emergency Core Cooling System (ECCS) in a PWR during the refill and the reflood phases of a LOCA of a PWR.

(2) Provision of information for analytical modeling of the related thermo-hydrodynamic phenomena.

(3) Verification of an integral reflood analysis, REFLA, and a US-developed reactor transient analysis code, TRAC.

In the previous analysis of a CCTF test[1], it was revealed that the temperature response and the water accumulation in the core are nearly axi-symmetric to the center axis of the core. Accordingly, the independency of the radial power of temperature distribution on the core water accumulation has to be shown for indicating the validity of the one-dimensional treatment of the core hydrodynamics. In SCTF tests[2] with the radial power distribution, the water accumulation was found to be radially flat before the quench occurred in the whole core.

Both the CCTF core and the SCTF core consist of two thousand heated rods, however the configurations of CCTF and SCTF are different from each other. The CCTF core is cylindrical and the radius of the core is shorter than that of a PWR. The SCTF core has slab configuration and the full scaled radius. However, the wetted perimeter of the surrounding wall of the SCTF core is longer than that of CCTF, accordingly the SCTF core has more significant wall effect. On the other hand, the CCTF core has a shortcoming that the radius is short. Another shortcoming of the CCTF core is that no differential pressure transducer is installed for measurement of the radial distribution of the core water accumulation. However the CCTF tests are believed to provide the realistic system and core behaviors, since CCTF integrally simulates a PWR system and the CCTF core has relatively large hydrodynamic equivalent diameter.

In order to overcome the shortcomings, the power distribution or the initial clad surface temperature distribution were azimuthally skewed in the following two multi-dimensional effect tests respectively:

(1) Asymmetric power test.

(2) Asymmetric temperature test.

Since the thermal core conditions were azimuthally skewed in these tests, the hydrodynamic conditions would be skewed azimuthally. Accordingly, the thermal effect can be sensed by the differential pressure transducer installed on the surrounding wall in the every ninety degree directions.

These two tests and the base case test with an azimuthally symmetric core conditions will be analyzed in this report on the view of the hydrodynamic behaviors in the core.

In CCTF, many thermocouples are installed on the clad surface and the information on the thermal conditions over the whole core can be obtained, whereas the information on the hydrodynamic conditions is limited because of limited number of core differential pressure transducers. In order to overcome this shortcomings, the following heat transfer coefficient correlation for the saturated film boiling is referred:[7]

$$h = 0.94\,[\lambda_g^{\,3}\,\rho_g\,\rho_\ell\,H_{fg}/L_g\,\mu_g\,\Delta T_{sat}]^{1/4}\,(1-\alpha)^{1/4} + E\varepsilon(1-\alpha)^{1/2}\,(T_W^4 - T_{sat}^4)/\Delta T_{sat} \quad . \qquad (1)$$

This correlation was developed for the slug flow by Murao and Sugimoto by using the data of the small scale reflood experiment. Since the radiation term (the second term of the right hand side of Eq. (1)) is small near the quenching period, the heat transfer coefficient is a function of the void fraction α and the distance from the quench front L_q. Accordingly, it can be inferred that the void fraction is uniform at the same elevation when (1) the flow is the slug flow and (2) the quench front propagation and (3) the heat transfer coefficient are uniform at the same elevation.

II. Experiment

1. Apparatus

The facility simulates a 1000 MWe PWR with a cold leg break and has a full length pressure vessel which includes a core, a downcomer, lower and upper plenums. The facility also consists of four full-length primary loops with steam generators and pump simulators. The core consists of 32 8×8 rod bundles which are electrically heated and models a typical 15×15 fuel assembly of a PWR arranged in a cylindrical configuration. An accumulator (Acc) system and a low pressure injection (LPCI) system are equipped as an emergency core cooling (ECC) system.

Volumetric scaling of the system is based on a core area scaling ratio of 1/21.4.

Since the overall description of the facility have already made in the previous report,[1] some portions of the facility will be discussed in detail.

Core and tie plate

The core is divided into three power zones and the power level of each power zone is variable, i.e. the radial power distribution is variable. The cross section of the pressure vessel is shown in Fig. 1. In this and the following figures, PN denotes the direction of the plant north.

As an actual 15×15 array assembly has 21 unheated rods, the 8×8 array bundle should have six unheated rods. However, seven unheated rods are assembled in the bundle since a three phase AC power supply system needs heated rods of a multipul of three in number (the nearest value is 57). The local peaking factor was referred from the FLECHT-SET,[5] i.e. 1.1 in high power rods (denotes H rods)(12 rods), 1.0 in medium power rods (M rods)(17 rods) and 0.95 in low power rods (L rods)(28 rods). The arrangement of rods in the bundle is shown in Fig. 2. The power is supplied from the bottom of the vessel through the extension of the heated rod. The top of heated rods connected to each other with soft stranded copper wire.

The tie plate preserves a blockage ratio of the upper tie plate of an actual bundle, which is estimated 52% in a PWR, and is simulated

with a plate having 7×7 holes of 12.8×10^{-3}m diameter for a 8×8 rod bundle. The holes are exactly located above the subchannels of the bundle. The relative elevations of the tie plate, the upper core support plate and the top of core of the CCTF and a PWR are compared in Fig. 3. The elevation of the tie plate is higher than that of a PWR in order to prevent from contacting the connecting copper wires of heated rods with the tie plate due to the thermal expansion of the core.

Upper plenum internals

The internals simulate those of the previous design for the Westinghouse 17×17 array assemblies. For scaling of the internals, the following three ways can be considered: 1) scaling of their radial dimensions without changing their quantity, 2) reducing the quantity without changing their dimensions and 3) an intermediate way. It is very important to simulate the entrainment behavior in the upper plenum, which governs a so-called steam binding effect. Both the size and the quantity are sensitive parameters to the probability of de-entrainment of water on the surface of the internals. Therefore the third way was adopted and the radial dimensions are compromised to be about a half of the actual dimensions. Since the size of each internal should correspond to the size of a bundle, the design of 8×8 array bundles was adopted and accordingly the radial dimensions of the internals were scaled down on 8/15 of the actual dimensions.

The types and quantities of the internals in a reference PWR[6] and the CCTF are listed in Table 1.

Instead of the support columns with mixers, the stub mixers are installed, i.e. the quantity of the stub mixer is designed to be the sum of the desired quantity of the support column with mixer and the stub mixer. The reason is as follows: 1) In 8/15 sized internals, the long structures like control rod guide tubes and support columns overblock the entrainment entering the hot leg, resulting in too much de-entrainment. Therefore the reduction of the quantity of the long structures is necessary. 2) The hydrodynamic characteristics of the stub mixer are almost equivalent to those of the support column with mixer except for the de-entrainment characteristics. Since the bottom of openings of the support column and the top of the stub mixer has the same elevation and the flow resistance of the openings are negligible

in comparison with that of the mixer, the flow resistances at the upper support plate and the fall back characteristics of both internals are almost identical.

Since the control rod guide tubes are arranged in a line in the vicinity of the hot leg nozzles in a PWR, the simulated guide tubes of CCTF are arranged in the same manner. The dimensions of the openings and the gap between adjacent guide tubes are also scaled down in 8/15 of the actual.

The arrangement of the internals of the CCTF and the corresponding bundle number are shown in Fig. 4.

2. Instrumentation

Many differential pressure transducers and thermocouples were installed to measure the differential pressures, fluid temperatures and wall temperatures. In the places where the velocity of liquid phase is very low, the frictional loss and the acceleration loss are negligible compared with the gravitational loss. Hence it is considered that the pressure drops expressed in the water head indicate the collapsed water level or the water accumulation in the downcomer, the core, the upper plenum and the lower plenum. In the downcomer and the core, the differential pressures were measured in four orientations DPD1∿4 and DPC1∿4 as shown in Fig. 1, respectively. The flow meters were equipped to measure the injection flow rates.

About 900 thermocouples were uniformly attached on the clad surface of the simulated core in order to determine whether the thermo-hydrodynamic behavior in the core is one-dimensional or not. Sheathed thermocouples of 0.5 mm diameter are buried on the outside clad surface. Including other detectors, more than 1600 channels of data were recorded.

3. Test procedure

The test procedures were as follows: After establishing the initial conditions of the test, the lower plenum was filled with saturated water to a specified level of 0.9 m from the bottom of the lower plenum for these tests. This elevation is 1.2 m below the bottom of the heated core, and is just above the pipe for the ECC injection into the lower plenum. Electric power was applied to the heated rods of the core. When the maximum temperature of rods reached the specified temperature, the water in the accumulator was injected into the lower plenum (Acc/LP mode). When the water was estimated to reach the bottom of the core, decay of the heating power was scheduled to be automatically started at a programmed rate, corresponding to the reactor decay heat. After the assumed time delay, the water injection location was changed from the lower plenum to the ECC ports of the three intact cold legs. The ECC water was still supplied from the accumulator and this period is defined as the accumulator mode (Acc mode). After a specified time delay, the injection mode was transferred from Acc mode to the low pressure coolant injection mode (LPCI mode). The system pressure was kept constant.

The test conditions of the base case test are listed in Table 2. The power was supplied to three radially divided power zones of the core as shown in Fig. 1 and the ratios of the power densities in the three zones were 1.15, 1.10, and 0.89 in the base case test. In Asymmetric power test, the test conditions except for the power distribution were the same as those of the base case test. In the test, the power distribution was skewed as shown in Fig. 5(a) and the average power in each power zone was intended to be identical as that of the base case test.

In Asymmetric temperature test, the test conditions except for the initial clad temperature distribution were the same as the base case test. In the test, the initial clad temperature distribution was skewed as shown in Fig. 5(b) and the initial stored energy of the whole core was intended to be identical as that of the base case test. However, due to the difficulty in the setting of the suitable initial clad temperature, the initial stored energy of the whole core was not identical as that of the base case test.

The initial stored energy of the core was evaluated by using the

temperature readings at the reflood initiation. The wall superheats obtained from the five thermocouples on a rod for each bundle were used for this evaluation.

The evaluated initial stored energies are:

(1) For Base case test: 5.69×10^5 J

(2) For Asymmetric power test: 6.32×10^5 J

(3) For Asymmetric temperature test: 7.20×10^5 J .

It is found that the initial stored energy for Asymmetric temperature test is about 25 % higher than that for Base case test.

Table 1 Component number of upper plenum internals

Component	PWR (193 components)	CCTF (32 components)	
	Quantity	Desired quantity	Selected quantity
Control rod guide tubes	61	10.11	12
Support columns without mixers	21	3.48	4
Support columns with mixers	27	4.48	
Stub mixers	31	5.14	8
Orifice plates	12	1.99	2
Open holes	41	6.80	6

Table 2 Test conditions of the base case test and their data bases

Items	Values	Data bases
System pressure	2 kg/cm^{2}a	2.5∿1.5 kg/cm^{2}a (Takahama 3.4)
Initial average linear power	1.4 kW/m	1.34∿1.37 kw/m Trojan 2% over power 30 sec after shutdown
ECC injection		Data referred in FLECHT-SET
Acc flow rate	280 m^3/h	378∿287 m^3/h
Acc water temp.	35 °C	35 °C
Acc injection period	14 sec	14 sec
LPCI flow rate	30 m^3/h	40 m^3/h
LPCI water temp.	35 °C	35 °C
Maximum initial clad temp.	600 °C	870 °C (Sendai 1)
SG secondary side water temp.	265 °C	265 °C
Downcomer wall temp. wall temp. of vessel below cold legs	198 °C	∿176 °C Equivalent wall temp.
Wall temp. of non-specified structures	119 °C (Saturation temp.)	——
K_{factor} of primary loops	∿25	24.45 (FLECHT-SET)
Decay curve of power	ANS × 1.2 + Actinide × 1.1 (Delayed neutron effect is considered in the initial power)	ANS × 1.2 + Actinide × 1.1 + Delayed neutron
Radial power factor	1.15	1.435
Axial power factor	1.49	1.546
Local power factor	1.1	1.027
Total peaking factor	1.885	2.278 (Sendai 1)

III. Results and discussion

1. Core hydrodynamic behaviors observed in the base case test

Azimuthal uniformity of core hydrodynamics

Figure 6 shows the differential pressures measured at the various elevations. Each hatched band involves the differential pressures measured in four azimuthal orientations of the core at each elevation. Since the frictional loss and the accelerational loss are negligible comparing the static head of the accumulated water because the liquid mass flow rate is very low during reflood phase, the differential pressure is nearly equal to the static head. The figure shows the four differential pressures in different orientations overlap with each other in a narrow hatched band. This indicates that the water accumulation, i.e. liquid fraction, in the core is axi-symmetric under the axi-symmetric power distribution. In order to conclude the one-dimensionality of the hydrodynamics in the core, it is necessary to investigate the cross flow to the radial direction. This will be discussed later using the result of the multi-dimensional effect tests.

Water accumulation behaviors

Figure 7 shows the transients of the differential pressures covering the whole heated core, $\Delta P_1 \sim \Delta P_6$. The differential pressures in the end box region and the upper plenum, ΔP_E and ΔP_U, respectively, are also shown in the figure. ΔP_E represents the differential pressure between the top of the heated core and the top of the core support plate and ΔP_U represents the differential pressure between the top of the core support plate and the top of the upper plenum. The white and dark circles indicate the bottom-quench time and the top-quench time, respectively. In this report, when the quench of a rod at a specified elevation is earlier than that at lower elevation, it was thought that the quench front propagated downward at the specified elevation and such a quench phenomenon was defined as the top quench. Otherwise the quench front was thought to propagate upward and the quench phenomenon was defined as the bottom quench.

The initiation time of the reflood is indicated in the figure as BOCREC, the bottom of core recovery. $\Delta P_1 \sim \Delta P_6$ and ΔP_E begin to increase nearly at the reflood initiation. It indicates that the water accumulation

began over the whole core and the end box region nearly at the reflood initiation. Within 20 to 30 seconds these differential pressures appear to become nearly constant, i.e. the water accumulation was almost terminated. This means that the water content in each measuring section has a kind of saturated value and is saturated nearly at the same time. ΔP_U then begins to increase, i.e. the water accumulation in the upper plenum began after the water accumulation appeared to almost terminate over the core and the end box region.

The duration shadowed in the figure indicates the time when the quench front exists in each measuring section of the differential pressure. It is noticeably found that the increase of each differential pressure, i.e. the increase of the water accumulation in each measuring section is remarkable for each shadowed duration, specially in $\Delta P_2 \sim \Delta P_5$. This can be explained as follows: The steam flow rate just above the quench front is much higher than that below the quench front due to noticeable high steam generation caused by the heat release from the quenching portion. This causes the water accumulation below the quench front is much more than that above the quench front. Accordingly, while the quench front advances in a respective measuring section, the much water accumulation region advances, resulting in the noticeable increase of the differential pressure in the section.

The differential pressure generally decreases with the elevation, as observed in $\Delta P_1 \sim \Delta P_4$, i.e. up to the 2.44 m elevation from the bottom of the core. This is due to the higher steam flow rate with the higher elevation. However, regarding to ΔP_5 and ΔP_6, a different tendency is observed during the early period up to 350 seconds, i.e. ΔP_5 and ΔP_6 are larger than ΔP_4, which is measured at lower elevation. This opposite relation disappears at 350 seconds, which is almost corresponding to the quench time at the elevation of the lower pressure tap for ΔP_4 measurement. These suggest that the water accumulation behavior at the ΔP_5 and ΔP_6 measuring elevations is different from that at the ΔP_1 through ΔP_4 measuring elevations. The reason is not clarified.

Figure 8 shows the detail of the differential pressure transients during the early period. In 1 to 4 seconds after reflood initiation, $\Delta P_3 \sim \Delta P_6$ begin to increase. The increasing rate changes at about 13 seconds after reflood initiation. This time is corresponding to the termination time of the Acc injection. At 24 seconds after reflood initiation, indicated as A in the figure, $\Delta P_1 \sim \Delta P_6$ and ΔP_E appear to

become nearly constant.

The early initiation and saturation of the water accumulation from the bottom to the top of the core were observed in the JAERI's small scale reflood test[3] and the phenomena were considered to be caused by the entrainment behaviors in the core as follows: When the water level is above the quench front and some portion of the water above the quench front generates steam much enough to produce entrainment, i.e. water droplets, the steam and the entrainment rapidly transfer over the whole core with the velocity of the steam, if the slip velocity between the steam and the entrainment is low. And it was considered that the entrainment began to be integrated and the slug flow was gradually formed in the whole core, i.e. the water accumulation initiated over the whole core. In the slug flow, the slip velocity between two phases are relatively higher than that in the water droplet flow. Therefore,more water could be accumulated in the case of the slug flow, however, the maximum liquid fraction is thought to be controlled by the steam flow rate and the water accumulation was terminated, when the local steam flow rate became constant.

Since the observed phenomena in CCTF and the small scale reflood test are similar with each other, the flow pattern in CCTF is recognized as a slug flow.

2. Core cooling behaviors observed in the base case test

Quench behavior

Figure 9 shows the quench front propagation of selected rods. From the inspection of all rods, it was found that at the lower core denoted in the figure the quench was always the bottom quench and at the upper core denoted in the figure the quench was always the top quench. In the intermediate core, the bottom quench occurred on some rods and the top quench on other rods.

Since the quench occurs simultaneously at the same elevation in the lower core, it can be considered that the bottom quench at the same elevation occurs at nearly the same time, independently of the radial location and the power density. This indicates that the bottom quench front moves nearly one-dimensionally. On the contrary, in the intermediate core the quench times are significantly variant because the

bottom quench occurred on some rods and the top quench occurred on other rods. Another reason of this variation would be that the top quench itself tends to occur randomly, since the two-phase flow hydrodynamics in the upper core seems to depend on the geometry and is considered to have sensitive effect on the top quench. This will be discussed later.

In the upper core, the uppermost thermocouples showed the very early top quenches, which occurred in 40 seconds after the initiation of the water accumulation in the core. The early top quench is attributed to the low clad surface temperature of the upper portion of the core and the early appearance of water at the upper core. It is considered that the top quench in the upper core is not attributed only to the fall back water down from the upper plenum, because the top quench occurred even before the water accumulation period in the upper plenum.

Figure 10 shows the correspondence of the top quench to the geometry above the bundles at the 3.05 m elevation, which is between the fourth and fifth grid spacers. In this figure, the chain circles indicate the location of the open holes on the upper core support plate, and the dark and the white circles mean the locations of the top-quenched and the bottom-quenched rods, respectively. The strong relationship between the top quench below the fifth grid spacer and the open hole is noticed, i.e. the deep top quench penetration appears in the bundles under the open holes. Another noticeable tendency is that the deep top quench penetration appears mostly in the central core and rarely in the peripheral core.

Heat transfer characteristics

Figure 11 shows the heat transfer coefficients of the H, M and L rods, defined in Section II.1, at the midplane of Bundle 30 which is in the center region of the core. The heat transfer coefficients were obtained from the measured clad surface temperature of rods with the HETRAP code developed by Malang[4] and modified by Sugimoto. The times of the rapid increases of the heat transfer coefficients are corresponding to the local quench times of the concerning points. The heat transfer coefficients for the different power rods at the same elevation and in the same power zone are nearly identical with each other before the quench occur.

Comparing the heat transfer coefficients in the various bundles and at the various elevations, it was noticed that the heat transfer

coefficients are nearly the same with each other at the same elevation except the following location, i.e. (1) the 3.05 m elevation in Bundle 30 and 32 and (2) the 3.05 m elevation in the peripheral bundles.

Figure 12 shows some examples of the heat transfer coefficients at the midplane and the 3.05 m elevation. The heat transfer coefficients at the same elevation agree well with each other except for that of the 3.05 m elevation in Bundle 30. In Bundle 30, the top quench occurred down below the fifth grid spacer. It is considered that the top quench is caused by the higher heat transfer.

Figure 13 shows in detail the corewise distribution of the heat transfer coefficients at the 3.05 m elevation, where the most nonuniformity of the heat transfer coefficients was observed. During the early period (0 to 90 seconds after reflood initiation), the heat transfer coefficients were found to be identical. From 100 seconds to the quench time of the heater rod in Bundle 30, the heat transfer coefficients were nonuniform. Generally the heat transfer coefficients tend to be lower in the peripheral bundles and higher in the central bundles than the average.

Another significant difference is in the heat transfer coefficients of Bundle 29 and 30. Both bundles are in the same power region near the center of the core. The difference of conditions of both bundles is only in the geometrical conditions above the bundles; i.e. a control rod guide tube was installed above Bundle 29, and an open hole above Bundle 30. It can be inferred that the significant difference is caused by the difference of the geometry above the bundles. However, the different geometry above the bundles does not always cause the different heat transfer coefficients. For example, although the difference of Bundle 8 and 14 is only in the geometry above the bundles, the heat transfer coefficients in both bundles are nearly identical. The same tendency are found in Bundle 22 and 26.

The heat transfer coefficient measured at the 3.05 m elevation in Bundle 32 was nearly the same as that in Bundle 30. Both bundles are in the same power region and corresponding to an open hole.

In summary, the core cooling behaviors are uniform over the whole core at the same elevation except the following regions:

(1) The peripheral bundle region in the intermediate and the upper core; The heat transfer coefficient tends to be lower in this region than the average at the same elevation. In addition, the top quench

takes place rarely in this region, comparing with the other region.
(2) The central region in the intermediate and the upper core corresponding to open holes; The heat transfer coefficient tends to be higher in this region than the average at the same elevation. In addition, the top quench takes place easily in this region, comparing with the other region.

From Eq.(1), it can be inferred that the void fraction is uniform at the same elevation in the bottom quench region, since the flow can be recognized as a slug flow, the quench front propagation is uniform and the heat transfer coefficient is uniform at the same elevation in the region.

3. Core hydrodynamic behaviors observed in Asymmetric power test and Asymmetric temperature test

Figure 14 shows the differential pressures which were measured in four azimuthally different orientations of the core in Asymmetric power test and Asymmetric temperature test. The four differential pressures were nearly equal with each other at any respective elevation of the core. In detail, the variation of the four differential pressures exists during the early period of Asymmetric temperature test. However, this variation is below ±10 % and it disappears after about 130 seconds. Accordingly, the water accumulation behavior can be regarded to be one-dimensional even in cases of thermally asymmetric condition, as well as in case of thermally symmetric condition. The SCTF result showed that[2] the differential pressure between the bottom and the top of the core was nearly one-dimensional up to the time when the whole core had quenched completely. This is consistent with the present result.

The flow pattern can be recognized as a slug flow for both asymmetric tests.

4. Core cooling behaviors observed in Asymmetric power test and Asymmetric temperature test

Figures 15 and 16 show the behaviors of the bottom quench front propagations in both tests. In Asymmetric power test, the bottom quench

fronts advanced nearly one-dimensionally. In Asymmetric temperature test, the bottom quench fronts advanced asymmetrically during the early period, i.e. they advanced faster on the cold side than on the hot side. However, this asymmetry decreased gradually, and disappeared when the quench front reached the midplane of the core.

Figures 17 and 18 show the correspondences of the top quench at the 3.05 m elevation to the geometry above the bundles. It is noticed that the strong relationship between the top-quenched rods and the open hole on the upper core support plate exists, as noticed in the base case test. No special effect of thermally multi-dimensional test condition is recognized in Asymmetric power test. However, in Asymmetric temperature test, the top quench was not observed in the hot side except the central core.

Figure 19 and 20 show the heat transfer coefficients at the 2.44 m elevation. In order to investigate the effect of thermal asymmetry on the core cooling, the heat transfer coefficients in diagonally located three bundles are compared in each figure. The heat transfer coefficients are uniform in both tests. This uniformity was found at the most of elevations and showed the uniformity of the void fraction as estimated from Eq.(1).

At the 1.02 m elevation in Asymmetric temperature test, the heat transfer coefficient in the hot side is lower than that in the cold side, as shown in Fig. 21. The lower heat transfer coefficient in the hot side is attributed to slower quenching due to hotter clad surface, since the heat transfer coefficient is a function of the distance from the quench front to the concerning point and the local void fraction as indicated in Eq.(1). This can be confirmed by shifting the curve of the heat transfer coefficient of the hot side to meet the curve for the cold side at the quench time. The overlapping of the curves shows that the heat transfer coefficients at the same distance from the quench front are identical near the quenching period. Considering that the discrepancy of the void fractions between the hot and cold sides is small near the quenching period, it can be inferred that the heat transfer coefficients of the hot and cold sides is identical, if the quench velocity is equal with each other.

Figure 22 shows the comparison of the clad surface temperatures in diagonally located three bundles at the 2.44 m elevation, where the maximum turnaroud temperature was observed. The higher turnaround

temperatures and the later quench time were observed in the high power side than in the low power side. This power dependency is reasonable, since the heat transfer coefficients are identical at the elevation. In Asymmetric temperature test, the corewise distribution of the clad surface temperatures appears at the same elevation during the early period (0∿250 seconds), as shown in fig. 23. However, the corewise distribution gradually becomes uniform.

5. Effect of the thermally asymmetric condition on core behaviors

Figure 24 shows the core water distributions of the base case test and the thermally asymmetric tests. The differential pressures are almost the same. In detail, however, the core differential pressures in thermally asymmetric tests are slightly lower than those in the base case test.

Figure 25 shows the comparison of quench front propagations of the low power rods in the medium power region among the base case test and thermally asymmetric tests. It indicates that the quench occurs slightly later in Asymmetric temperature test than in the base case test. This is, as described in the section 4, attributed to the slightly higher initial stored energy in Asymmetric temperature test.

Figure 26 shows the comparison of the heat transfer coefficients among the base case test and thermally asymmetric tests. In this figure, the heat transfer coefficients obtained at the 2.44 m elevation in Bundle 23, which is located in the hot side, were selected as typical ones. The heat transfer coefficient in Asymmetric power test is almost identical with that in the base case test. However, the heat transfer coefficient in Asymmetric temperature test, is found to be lower than those in the base case test. The maximum difference is about -30 %. In the cold side, similar tendency was observed, i.e. the heat transfer coefficient in Asymmetric temperature test was lower than that in the base case test. This lower heat transfer coefficient is attributed to slower quenching.

6. Effect of the thermally asymmetric condition on the system behavior

Figure 27 shows the mass flow rates at the core inlet, the core outlet and the loop obtained in the base case test, Asymmetric power test and Asymmetric temperature test. The figure shows good agreement among three tests.

Figure 28 shows the core water accumulation in three tests. This figure also shows good agreement. These suggest that the effect of the thermally asymmetric condition on the system behavior is negligible if the energy initially stored in the core and the power averaged over the core are equal to those in the thermally symmetric condition.

7. Summary of experiments

From the base case test the following experimental results were found:

(1) The water accumulation was initiated along the whole core almost simultaneously just after reflood initiation. Within 20 to 30 seconds, the water accumulation is almost terminated. The flow pattern was recognized as a slug flow. This phenomena is very similar to those for the JAERI's small scale reflood tests.

(2) The water accumulation was found to be azimuthally uniform at the same elevation. In the intermediate core and the upper core, relatively higher water accumulation was observed. The mechanism is not clarified. (The terms, the lower core, the intermediate core and the upper core, are defined in Fig. 9).

(3) The bottom quench front, which was observed in the lower and the intermediate core, propagated uniformly.

(4) In the upper core, the very early top quench was observed at the every rod with thermocouples.

(5) The top quench in the upper core is not attributed only to the fall back water from the upper plenum.

(6) In the intermediate core, the top quench was observed on the some portion of rods, however, the location and the time of the top quench were variant. The top quench occurred mostly in the bundles corresponding to open holes and in the central core, and occurred rarely in the peripheral core.

(7) The heat transfer coefficient was uniform at the same elevation except for the heat transfer coefficients in the following regions:

i) The peripheral bundle region in the intermediate and the upper portions of the core, where the heat transfer coefficients are lower than the average value at the same elevation.

ii) The central region corresponding to the location under the open holes in the intermediate and the upper portions of the core, where the heat transfer coefficients are higher than the average value at the same elevation.

(8) It was inferred that the void fraction is uniform at the same elevation where the heat transfer coefficient is uniform.

From the thermally asymmetric tests; the following experimental results were found:

(9) The water accumulation in the core was found to be azimuthally uniform at the same elevation and nearly identical with that for the base case test. This indicates that the void fraction is uniform at the same elevation.

(10) The bottom quench front propagated uniformly except for the lower core region in Asymmetric temperature test.

(11) The top quench was also observed in the thermally asymmetric tests. However, no special effect of thermal asymmetry on the top quench was recognized in Asymmetric power test. In Asymmetric temperature test, the top quench did not occurred in the hot side except for the central region.

(12) The heat transfer coefficient at the elevation of 1.83 m up to 2.44 m was uniform. Below the elevation, the heat transfer coefficient in the hot side was slightly lower than those in the cold side. This is attributed to slow quenching in the hot side.

(13) The azimuthal temperature distribution of the heated rods in the core became uniform gradually with time.

(14) The effect of the thermally asymmetric condition on the system behavior can be considered to be negligible if the energy stored in the core and the power averaged over the core are equal to those in the thermally symmetric condition.

8. Application of the present findings to LOCA analysis

In general, the differential pressures in the core, i.e. the core water accumulation were uniform and nearly identical for three tests and the heat transfer coefficients were uniform as far as the bottom quench front propagation was uniform. The occurence of the top quench and the heat transfer coefficient in the upper elevation were nonuniform.

The effect of the top quench on the core cooling and system behaviors is negligible, since

(1) The top quench is considered to have slight influence on the bottom quench and the heat transfer in the bottom quench region.

(2) The heat release by the top quench is considered to be very small comparing that by the bottom quench and by the convection, and

(3) The maximum temperature appears in the bottom quench region as shown in Fig. 29.

Accordingly, the water accumulations in the cores having the same average power and the same initial stored energy with each other can be one-dimensionally analyzed with a common single channel core. Since the heat transfer coefficient can be considered to be a function of the void fraction and the distance from the quench front in the bottom quench region, it is inferred that the heat transfer coefficient can be estimated from the local void fraction in the representing single channel core and the analysis of the quench front propagation for the concerning rod.

Since the system behaviors for the three tests are almost identical, it is inferred that, as well as the core water accumulation, the evaluation of the core behavior for the system analysis can be analyzed with the representing single channel core.

IV. Conclusion

1. The water accumulation was initiated along the whole core even above the quench front almost simultaneously just after reflood initiation. Within 20 to 30 seconds, the water accumulation is almost terminated. The phenomena are almost identical for three tests. The flow pattern above the quench front was recognized as a slug flow. Phenomena is very similar to those for the JAERI's small scale reflood tests.
2. In the lower two-thirds of the core, the bottom quench was observed and the core water accumulation was almost one-dimensional even under the thermally asymmetric conditions. This indicates that the void fraction is uniform at the same elevation.
3. In the base case test and Asymmetric power test, the bottom quench propagated almost uniformly and the heat transfer coefficients were nearly identical at the same elevation almost over the core. This also suggests that the void fraction is uniform at the same elevation.
4. The multi-dimensional effect on the top quench was observed, i.e. top quenches in the intermediate core defined in Fig. 9 occurred only at the some bundles under the open holes of the upper support plate except for the region near the surrounding wall and the heat transfer coefficients at the location were higher than the average. In the upper quater of the core, the early top quench was observed on every instrumented rod. In these region, the water accumulation was relatively higher. However the mechanism is not clarified.
5. In Asymmetric temperature test, the heat transfer coefficients were about 30 % lower than those of the base case test. This was attributed to the slower quenching due to the slightly higher initial stored energy.
6. In Asymmetric temperature test, though the quench front was not uniform initially, the bottom quench front became uniform when the quench front reached the midplane of the core and simultaneously the clad surface temperatures of the hot and cold isdes became close gradually.
7. It is concluded that the water accumulation behavior or void fraction in the lower two-thirds of the core, i.e. our concerning region for the peak clad temperature analysis, and the core behavior for system analysis can be one-dimensionally analyzed with a representing single channel core.

Nomenclature

E	:	Emissivity
g	:	Acceleration of gravity (m/s^2)
H_{fg}	:	Latent heat of evaporation (J/kg)
h	:	Heat transfer coefficient ($W/m^2 \cdot K$)
L_q	:	Distance from quench front (m)
ΔP_U	:	Differential pressure in upper plenum (Pa)
$\Delta P_1 \sim \Delta P_6$	:	Differential pressure defined in Fig. 7 (Pa)
T	:	Temperature (K)
α	:	Void fraction
ΔT_{sat}	:	Superheat of wall (K)
ε	:	Stefan Boltzmann constant ($W/m^2 \cdot K^4$)
λ	:	Thermal conductivity ($W/m \cdot K$)
μ	:	Dynamic viscosity ($Pa \cdot S$)
ρ_ℓ	:	Density of liquid (kg/m^3)

(Subscripts)

W	:	Wall
sat	:	Saturated

Acknowledgement

The authors are much indebted to Mr. T. Sudoh, Dr. H. Akimoto and Messrs. J. Sugimoto and T. Okubo for their technical supports. The authors would like to express their thanks to Dr. M. Nozawa, director of the Nuclear Safety Research Center, to Dr. S. Katsuragi, head of Div. of Nuclear Safety Research, to Dr. M. Ishikawa, deputy head of Div. of Nuclear Safety Research, and to Dr. K. Hirano, chief of Reactor Safety Laboratory II at JAERI for their guidance and encouragement for this program. The authors also would like to express their appreciation to the 2D/3D project members of USA and FRG, especially Dr. L.S. Tong of USNRC and Prof. Dr. F. Mayinger of T.U. München for valuable discussions.

References

(1) Murao, Y., et al.: Experimental Study of System Behavior during Reflood Phase of PWR-LOCA Using CCTF, J. Nucl. Sci. Technol., 19 [9], pp.705∿719, (1982)

(2) Adachi, H., et al.: SCTF Core-I Test Results (System Pressure Effects on Reflooding Phenomena), presented at the USNRC's ninth water reactor safety information meeting, 1981 in Maryland, USA.

(3) Murao, Y. and Iguchi, T.: Experimental modeling of core hydrodynamics during reflood phase of LOCA, J. Nucl. Sci. Technol., 19 [8], pp.613∿627, (1982).

(4) Malang, S., "HETRAP: A Heat Transfer Analysis Program", ORNL-TM-4555 (1974)

(5) Waring, J.P., et al.: PWR FLECHT-SET PHASE B1 EVALUATION REPORT, WCAP-8583 (1975)

(6) Trojan nuclear plant, Final safety analysis report volume 1∿9, DOCKET-50344-38∿46, (1973)

(7) Murao, Y. and Sugimoto, J.: Correlation of heat transfer coefficient for saturated film boiling during reflood phase prior to quenching, 18 [4], pp.275∿284 (1981)

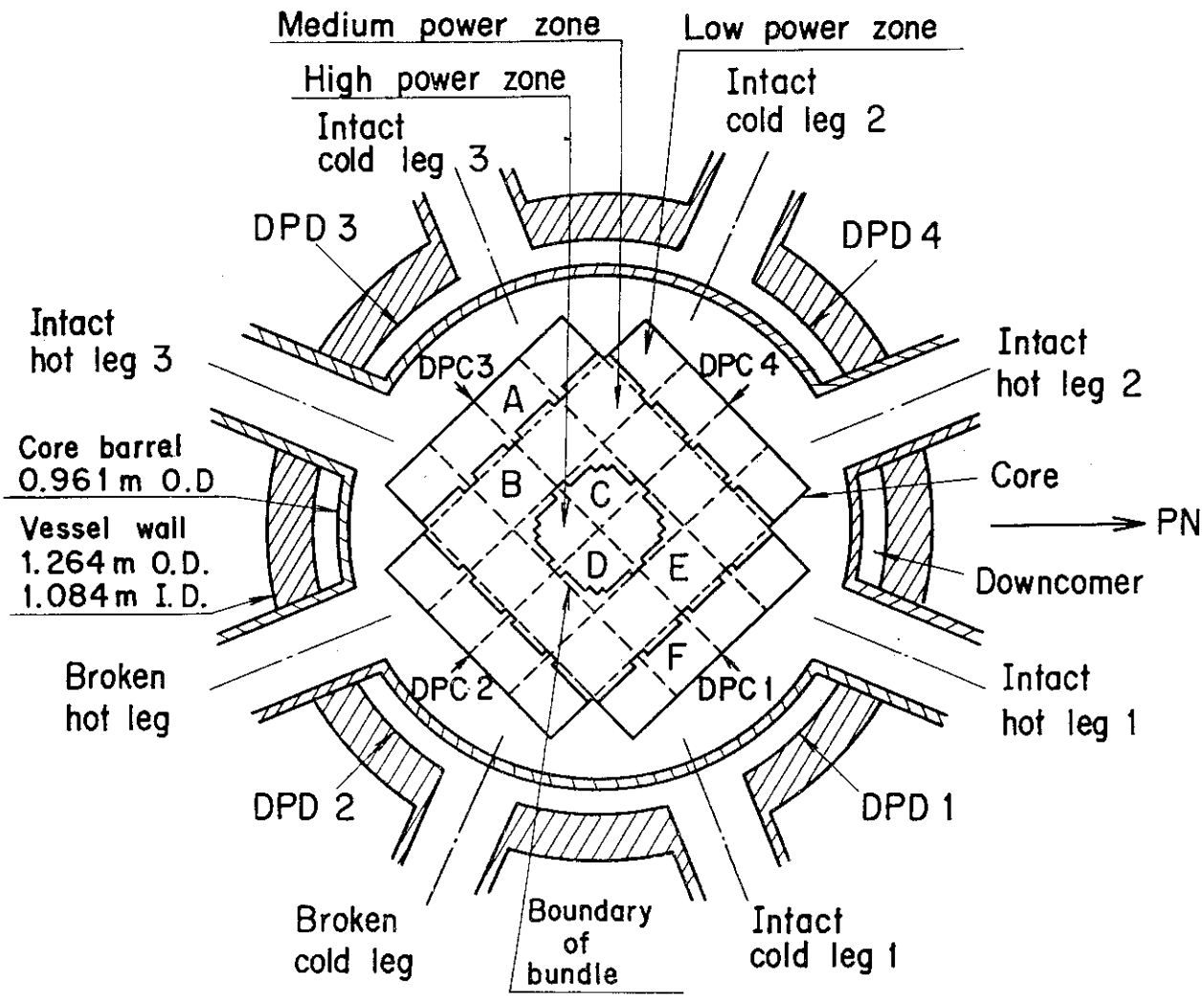

Fig. 1 Cross section of pressure vessel

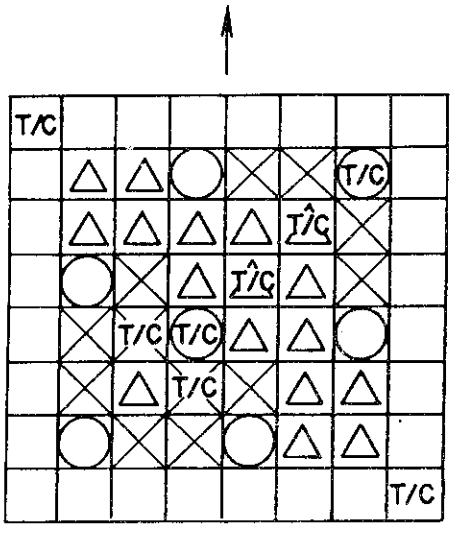

Bundle numbered
3, 6, 11, 14,
18, 22, 24, 28,
30, 32
in Fig. 4

Symbols

- Low power rod (L rod)
- Medium power rod (M rod)
- High power rod (H rod)
- Non-heated rod
- T/C Thermocouple-attached rods
- Bundle direction

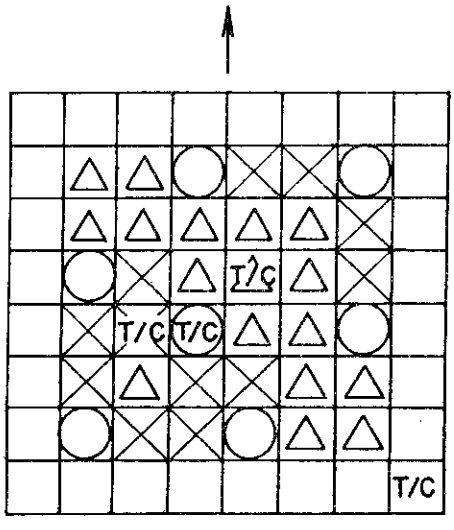

Other bundle

Fig. 2 Arrangement of heated rods in bundle

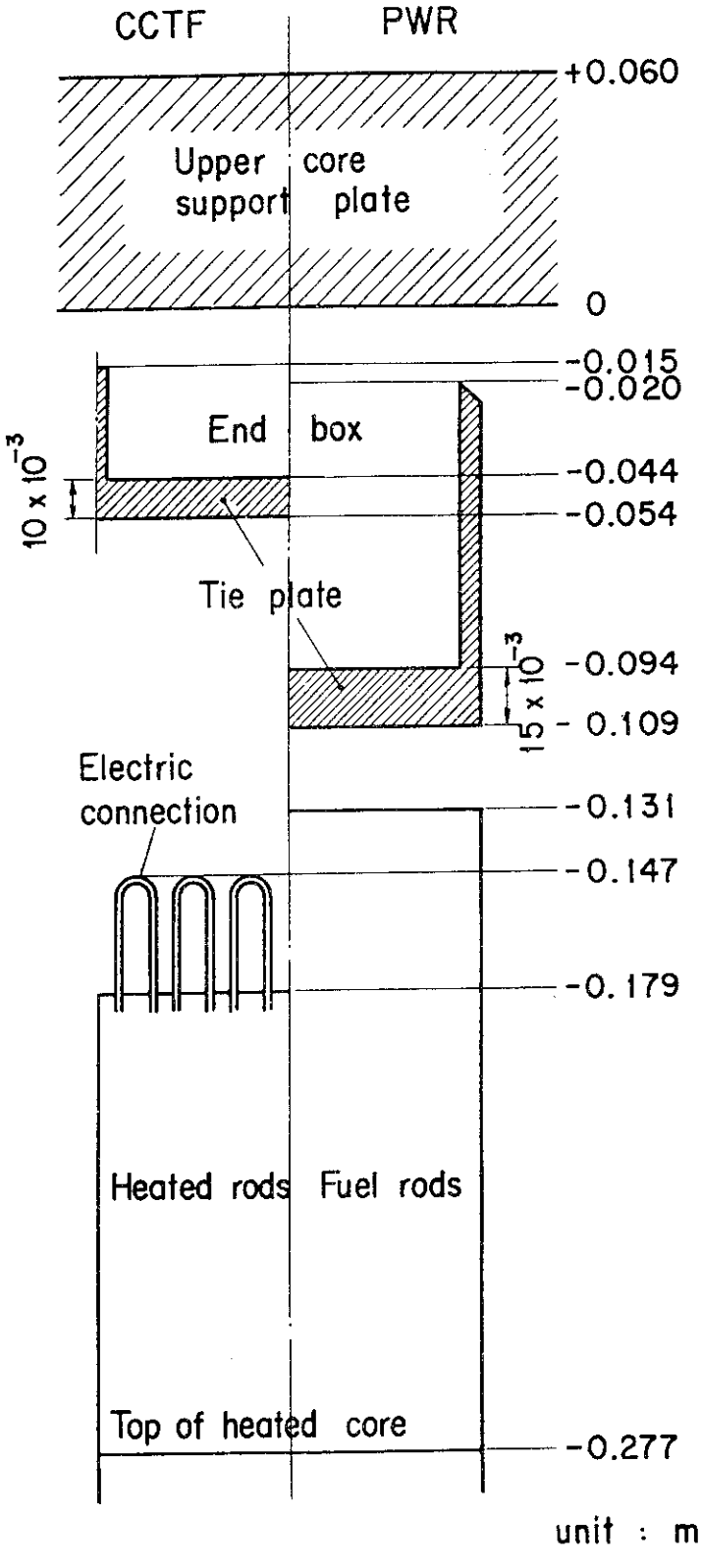

Fig. 3 Relative elevations of tie plates, upper core support plates and top of cores of CCTF and PWR

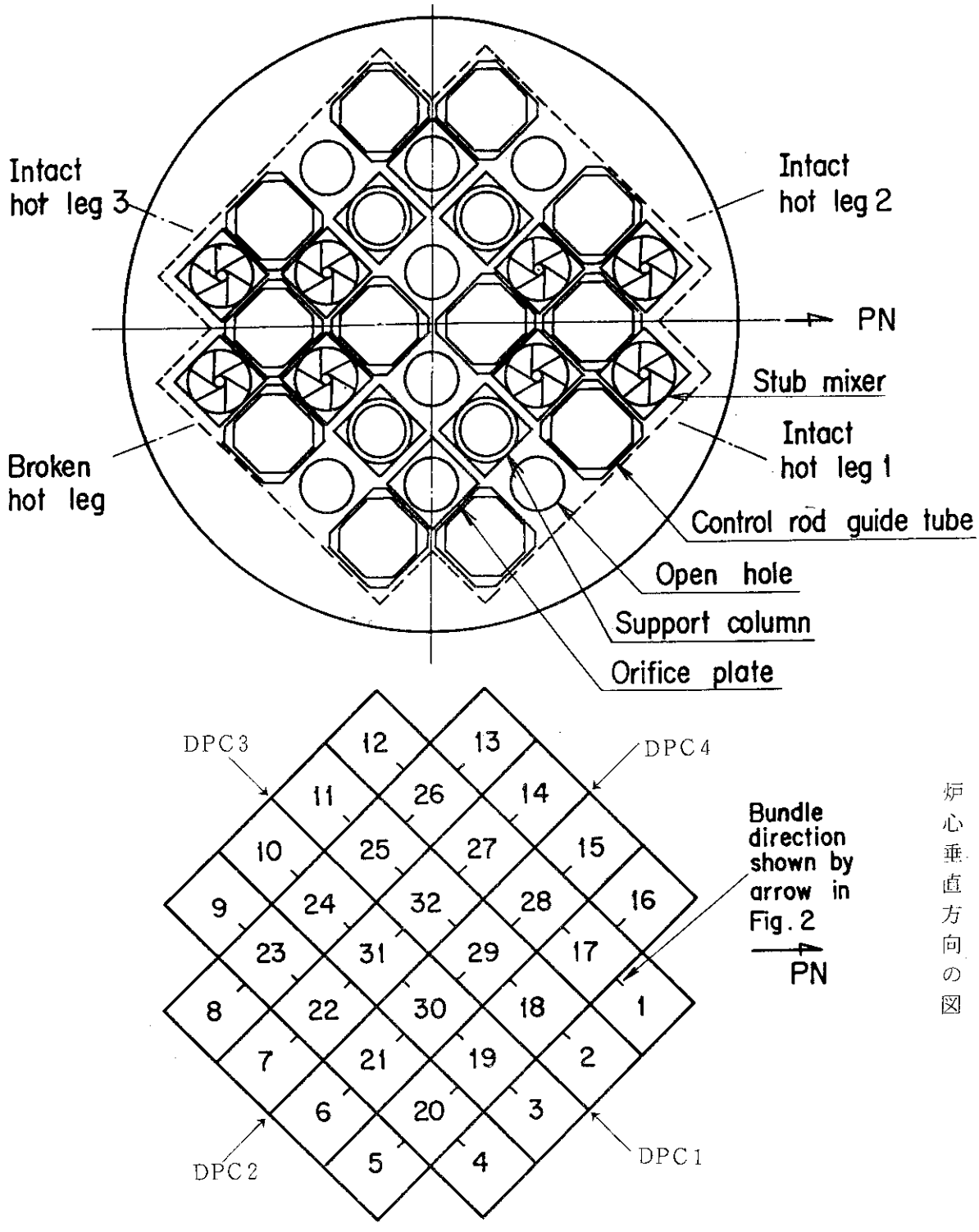

炉心垂直方向の図

Fig. 4 Arrangement of upper plenum internals and corresponding bundle number

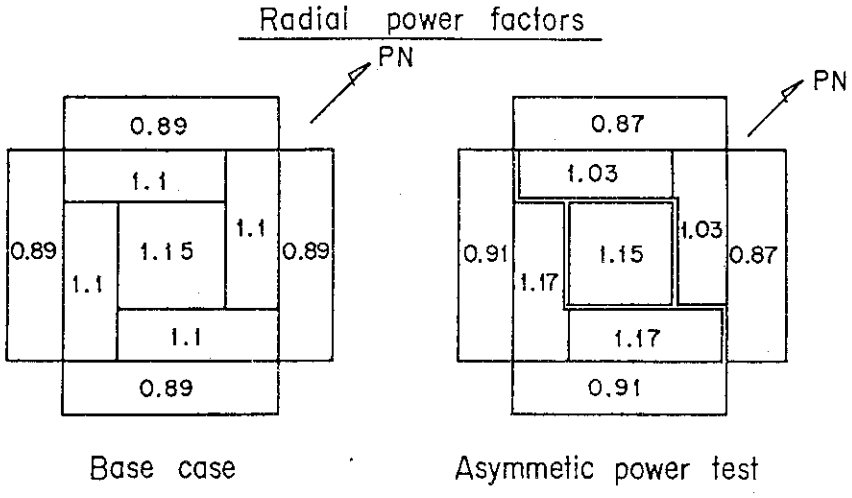

Fig. 5 (a) Initial power distribution of Asymmetric power test

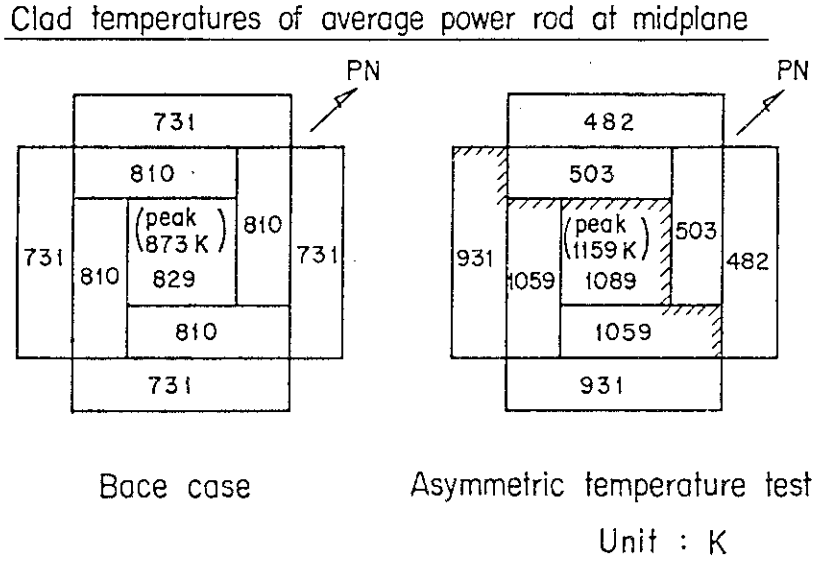

Fig.5 (b) Initial temperature distribution of Asymmetric temperature test

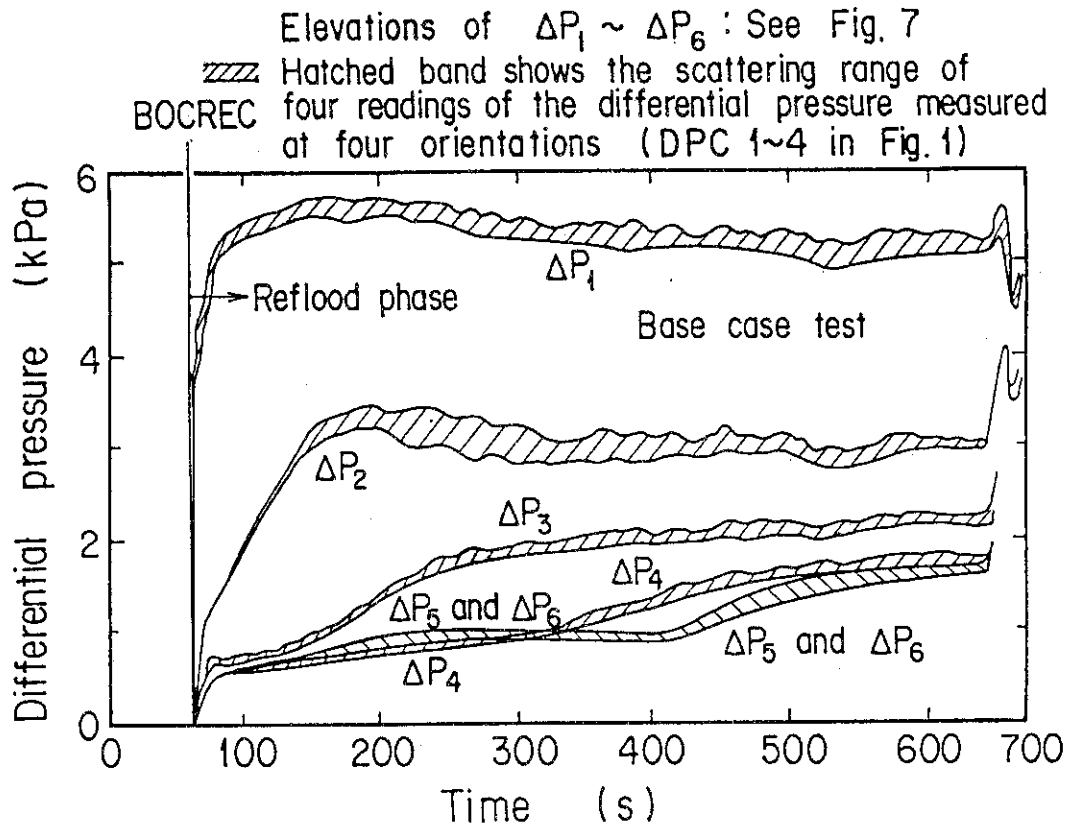

Fig. 6 Uniformity of differential pressures in core in base case test

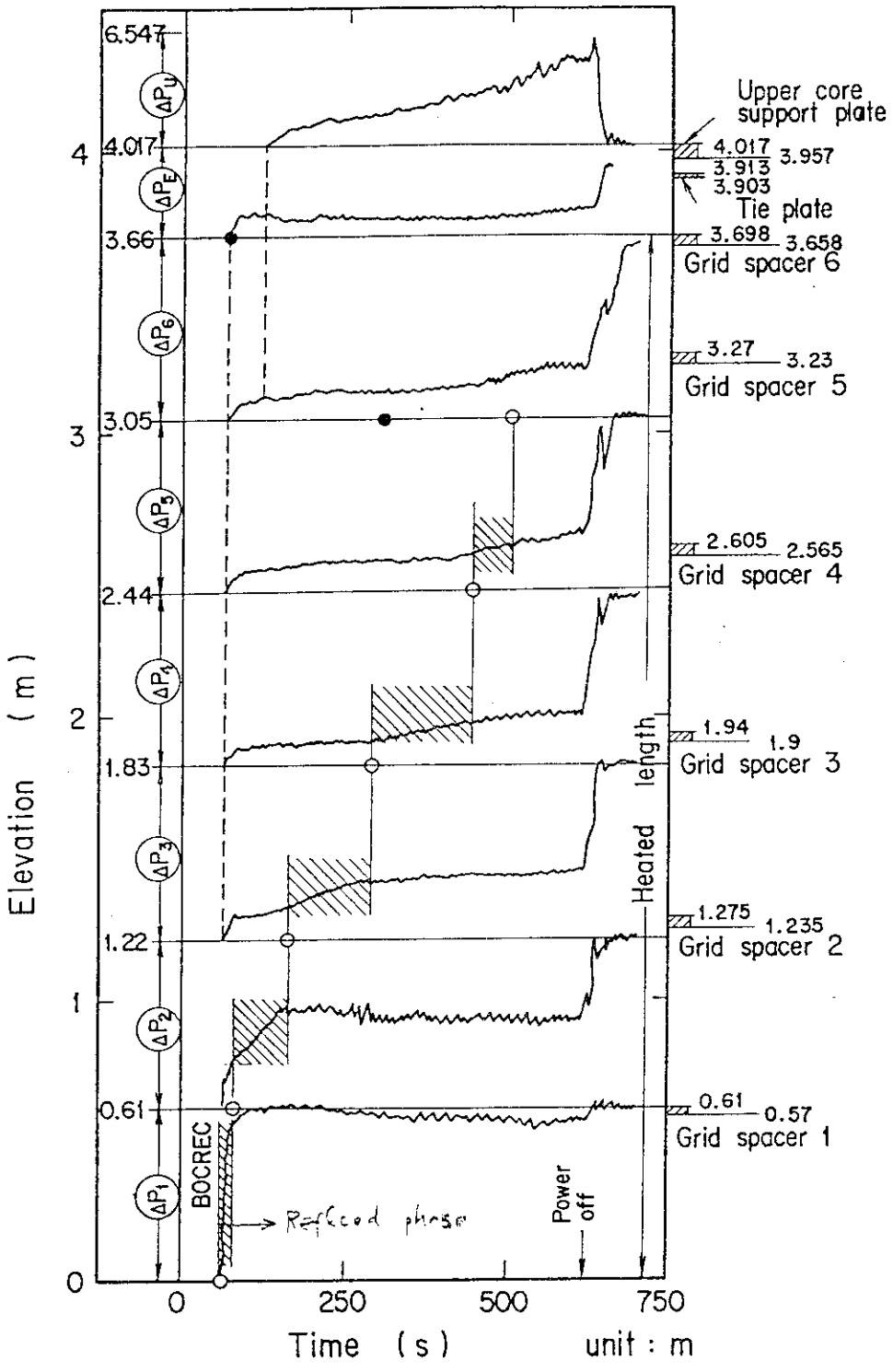

Fig. 7 Comparison of the differential pressures of whole core, end box region and upper plenum

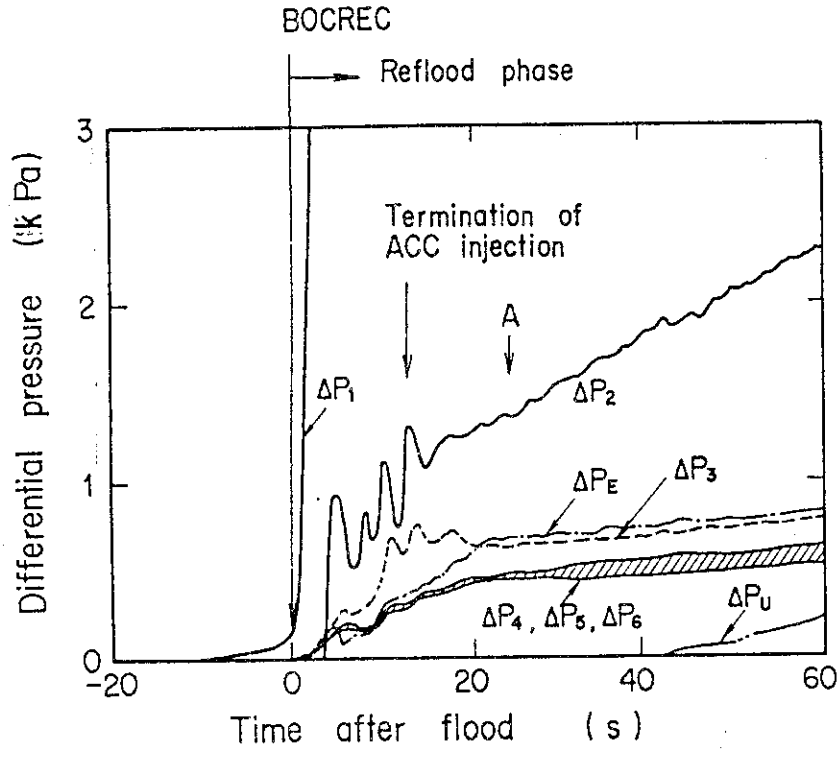

Fig. 8 Detail of differential pressure transients of whole core, end box region and upper plenum

Symbols	H rod	L rod
Bundle 17	●	○
Bundle 23	■	□
Bundle 30	▲	△

GS1 ~ 6 : Elevation of Grid spacer 1 ~ 6

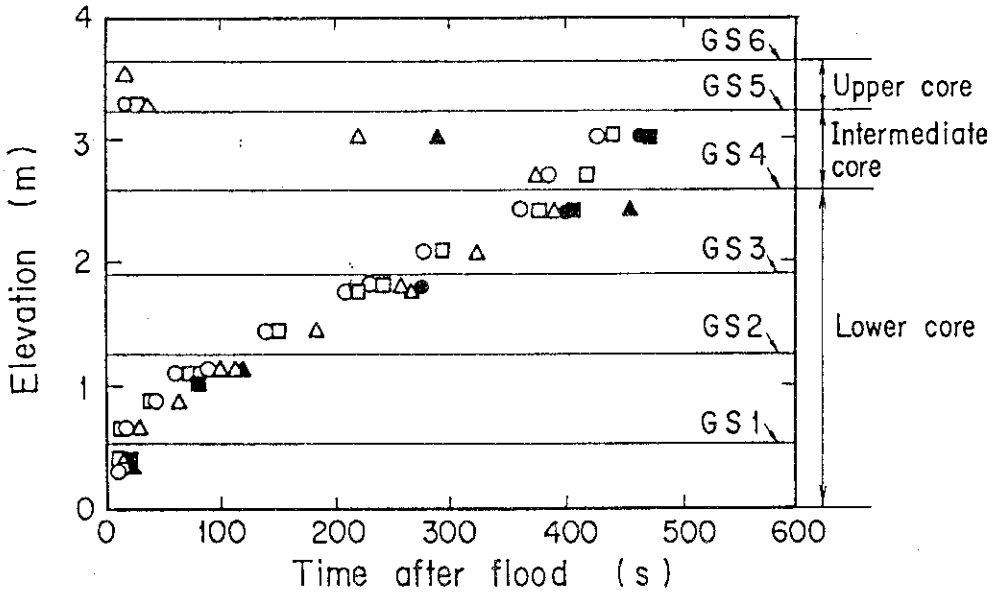

Fig. 9 Quench front propagation in base case test

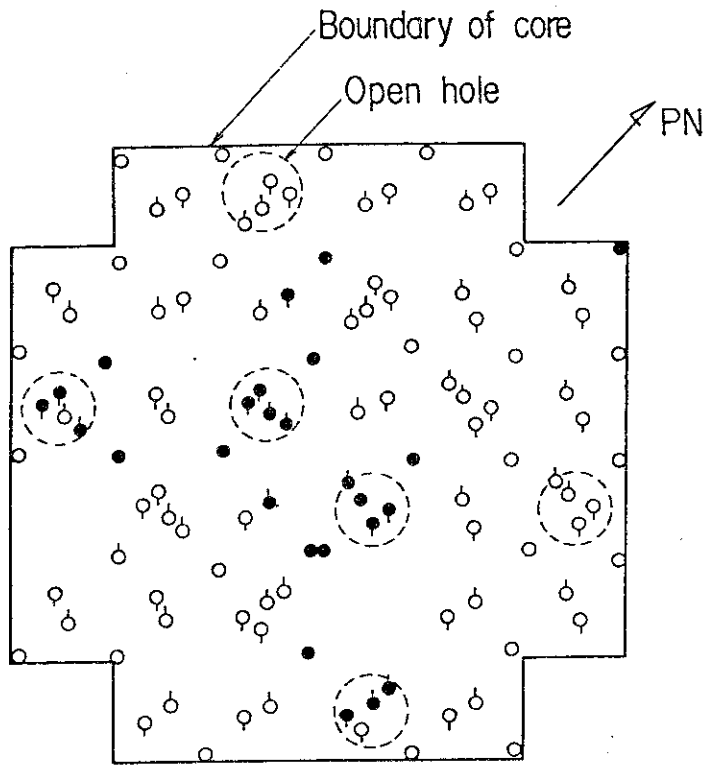

♀ High power
♁ Medium power
○ Low power
○ Bottom quench
● Top quench
3.05 m Elevation

Fig. 10 Relationship of top-quenched rods and open holes in base case test

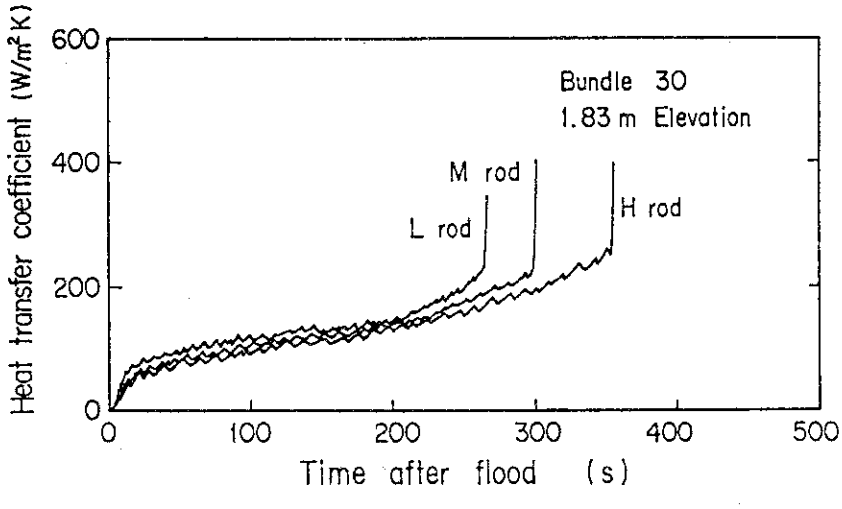

Fig. 11 Comparison of heat transfer coefficients of different rods in a bundle

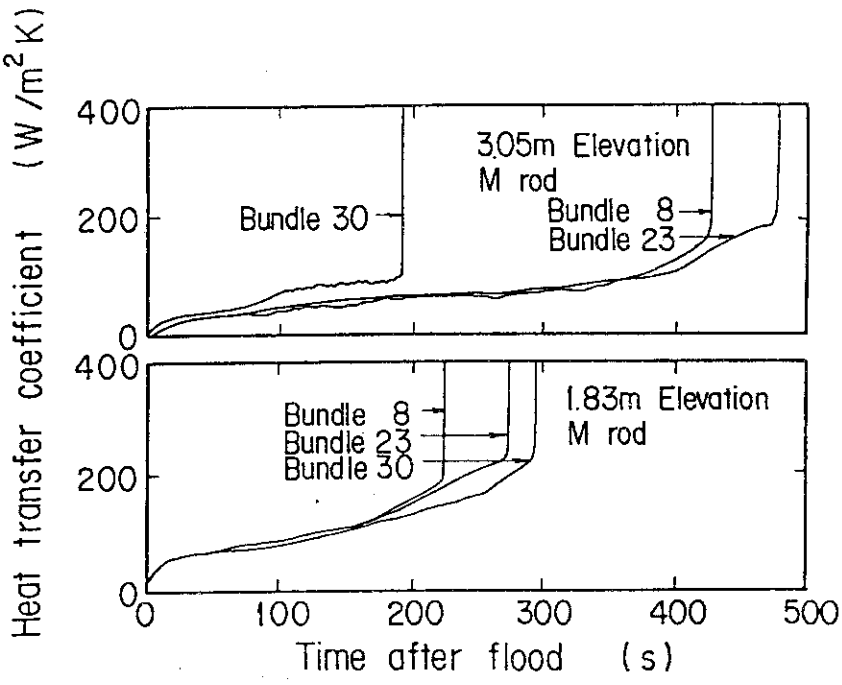

Fig. 12 Comparison of heat transfer coefficients in different bundles

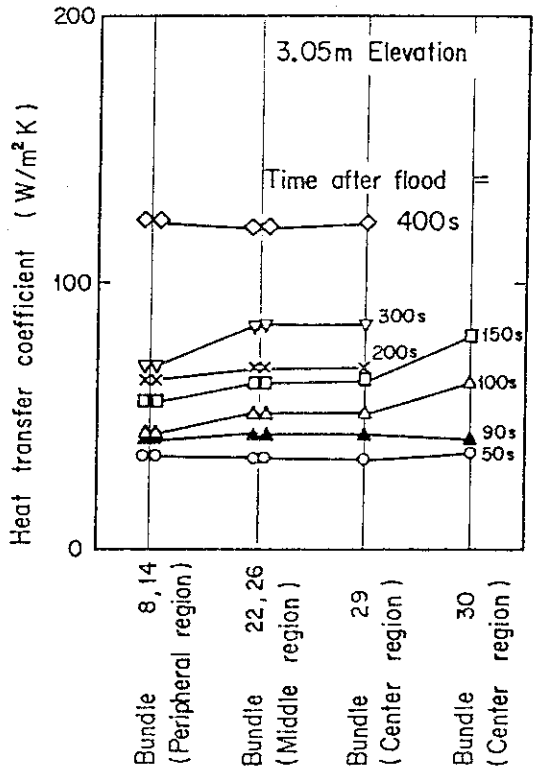

Fig. 13 Corewise distribution of heat transfer coefficient

Note ▨ Hatched band shows the scattering range of four readings of the differential pressures measured at four orientations (DPC1~4 in Fig.1)

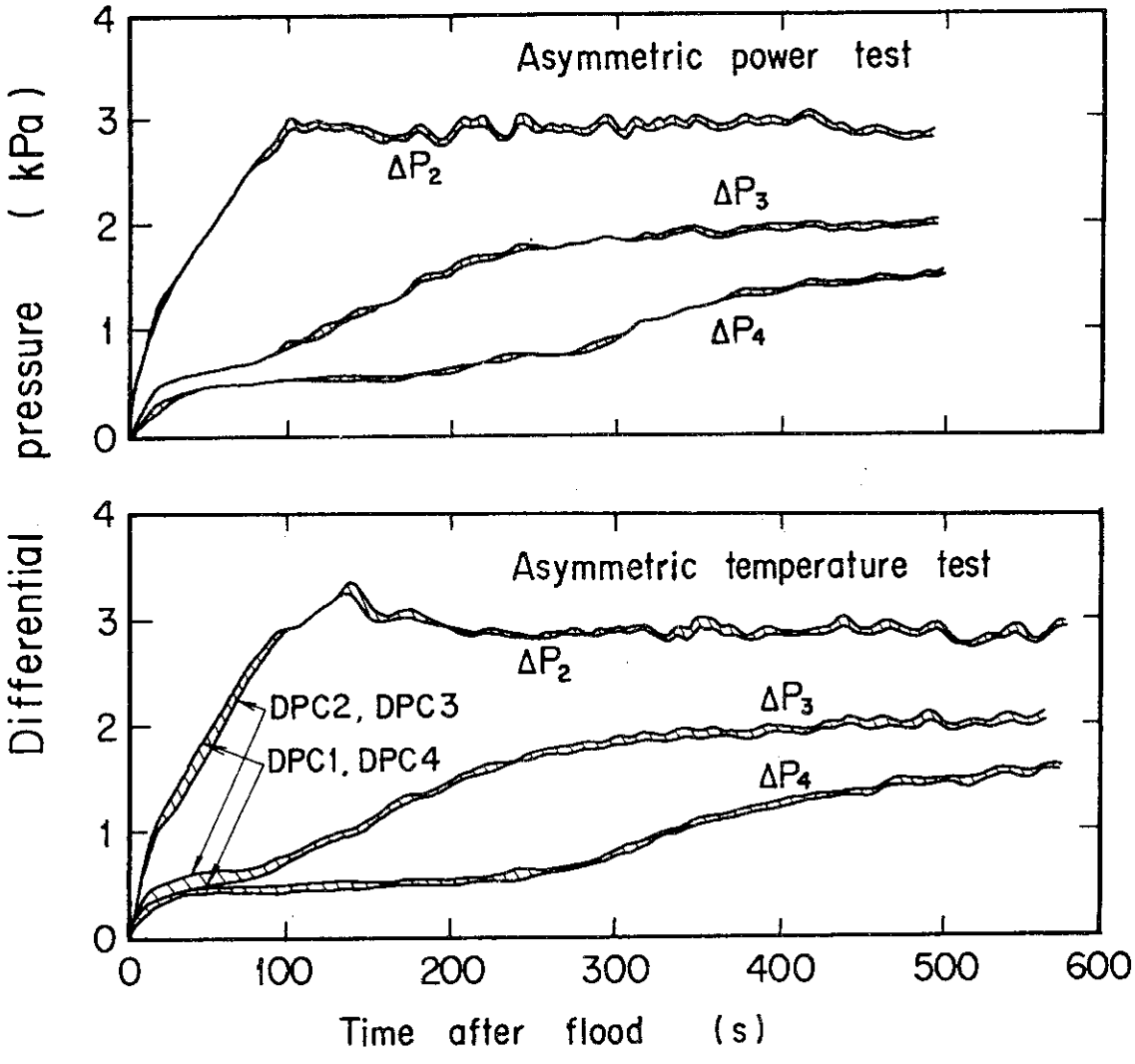

Fig. 14 Uniformity of differential pressures in core in Asymmetric power test and Asymmetric temperature test

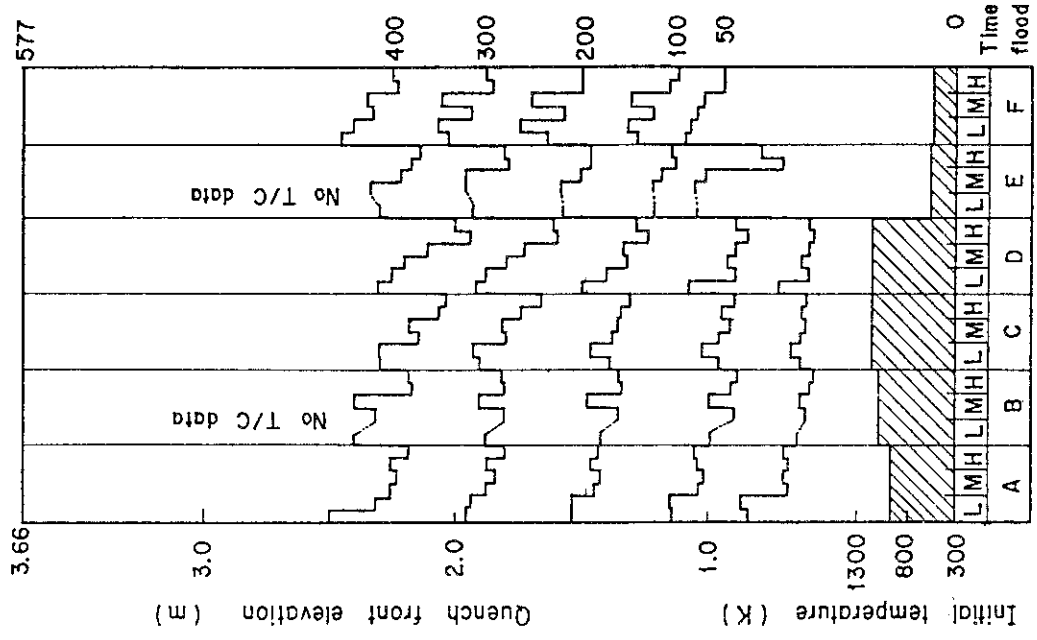

Note 1) A, B, C, D, E, F : Bundle identification (See Fig. 1)
2) L, M, H : Power level identification
L Low power rod
M Medium power rod
H High power rod

Fig. 16 Quench front propagation of Asymmetric temperature test

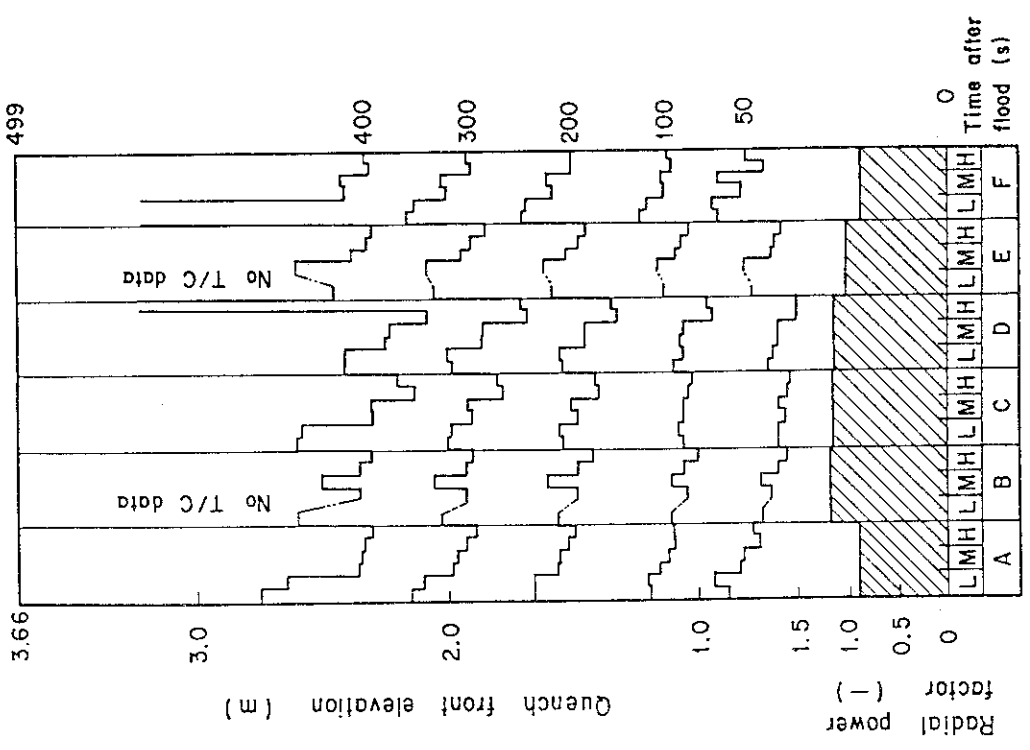

Note 1) A, B, C, D, E, F : Bundle identification (See Fig. 1)
2) L, M, H : Power level identification
L Low power rod
M Medium power rod
H High power rod

Fig. 15 Quench front propagation of Asymmetric power test

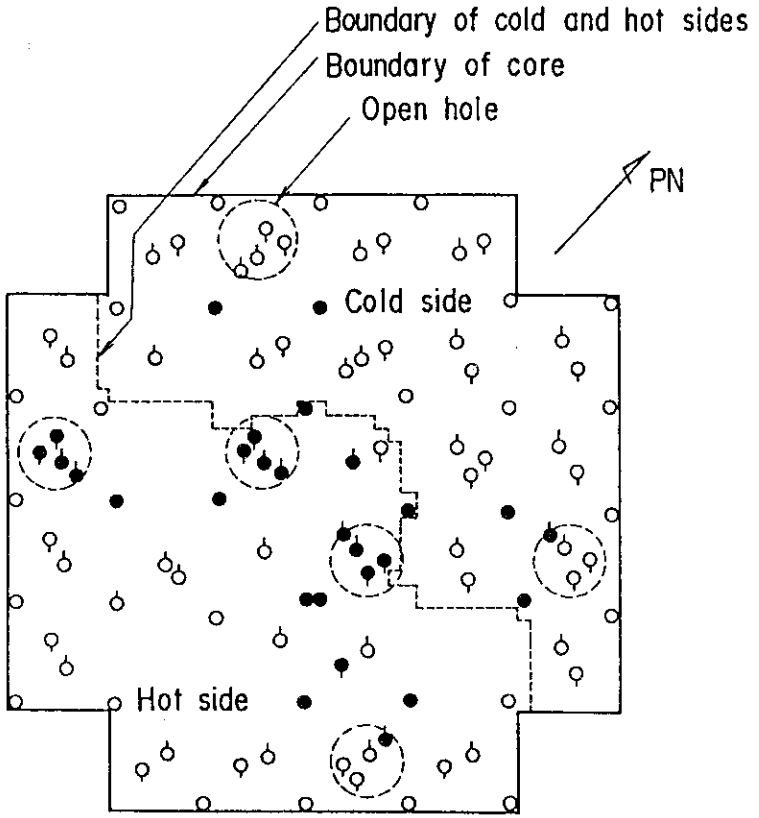

○ High power
◇ Medium power
○ Low power
○ Bottom quench
● Top quench
3.05 m Elevation

Fig.17 Relationship of top-quenched rods and open holes in Asymmetric power test

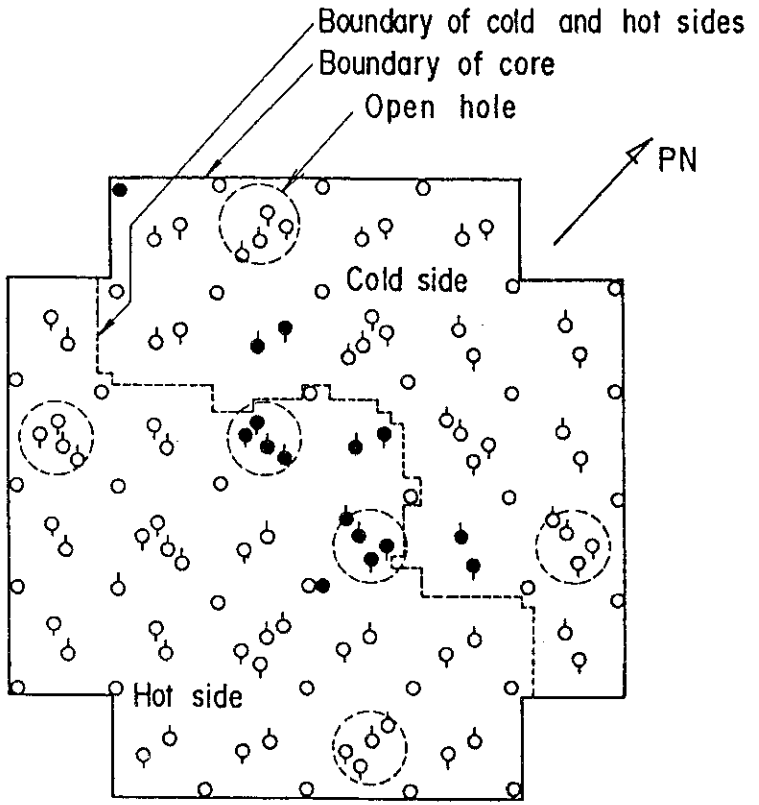

○ High power
◇ Medium power
○ Low power
○ Bottom quench
● Top quench
3.05 m Elevation

Fig. 18 Relationship of top-quenched rods and open holes in Asymmetric temperature test

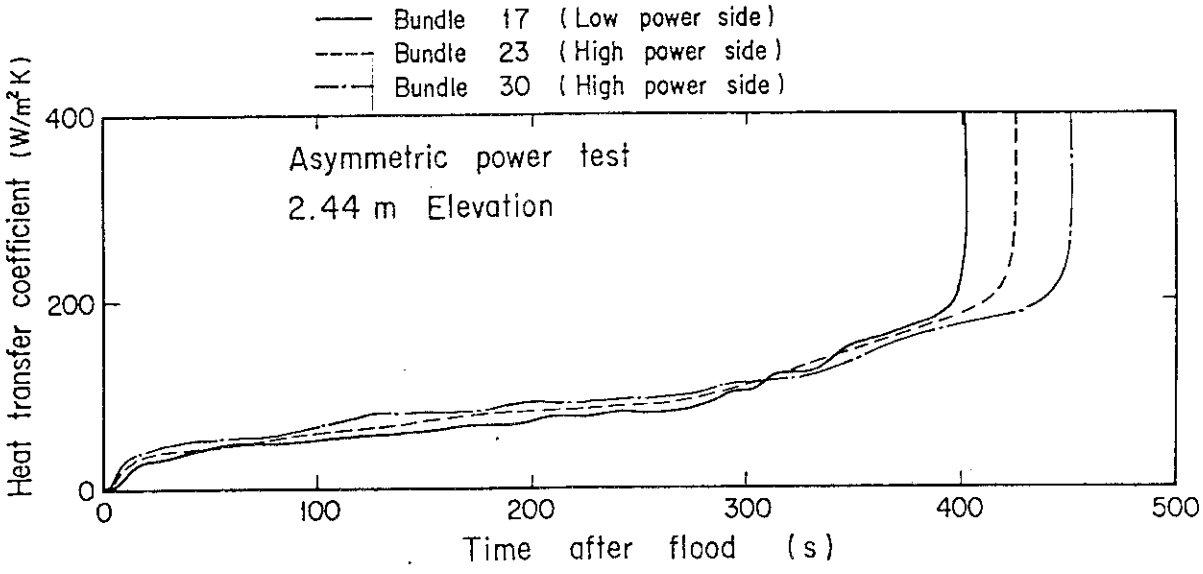

Fig. 19 Comparison of heat transfer coefficients in different bundles in Asymmetnc power test

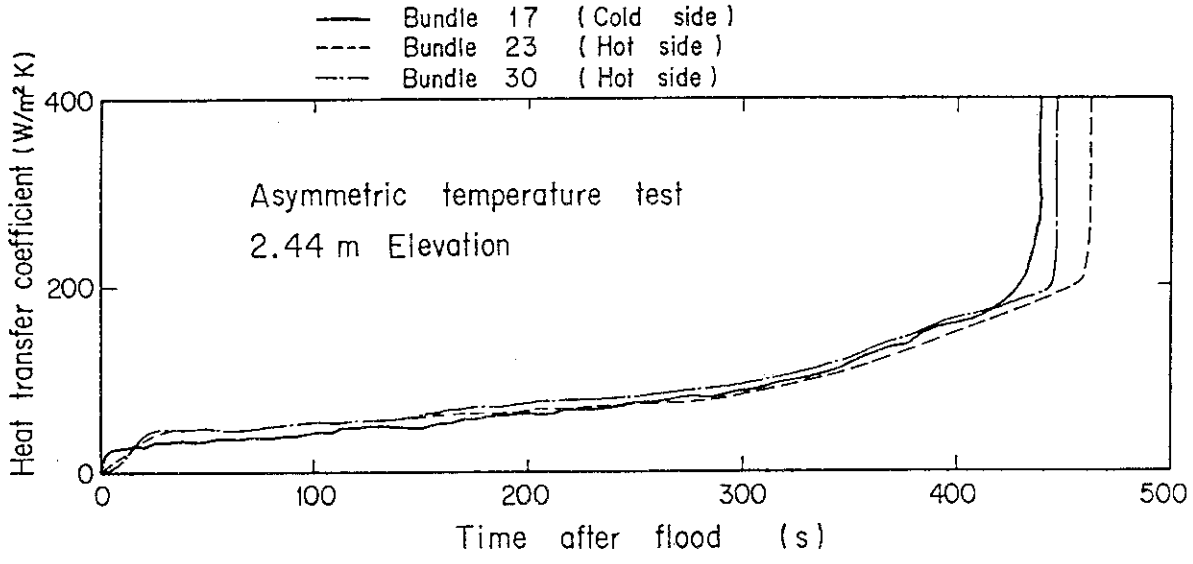

Fig. 20 Comparison of heat transfer coefficients in different bundles in Asymmetric temperature test at 2.44 m elevation

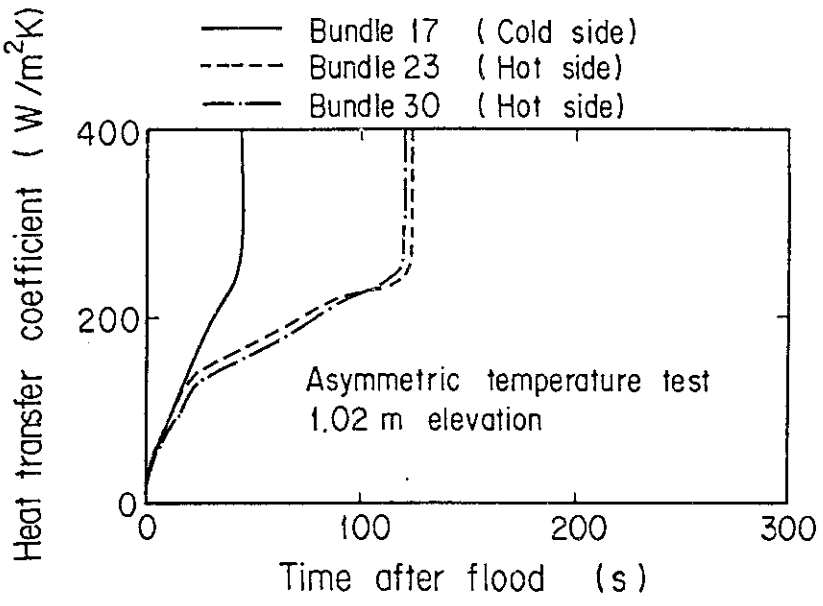

Fig. 21 Comparison of heat transfer coefficients in different bundles in Asymmetric temperature test at 1.02 m elevation

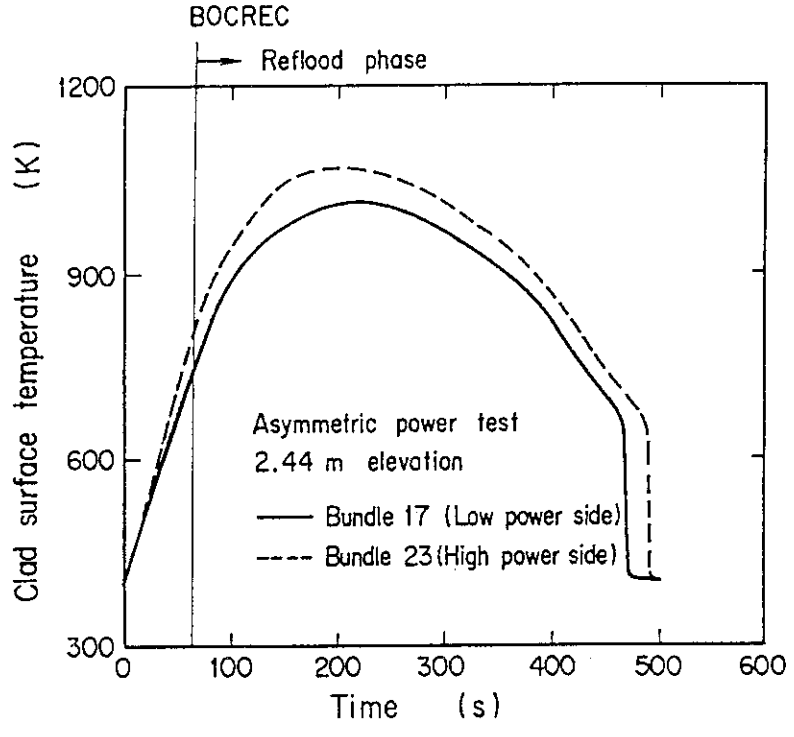

Fig. 22 Clad surface temperatures in different bundles in Asymmetric power test

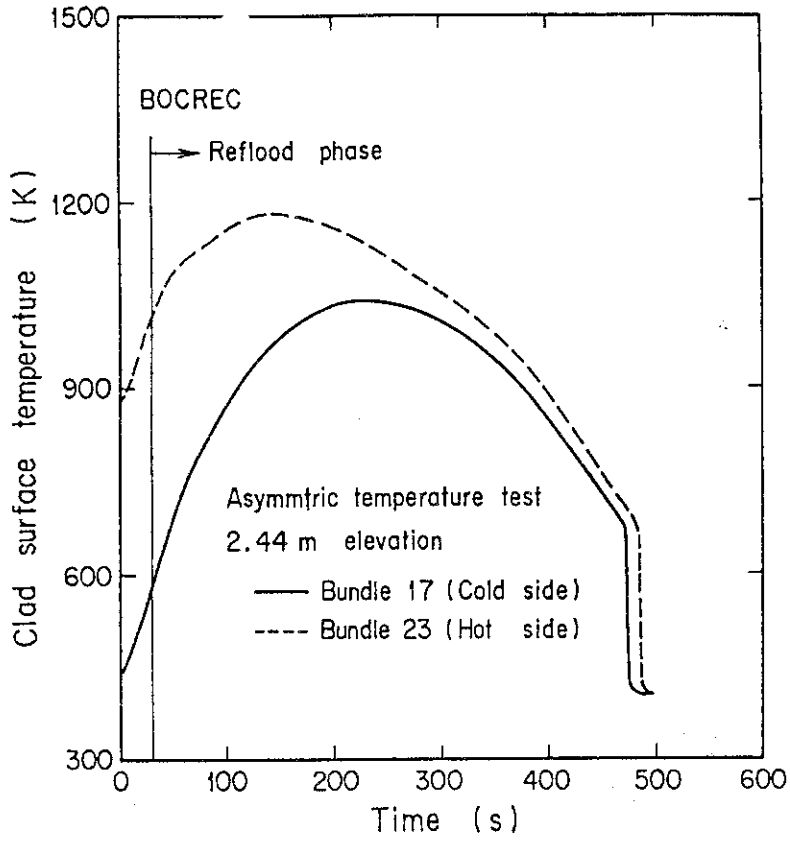

Fig. 23 Clad surface temperatures in different bundles in Asymmetric temperature test

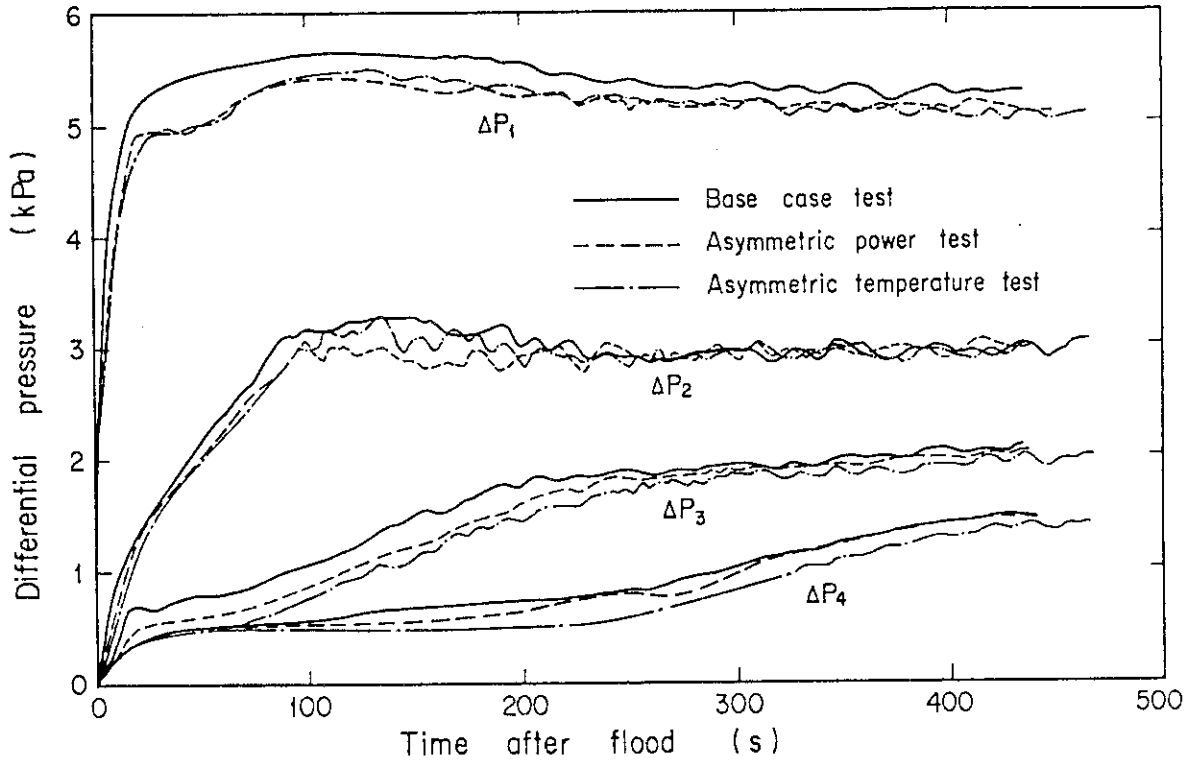

Fig. 24 Comparison of core differential pressures at various elevations among base case test and thermally asymmetric tests

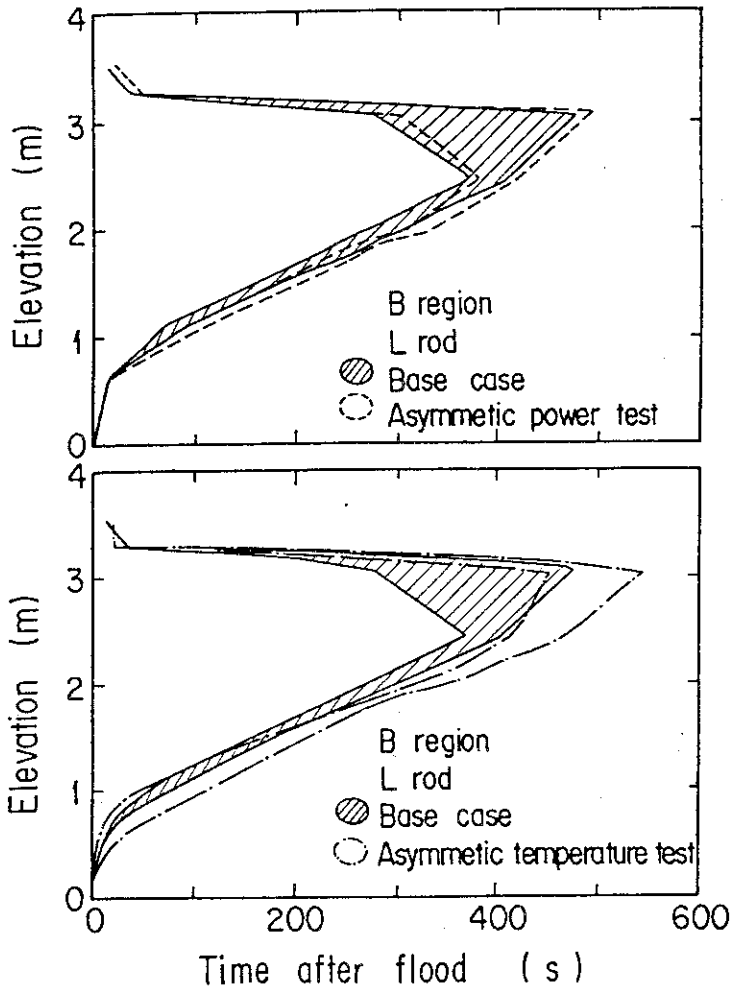

Fig. 25 Comparison of quench front propagations among base case test and thermally asymmetric tests

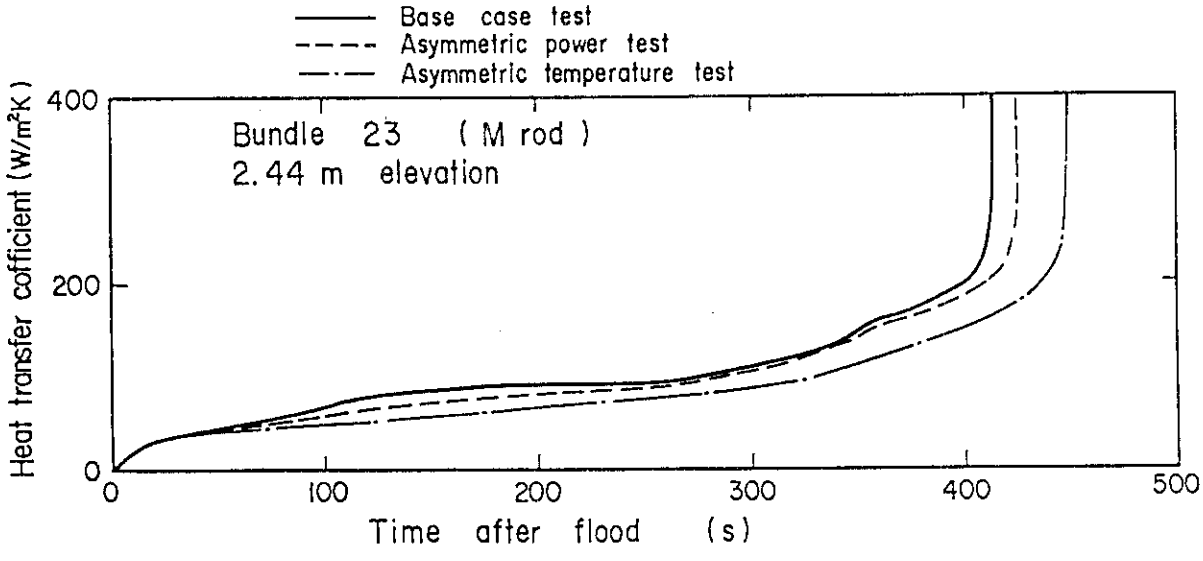

Fig. 26 Comparison of heat transfer coefficients among base case test and thermally asymmetric tests

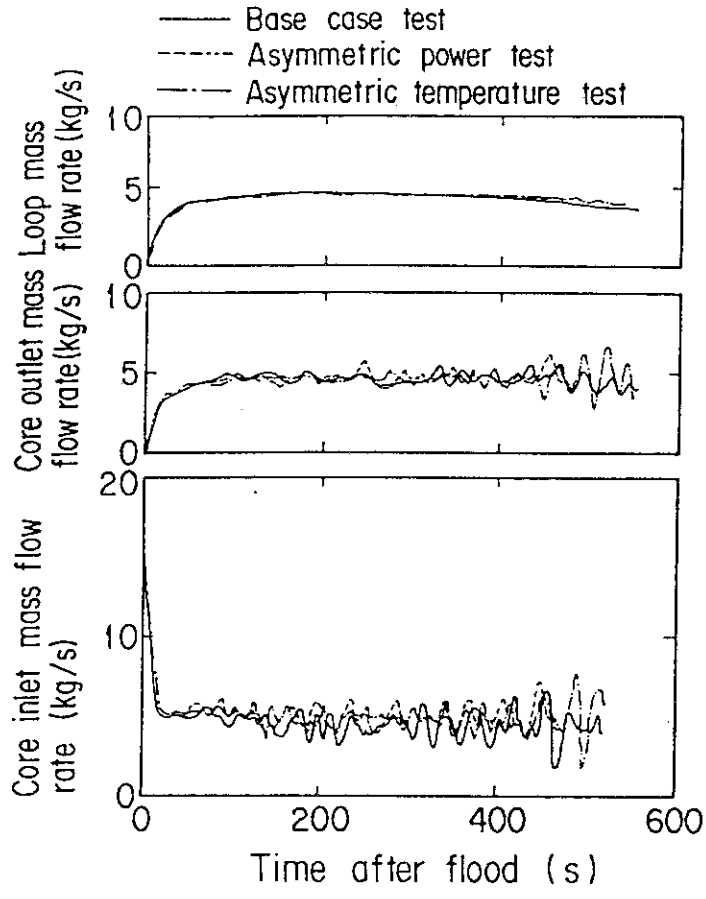

Fig. 27 Comparison of mass flow rates among base case test and thermally asymmetric tests

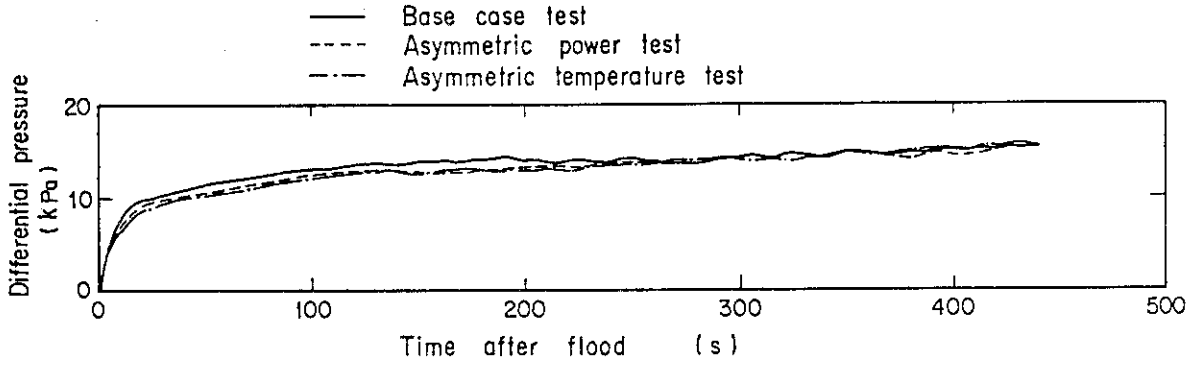

Fig. 28 Comparison of core water accumulations among base case test and thermally asymmetric tests

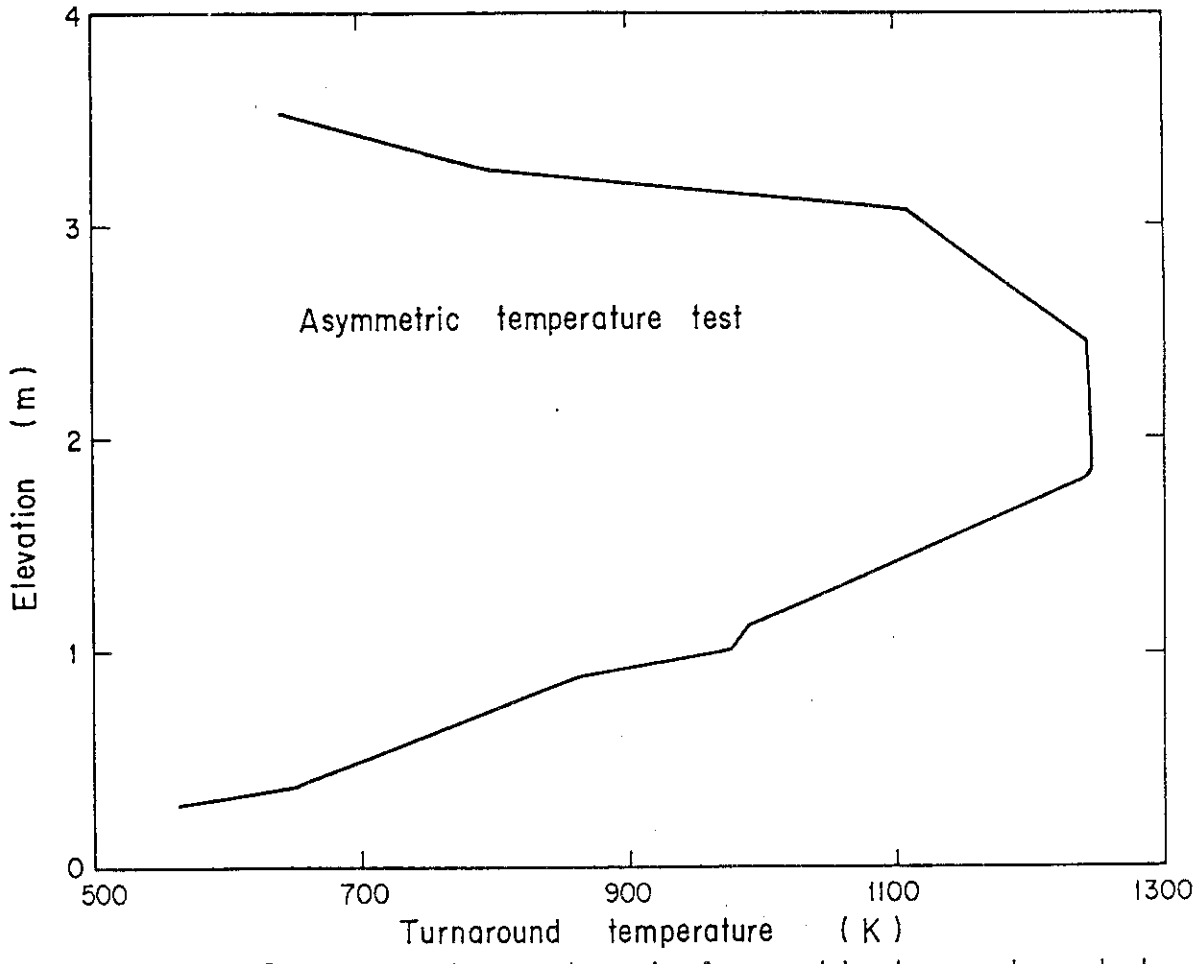

Fig. 29 Turnaround temperature in Asymmetric temperature test

Appendix A

Explanation of measuring location of referred data and definition of the evaluated data

Figure list

1. Definition of Tag.ID for clad surface temperatures

Notation : TENNWAM

NN : Bundle number

WA : Power zone

WA = X1, X2 : High power (Local power factor 1.1)

WA = Y1, Y2 : Medium power (Local power factor 1.0)

WA = Z1, Z2 : Low power (Local power factor 0.95)

M : Elevation

M	Elevation (m)	Axial power factor
1	0.38	0.568
2	1.015	1.176
3	1.83	1.492
4	2.44	1.312
5	3.05	0.815

2. Definition of power zone and bundle number

See Fig. A-1

3. Definition of Tag.ID for void fraction

See Fig. A-2

4. Definition of Tag.ID for average linear power of heater rod in each power unit zone

See Fig. A-3

5. Definition of carry-over rate fraction (C.R.F)

$$CRF = \frac{\dot{m}_{UP} + \dot{m}_{L}}{\dot{m}_{CR} + \dot{m}_{UP} + \dot{m}_{L}}$$

The calculated data within ±25 s are averaged:

$$(CRF)_i = \frac{1}{101} \sum_{k=i-50}^{i+50} (CRF)_k$$

where

ΔP_{UP} : Average of measured data at four orientations

ΔP_{CR} : Same as above

$$\dot{m}_{UP} = A_{up} \frac{d}{dt} (\Delta P_{UP})$$

$$\dot{m}_{CR} = A_{CR} \frac{d}{dt} (\Delta P_{CR})$$

$$\dot{m}_L = \sum_{k=1}^{4} \dot{m}_{pk}$$

$\dot{m}$: mass flow rate or mass accumulation rate

ΔP: differential pressure

suffix

UP: upper plenum

CR: core

L : loop

p : primary pump

6. Definition of Tag.ID for differential pressure through downcomer, upper plenum, core and lower plenum

   See Fig. A-4

7. Definition of Tag.ID for differential pressure through intact and broken loop and broken cold leg nozzle

   See Fig. A-5

8. Definition of Tag.ID for fluid temperature in inlet and outlet plenum and secondary of steam generator

   See Fig. A-6

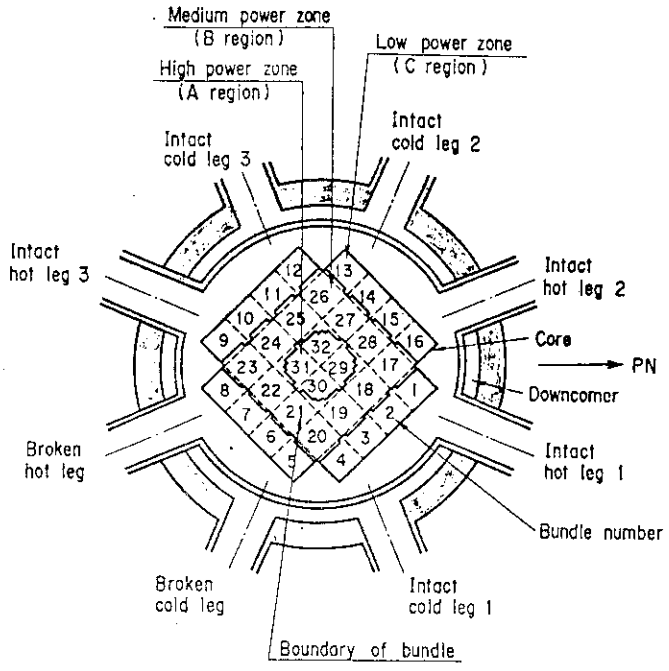

Fig.A-1 Definition of power zones and bundle numbers

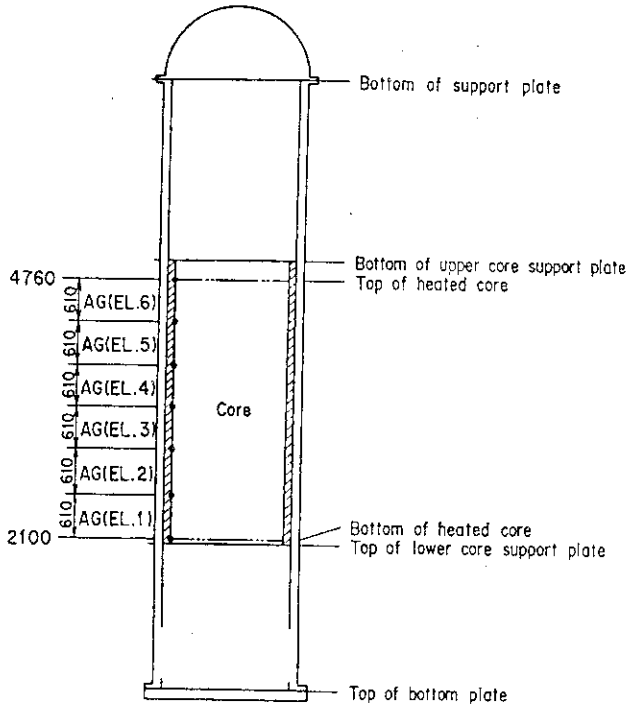

Fig.A-2 Definition of Tag.ID for void fraction (AG(EL.1)～AG(EL.6))

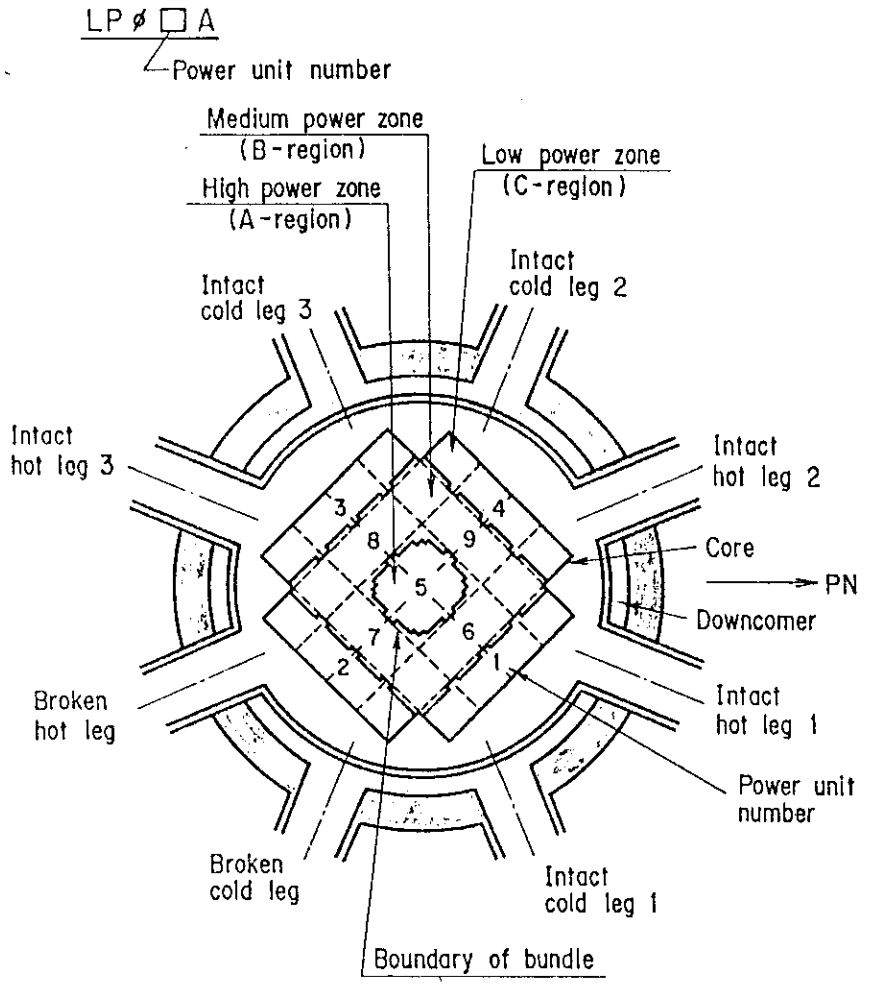

Fig. A-3 Definition of Tag. ID for average linear power of heater rod in each power unit zone (LP01A ~ LP09A)

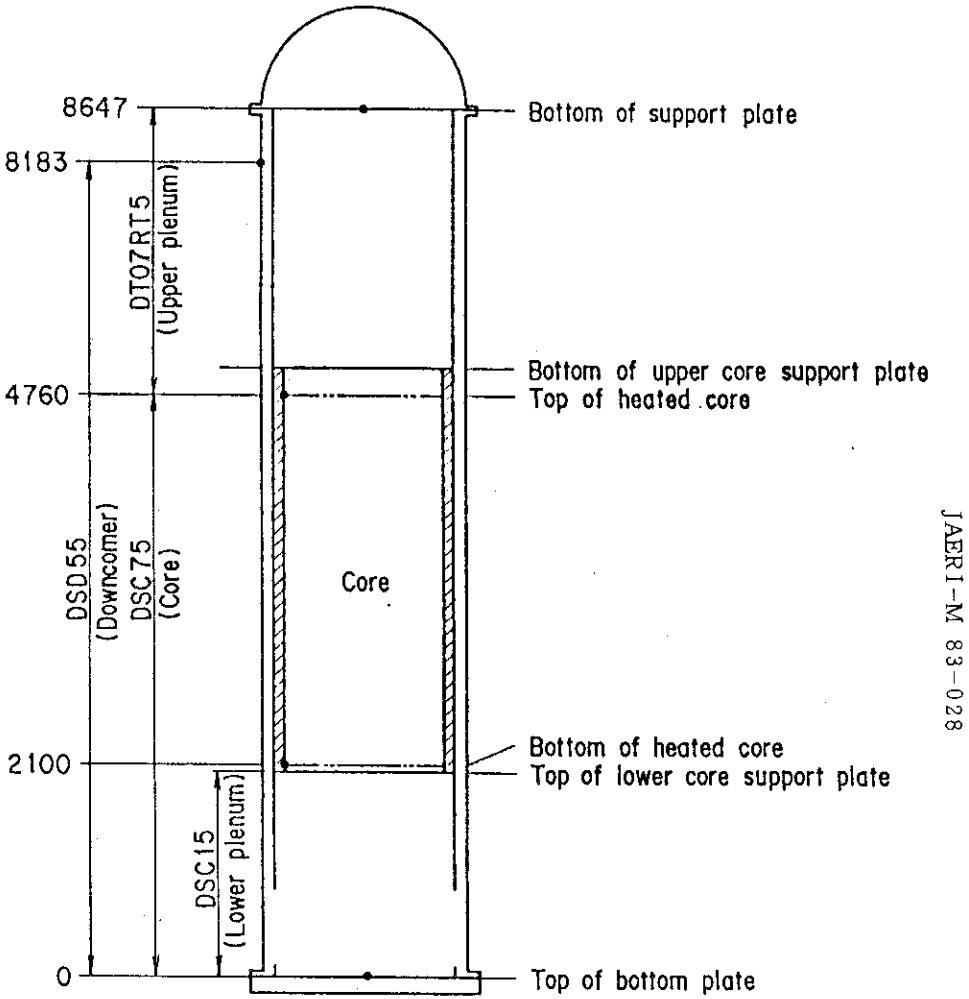

Fig. A-4 Definition of Tag. ID for differential pressure through downcomer, upper plenum, core, and lower plenum (DSD55, DT07RT5, DSC75, DSC15)

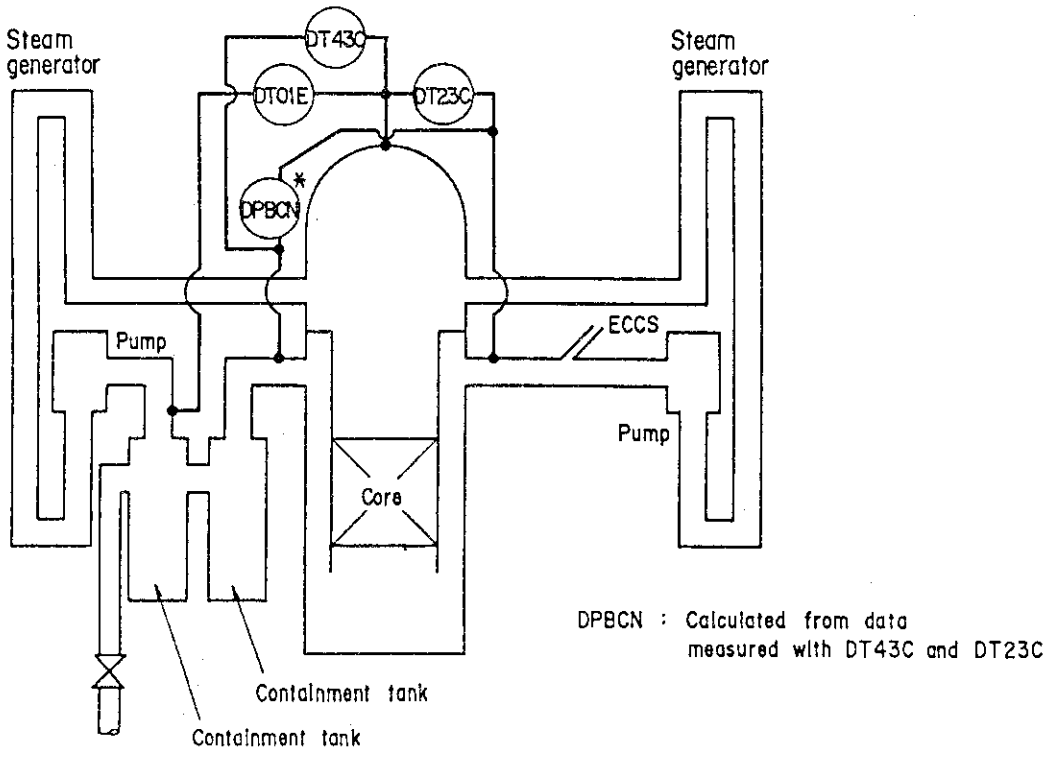

Fig. A-5 Definition of Tag. ID for differential pressure through intact and broken loop and broken cold leg nozzle (DT23C, DT01B, DPBCN)

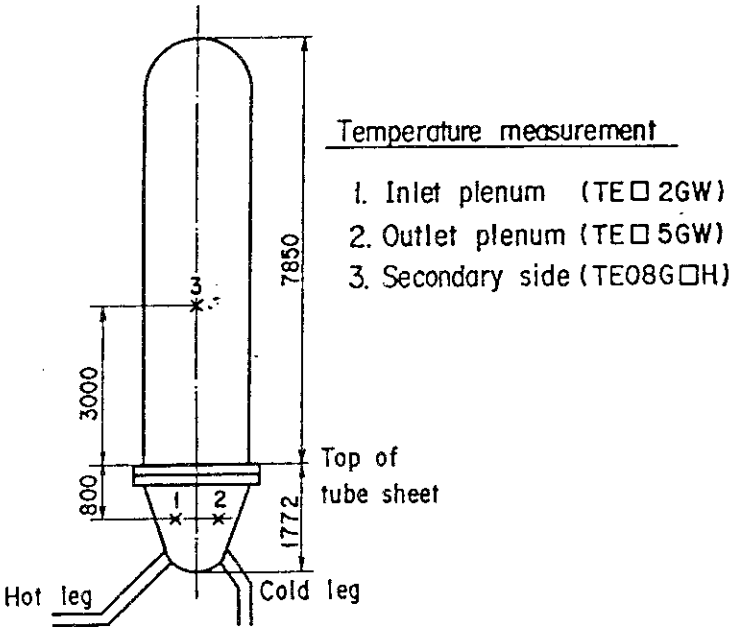

Fig. A-6 Definition of Tag. ID for fluid temperature in inlet and outlet plenum and secondary of steam generator (TE□2GW, TE□5GW, TE08G□H)

Appendix B

Main results of test C1-17 (Run 36)

Table and Figure List

Table B-1 Summary of test conditions

1. TEST TYPE : ASSYMMETRICAL CORE HEATING TEST
2. TEST NUMBER : RUN 036 3. DATE : Mar.3, 1981
4. POWER : A: TOTAL: 9.39 MW; B:LINEAR: 1.41 KW/M
5. RELATIVE RADIAL POWER SHAPE :

   A: ZONE: A B C

   B: RATIO: — — —
6. AXIAL POWER SHAPE : CHOPPED COSINE
7. PRESSURE (KG/CM^2A) :

   A: SYSTEM: 2.0, B: CONTAINMENT 2.07,

   C: STEAM GENERATOR SECONDARY: 53.9
8. TEMPERATURE (DEG.C) :

   A: DOWNCOMER WALL 166, B: VESSEL INTERNALS 122,

   C: PRIMARY PIPING WALL 121, D: LOWER PELNUM LIQUID 121,

   E: ECC LIQUID 38.8, F: STEAM GENERATOR SECONDARY 263,

   G: CORE TEMPERATURE AT ECC INITIATION 522
9. ECC INJECTION TYPE: C

   A: COLD LEG, B: LOWER PLENUM, C: LOWER PLENUM + COLD LEG
10. PUMP K-FACTOR : $\sim$ 15
11. ECC FLOW RATES AND DURATION :

    A: ACCUMULATOR 284 M^3/HR FROM 0 TO 23 SECONDS

    B: LPCI 30.2 M^3/HR FROM 23 TO 708 SECONDS

    C: ECC INJECTION TO LOWER PLENUM : FROM 0 TO 17 SECONDS

    (VALVE OPENING AND CLOSING TIMES ARE INCLUDED IN THE INJECTION DURATION)
12. INITIAL WATER LEVEL IN LOWER PLENUM : 0.87 M.
13. POWER CONTROL : ANS x 1.2 + ACTINIDE (30 SEC AFTER SCRAM)
14. EXPECTED BOCREC TIME FROM ECC INITIATION 12 SEC
15. EXPECTED PEAK TEMPERATURE AT BOCREC 600 C

Table B-2 Chronology of events

EVENT	TIME (sec)
Test Initiated (Heater Rods Power on) (Data Recording Initiated)	0
Accumulator Injection Initiated	52
Power Decay Initiated (Bottom of Core Recovery)	64.5 (63.5)
Accumulator Injection Switched from Lower Plenum to Cold Leg	69
Accumulator Injection Ended and LPCI Injection Initiated	75
All Heater Rods Quenched	—
Power Off	562.5
LPCI Injection Ended	760
Test Ended (Data Recording Ended)	562.5

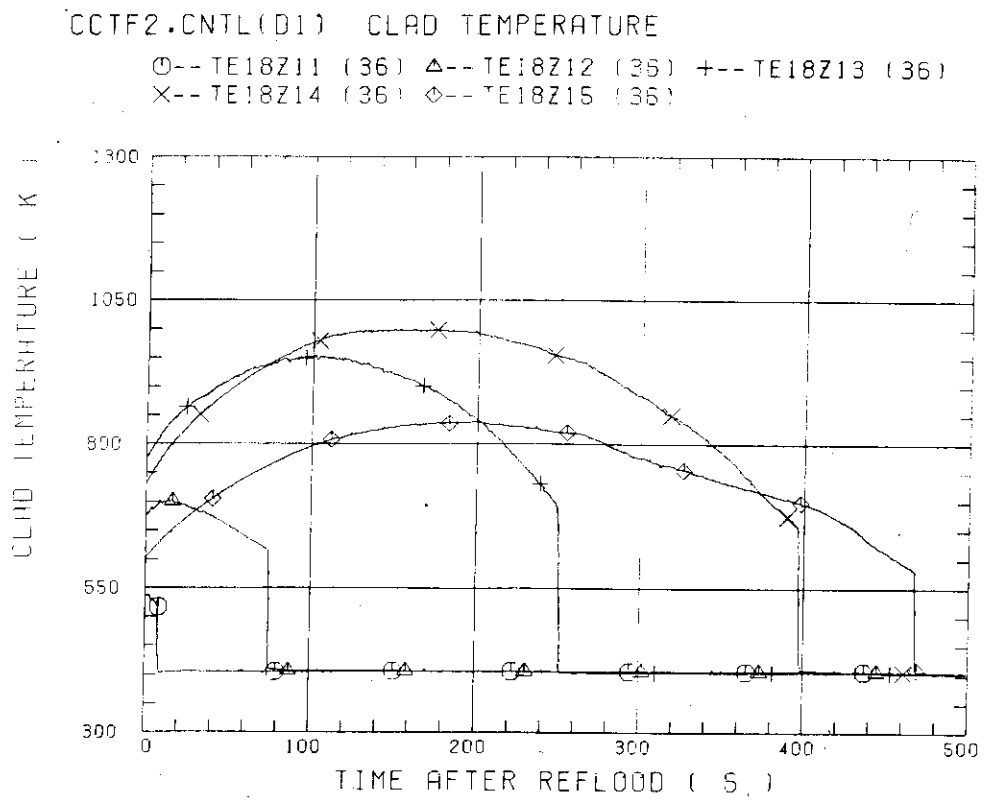

Fig. B-1 Surface temperature on medium power rod (Y-rod) in medium power region (B region)

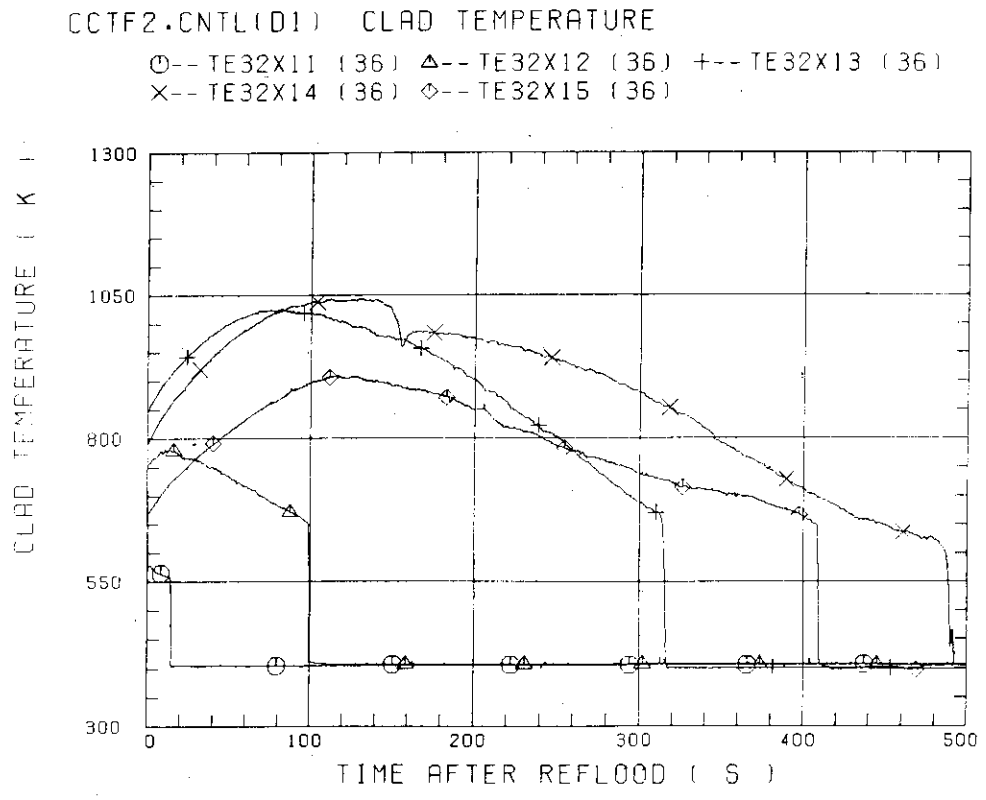

Fig. B-2 Surface temperature on high power rod (X-rod) in high power region (A region)

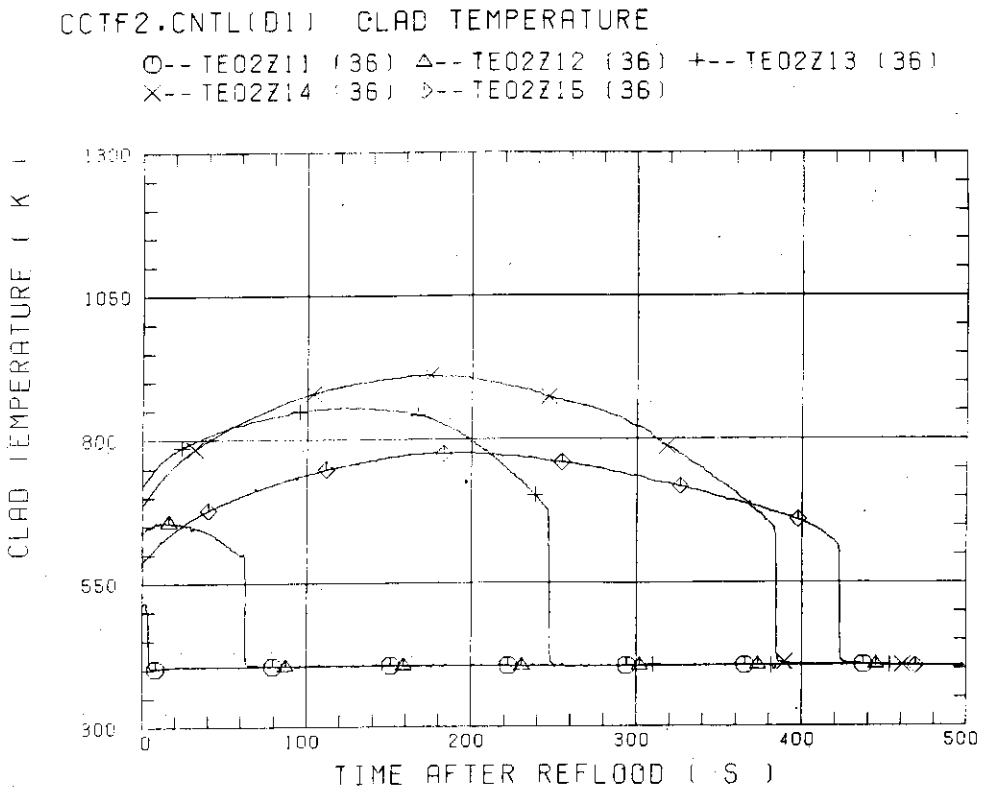

Fig. B-3 Surface temperature on low power rod (Z-rod) in low power region (C region) (lowest power rod)

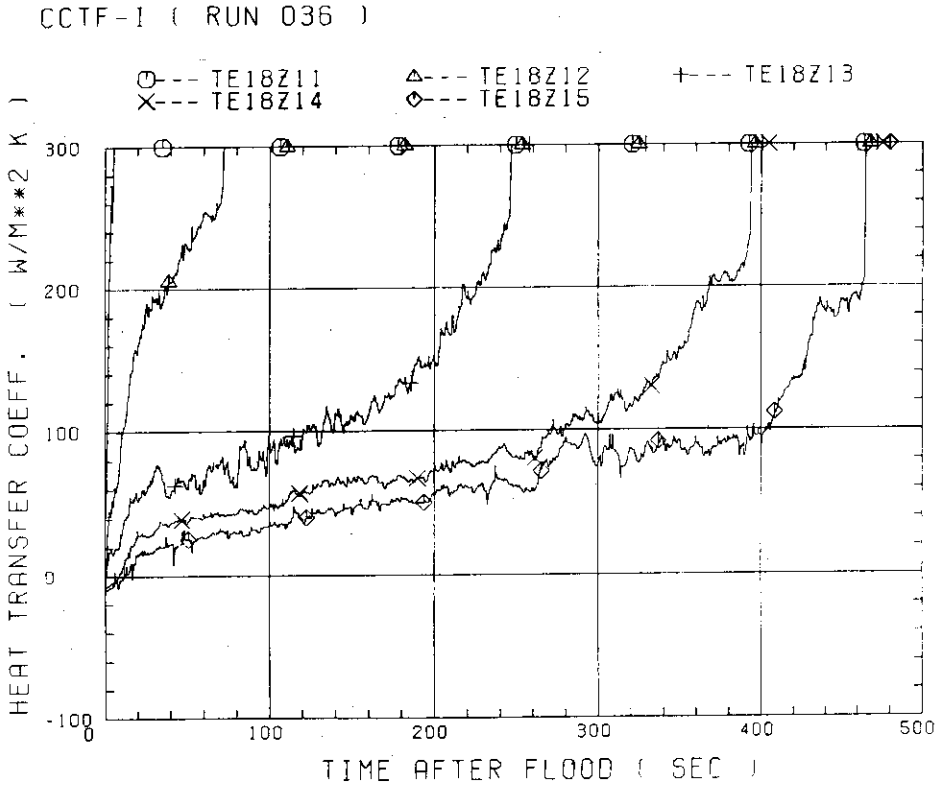

Fig. B-4 Heat transfer coefficients of low power rod (Z-rod) in medium power region (B region) (average power rod)

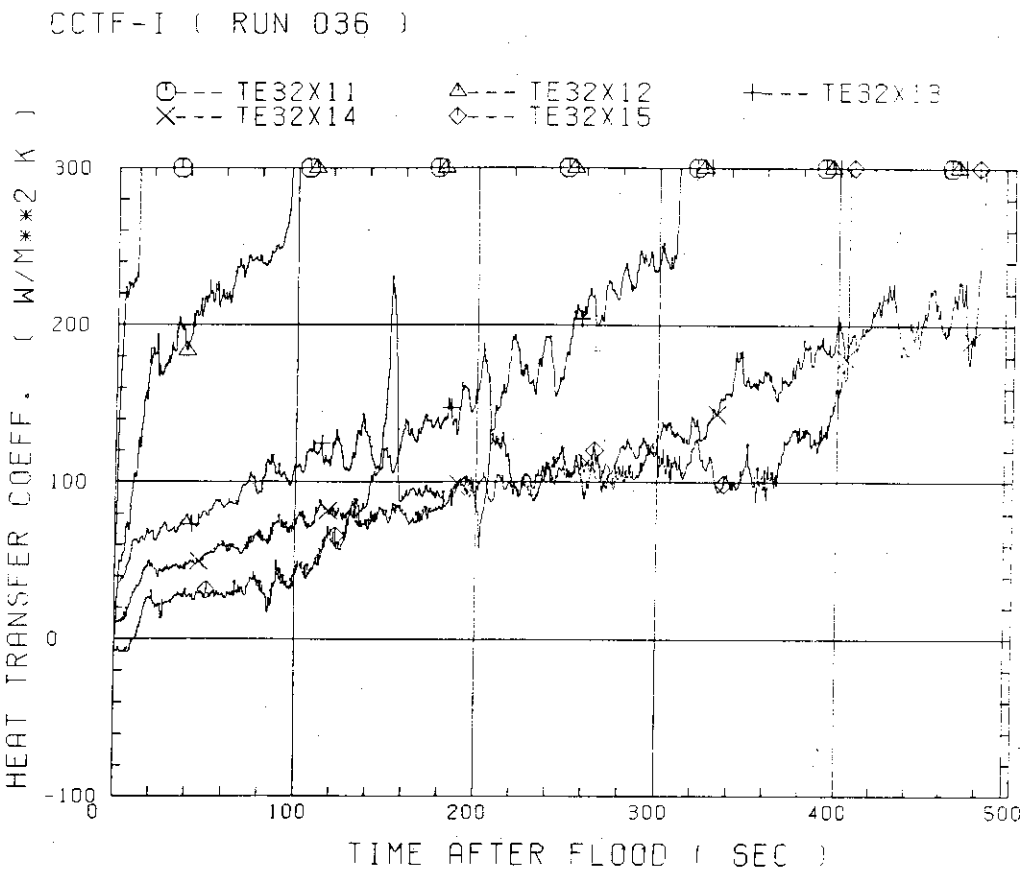

Fig. B-5 Heat transfer coefficients of high power rod (X-rod) in high power region (A region) (peak power rod)

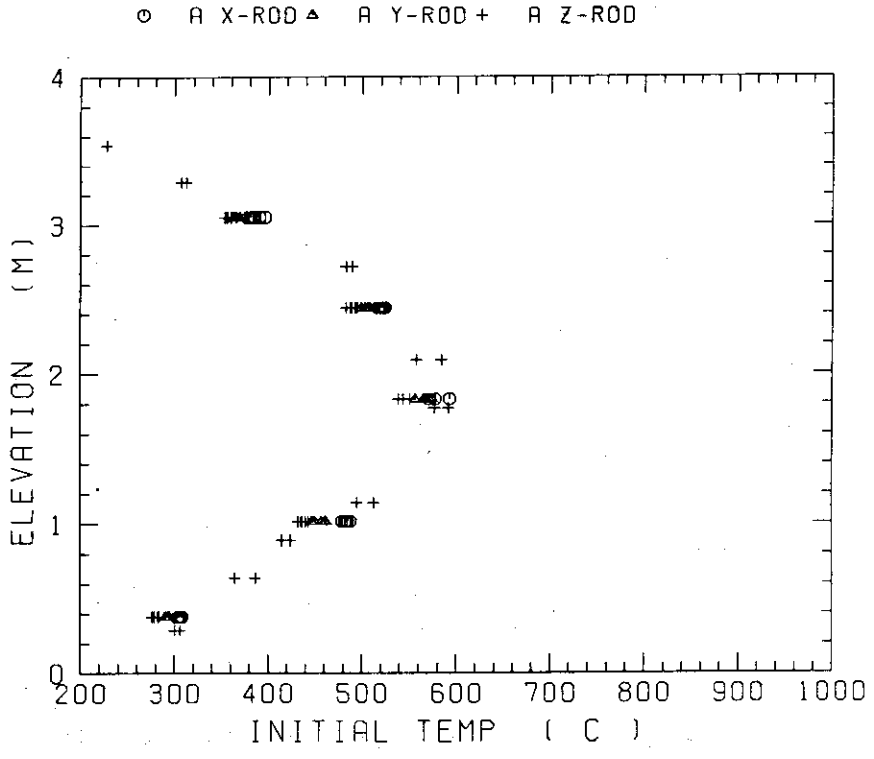

Fig. B-6 Initial rod surface temperature in high power region (A region)

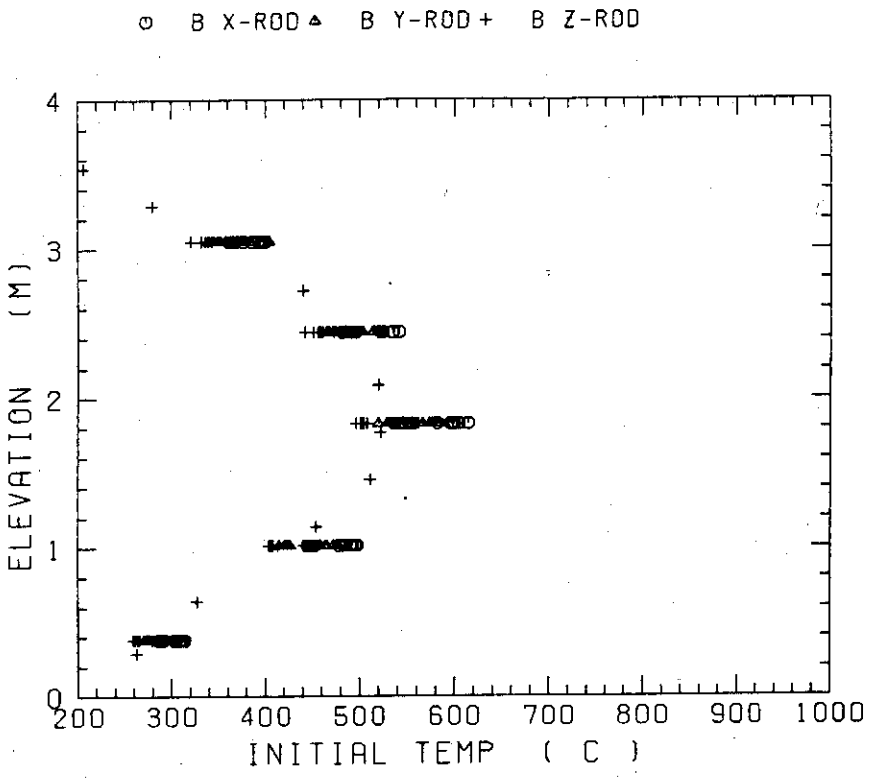

Fig. B-7 Initial rod surface temperature in medium power region (B region)

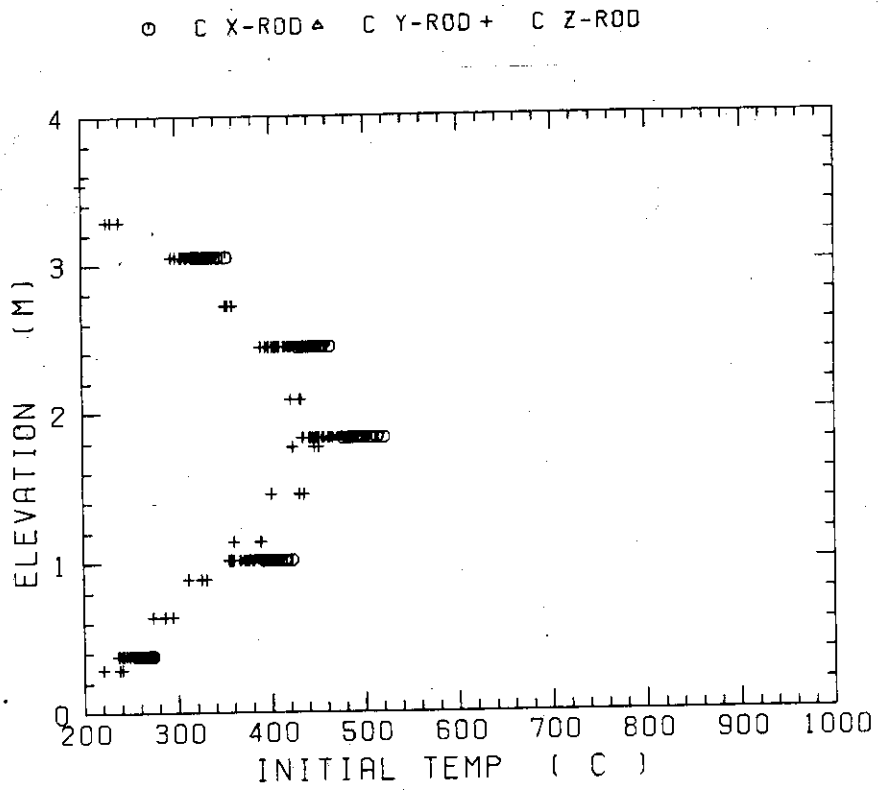

Fig. B-8 Initial rod surface temperature in low power region (C region)

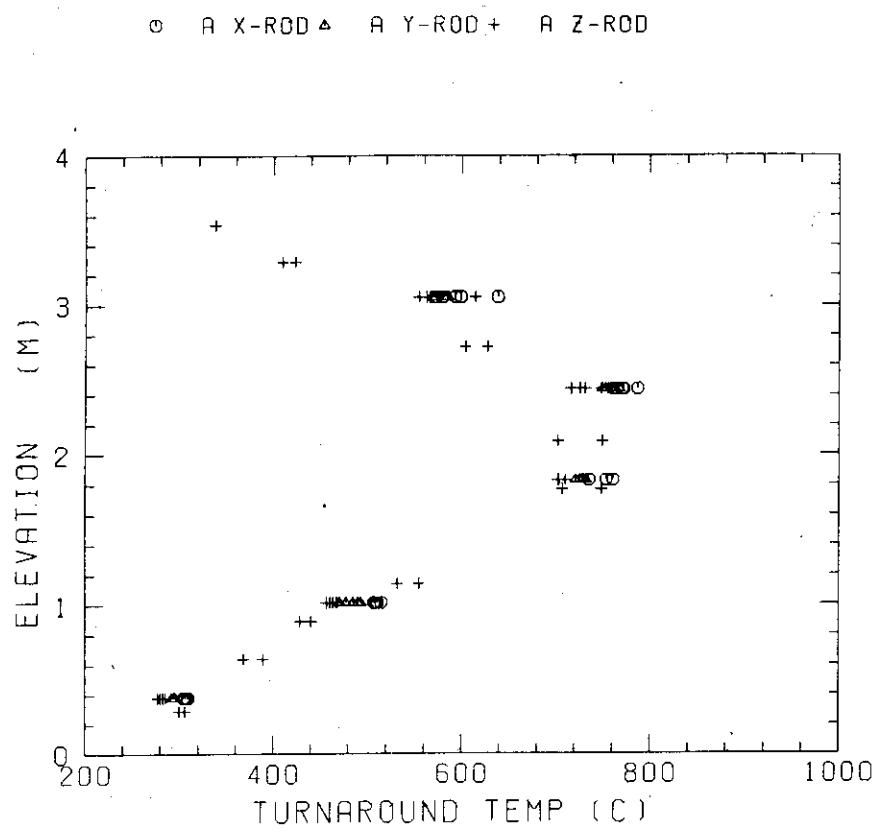

Fig. B-9 Turnaround temperature in high power region (A region)

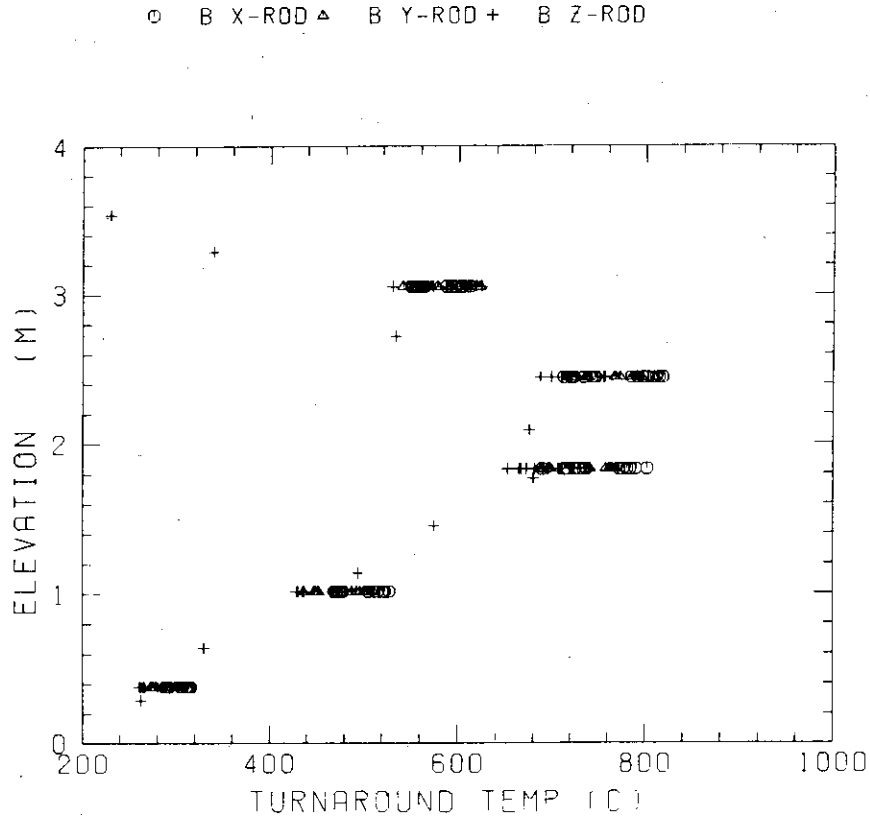

Fig. B-10 Turnaround temperature in medium power region (B region)

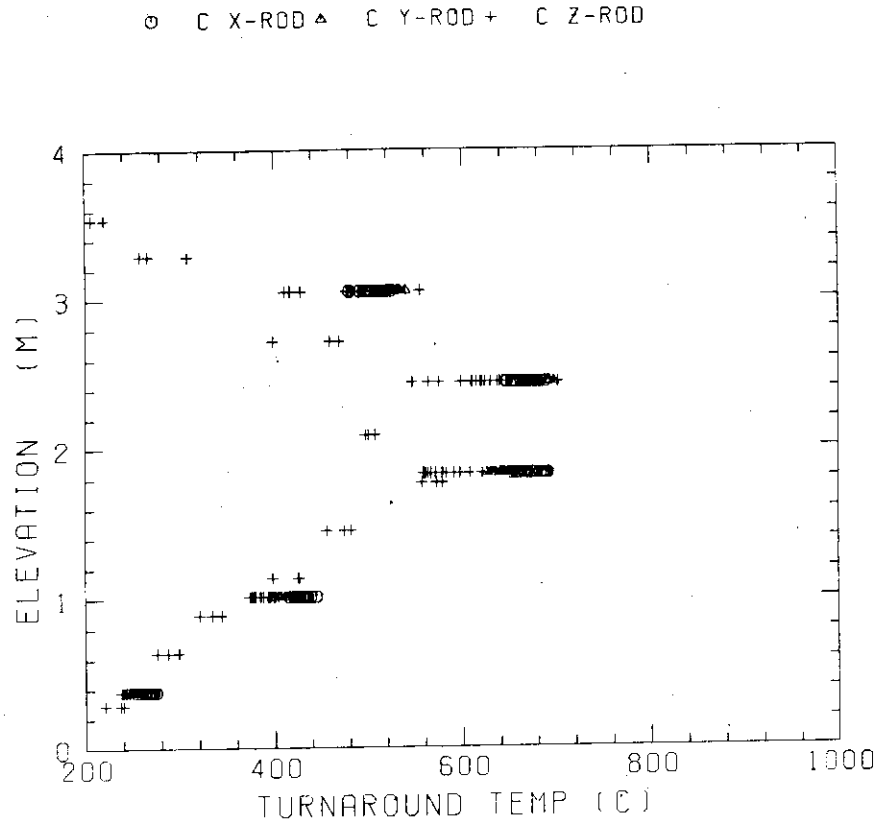

Fig. B-11 Turnaround temperature in low power region (C region)

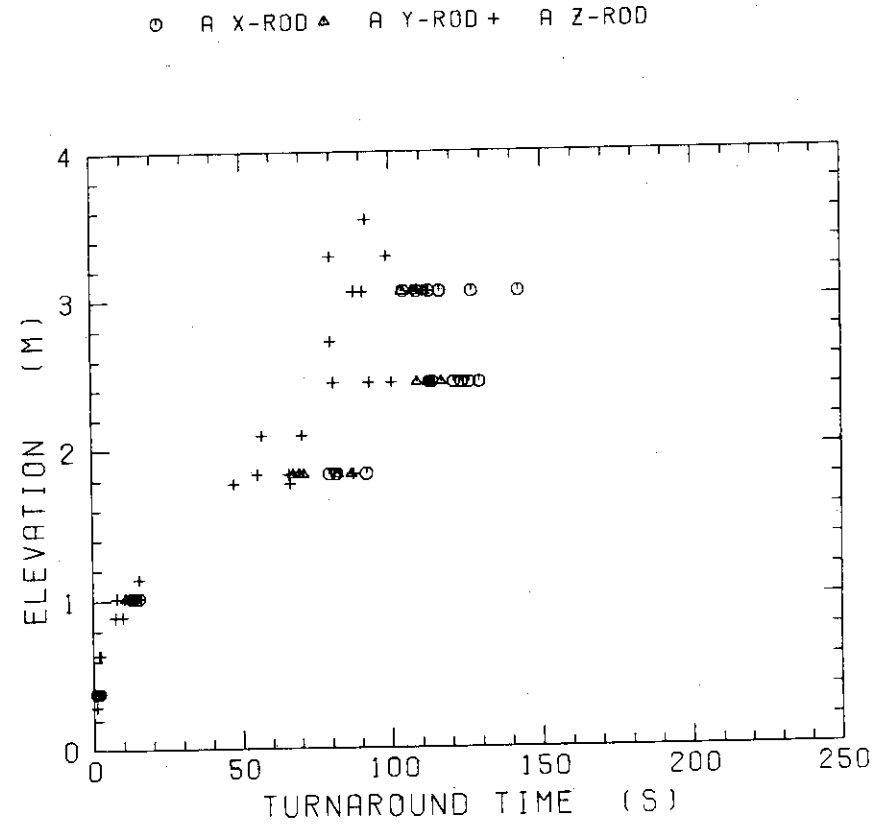

Fig. B-12 Turnaround time in high power region (A region)

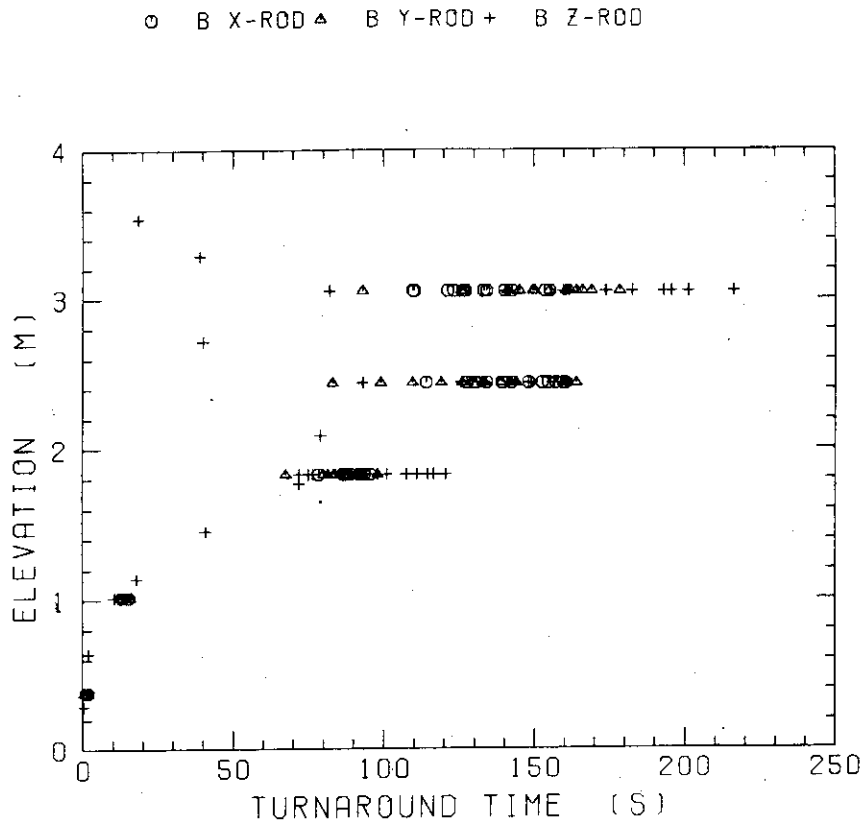

Fig. B-13 Turnaround time in medium power region (B region)

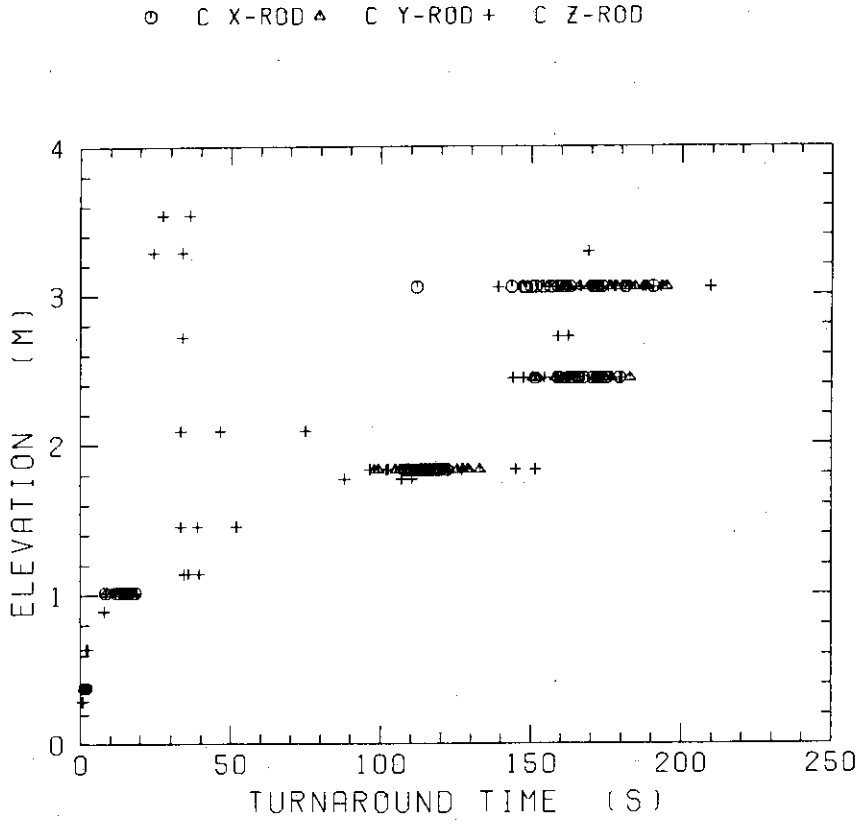

Fig. B-14 Turnaround time in low power region (C region)

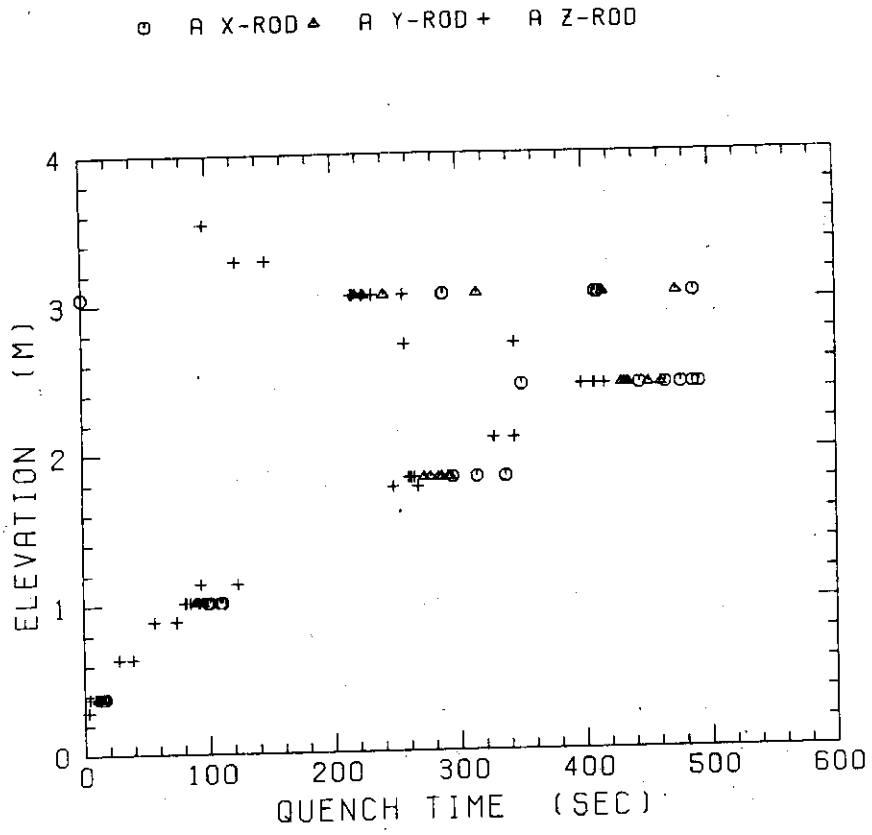

Fig. B-15 Quench temperature in high power region (A region)

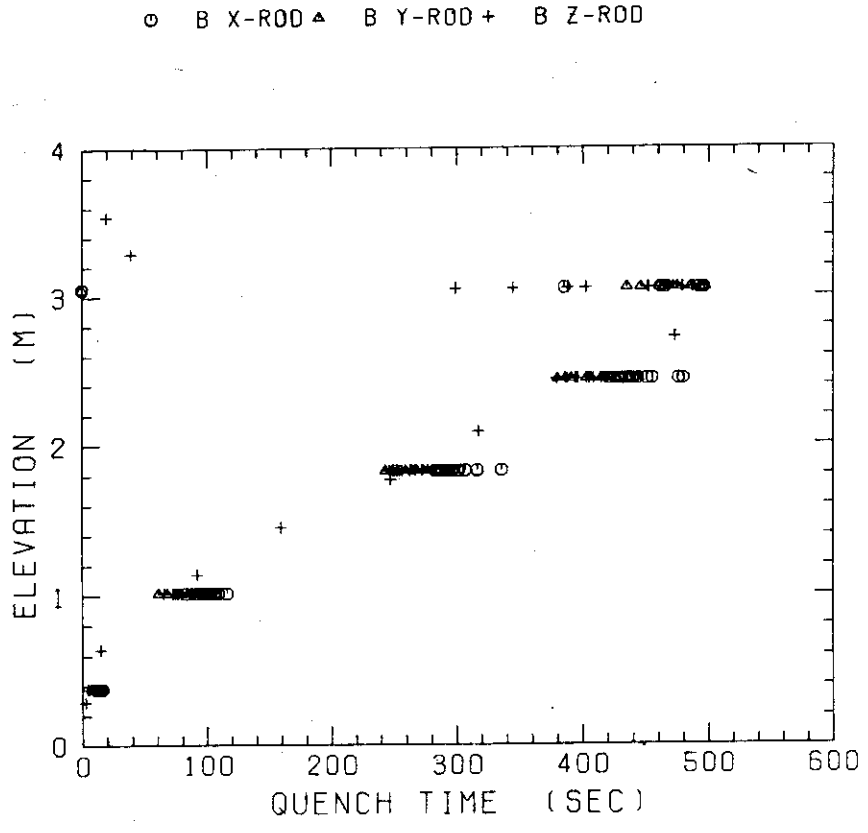

Fig. B-16 Quench temperature in medium power region (B region)

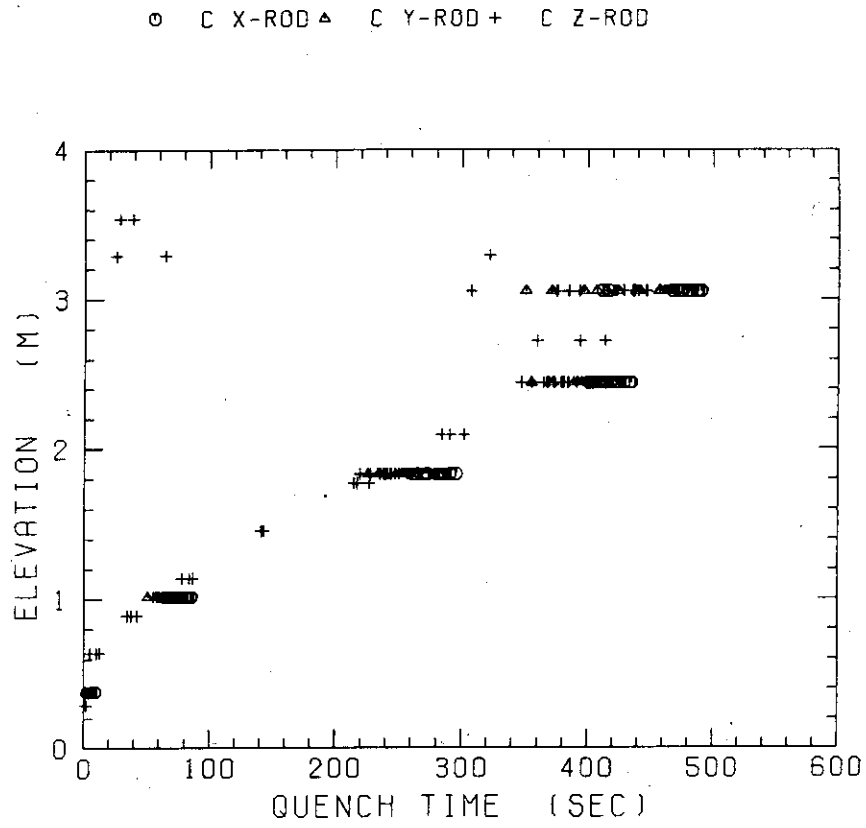

Fig. B-17 Quench temperature in low power region (C region)

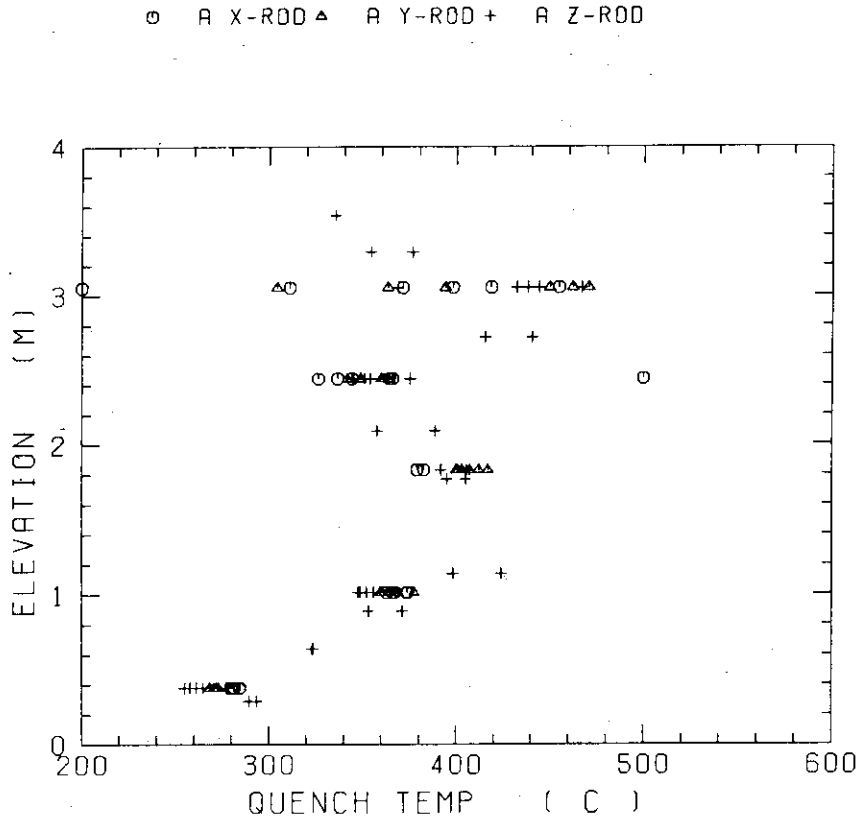

Fig. B-18 Quench time in high power region (A region)

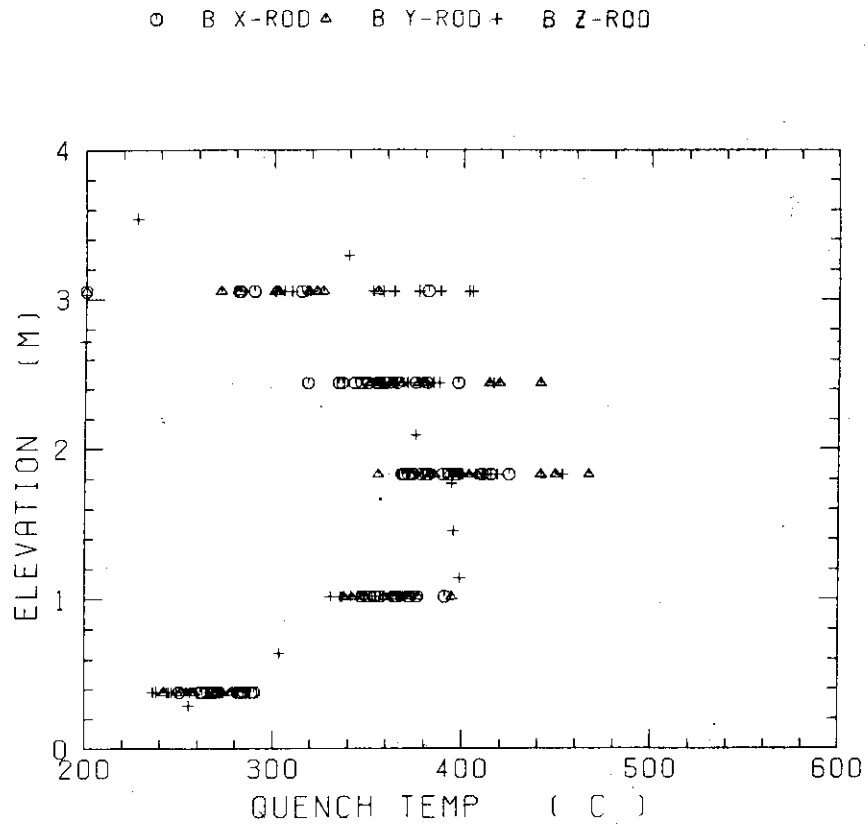

Fig. B-19 Quench time in medium power region (B region)

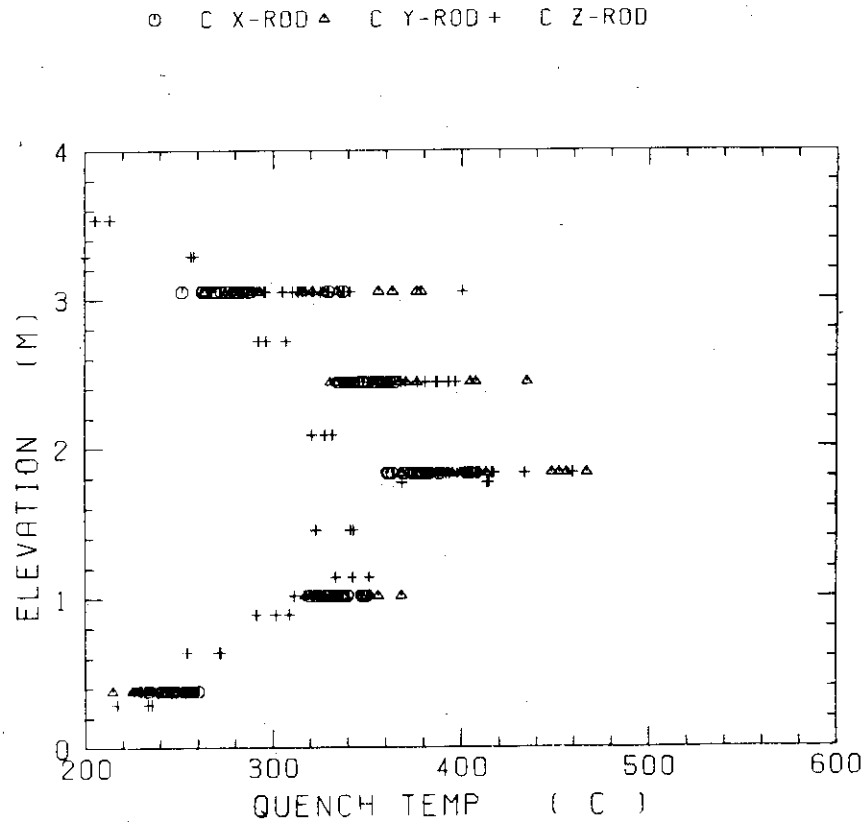

Fig. B-20 Quench time in low power region (C region)

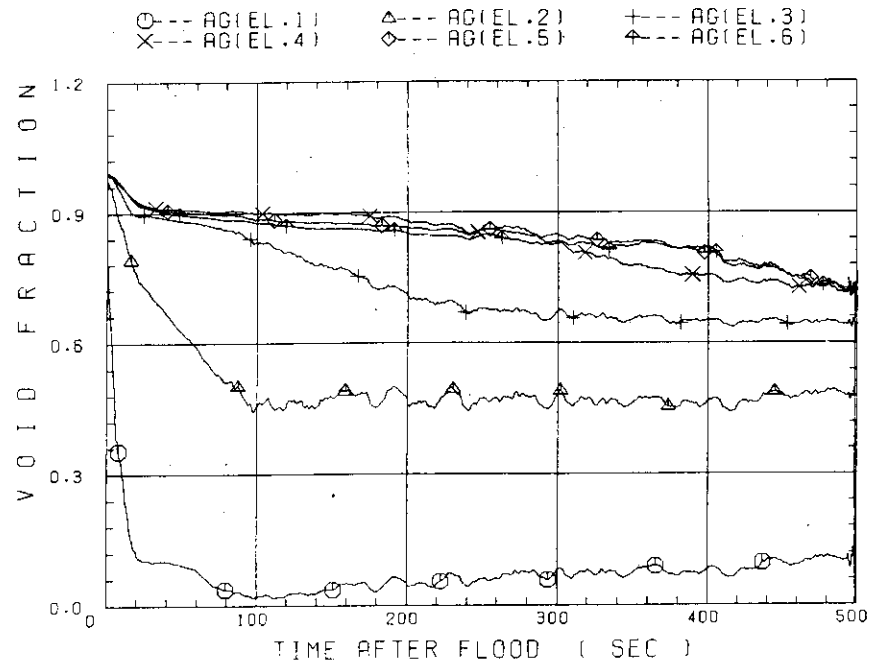

Fig. B-21 Void fraction in core

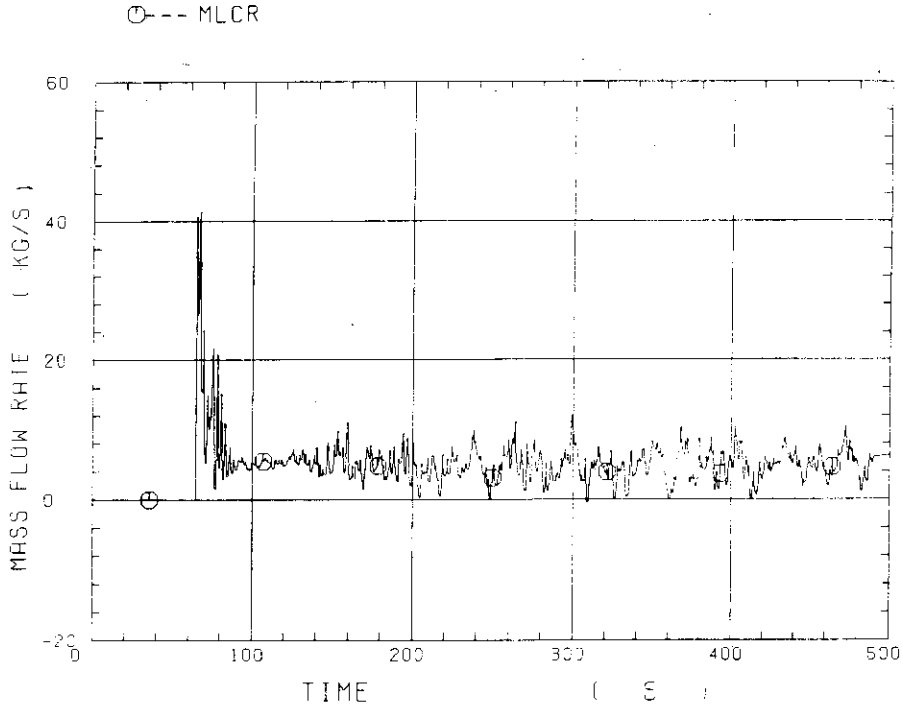

Fig. B-22 Core inlet mass flow rate

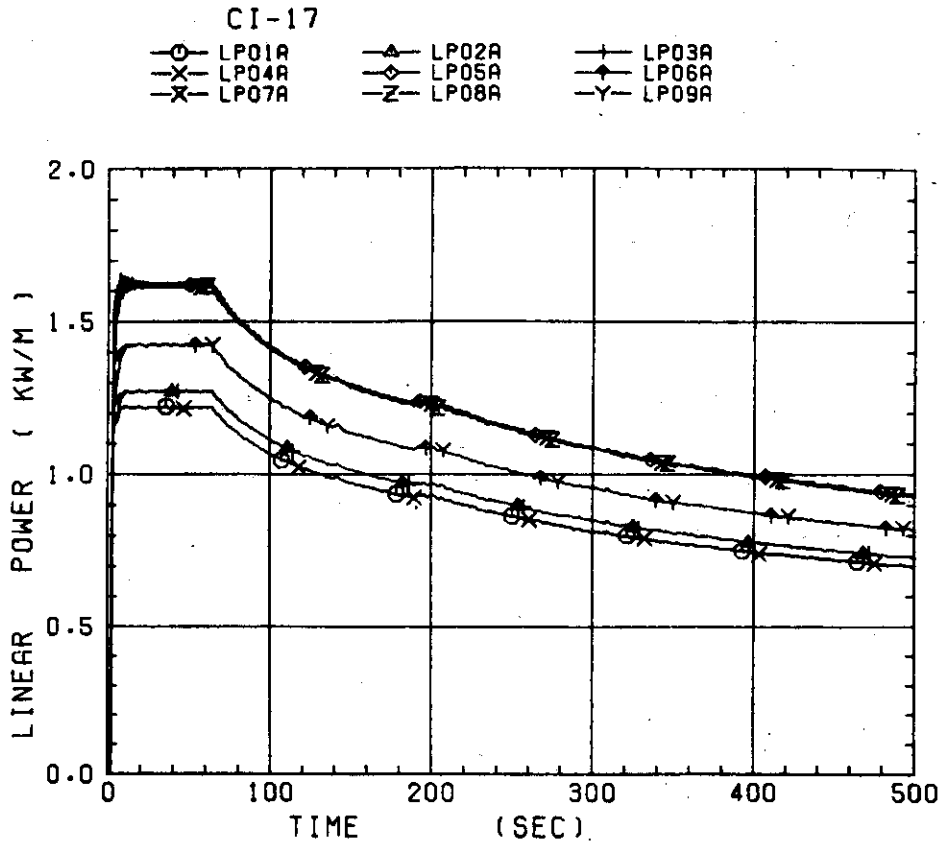

Fig. B-23 Average linear power of heater rod in each power unit zone

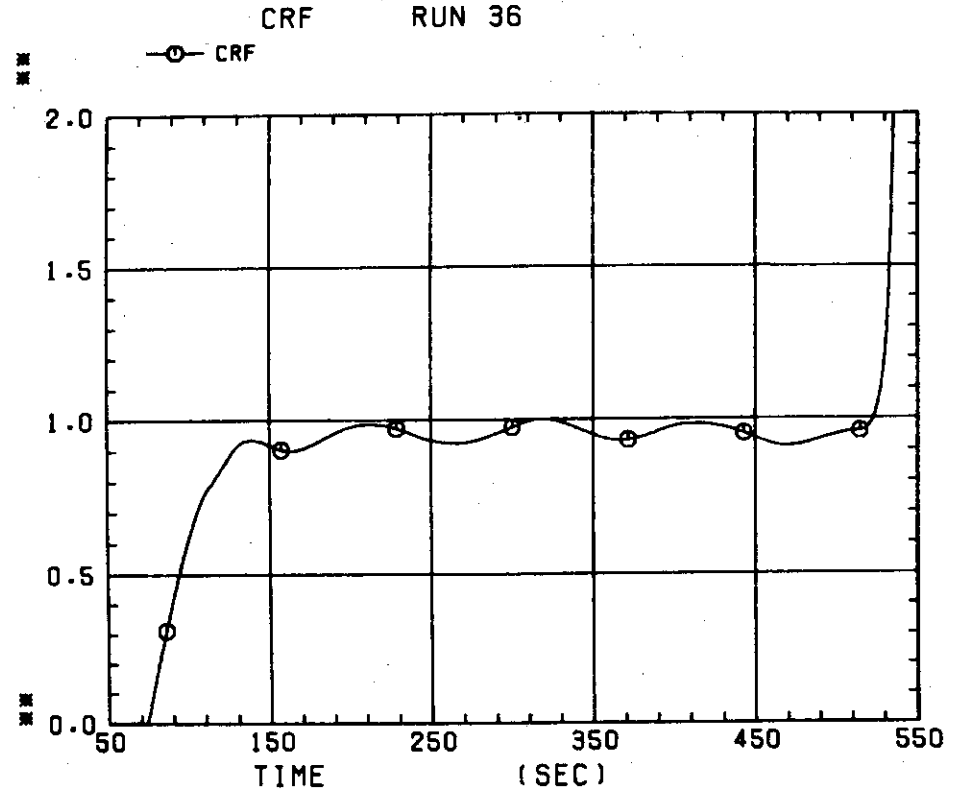

Fig. B-24 Carry-over rate fraction

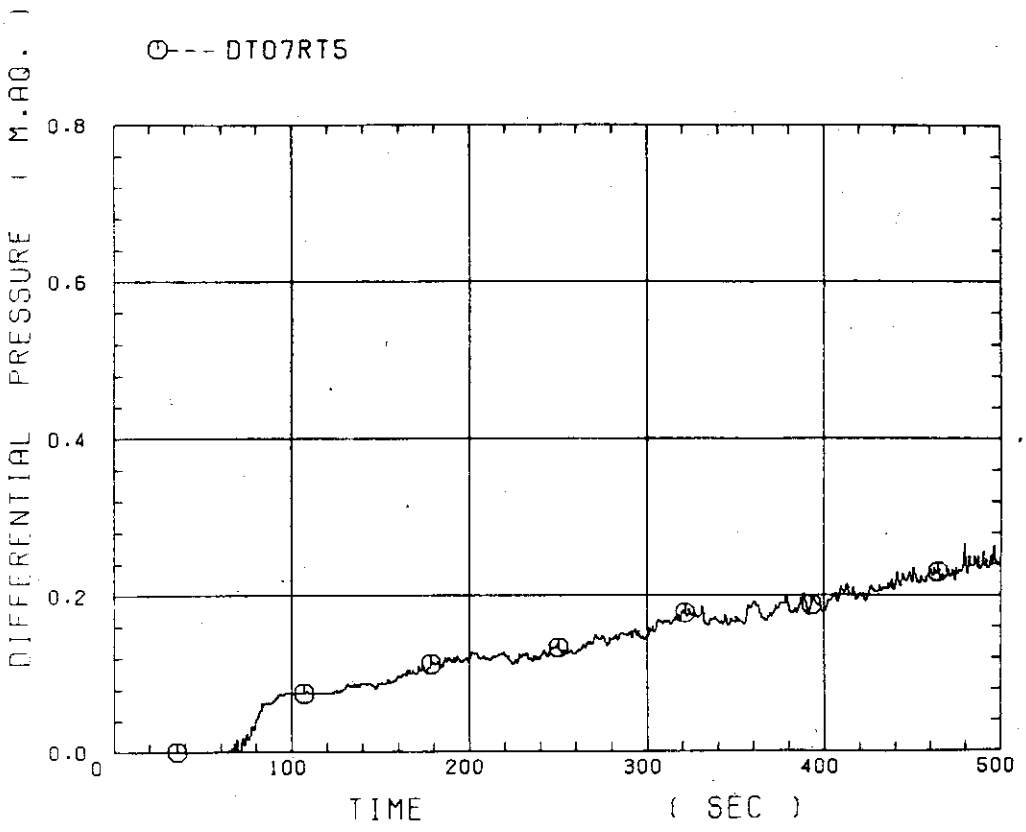

Fig. B-25 Differential pressure through upper plenum

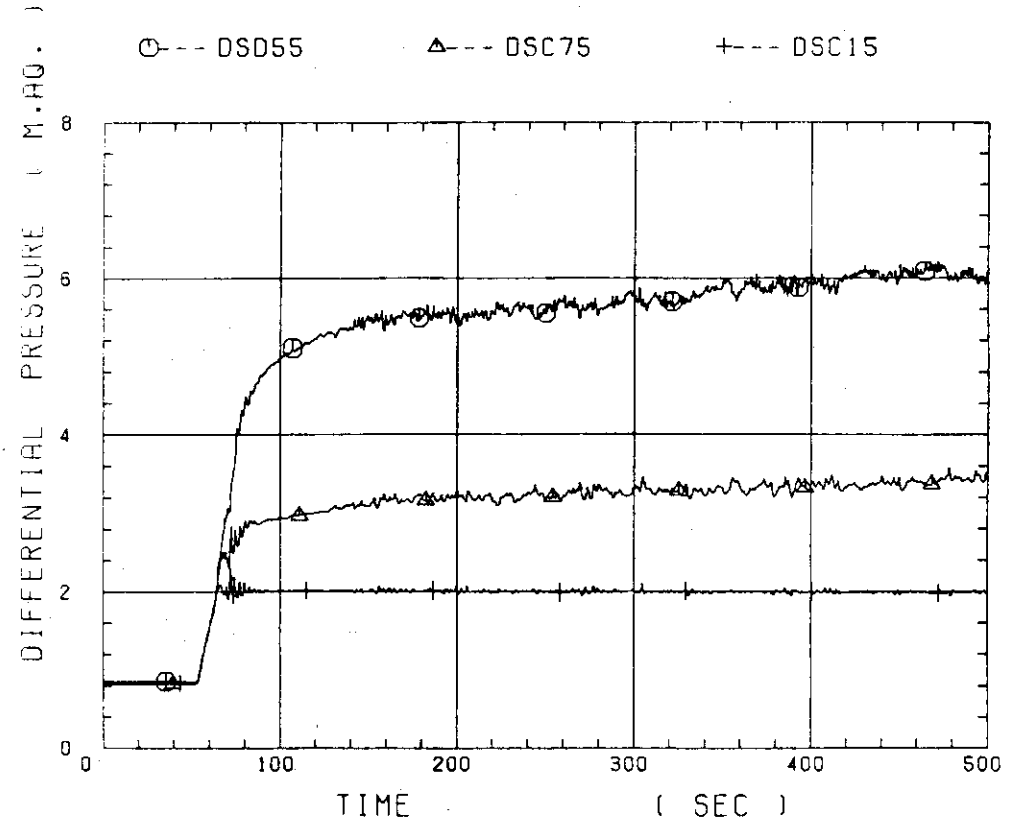

Fig. B-26 Differential pressure through downcomer, core, and lower plenum

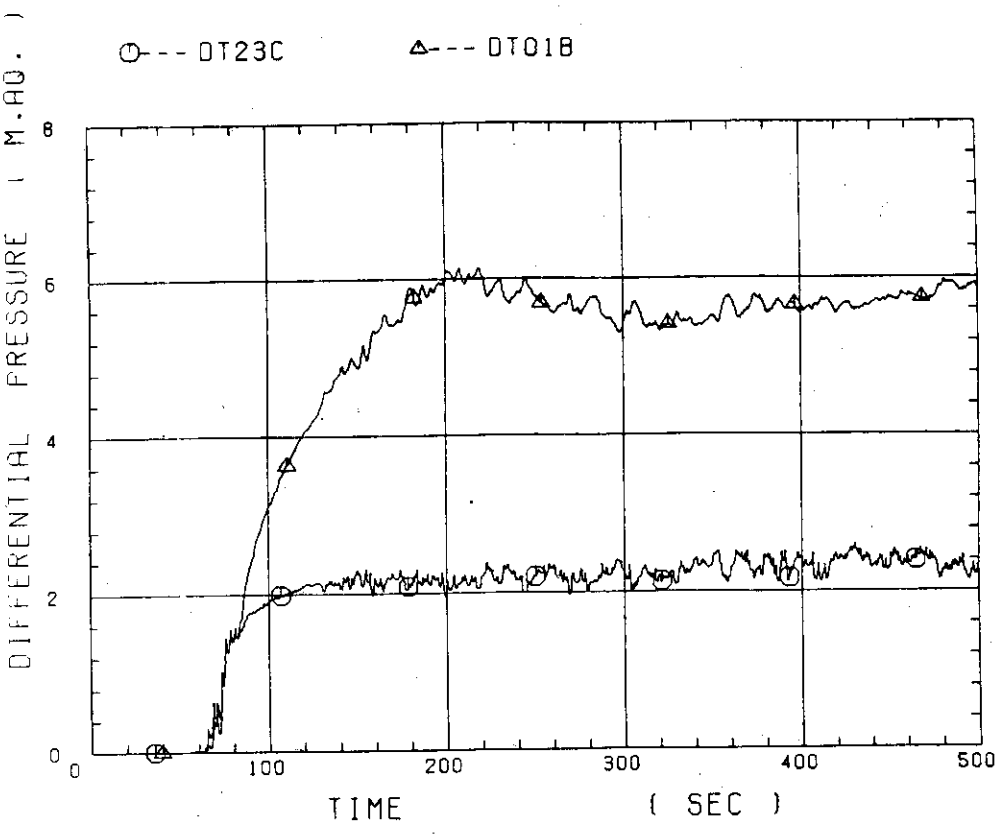

Fig. B-27 Differential pressure through intact and broken loops

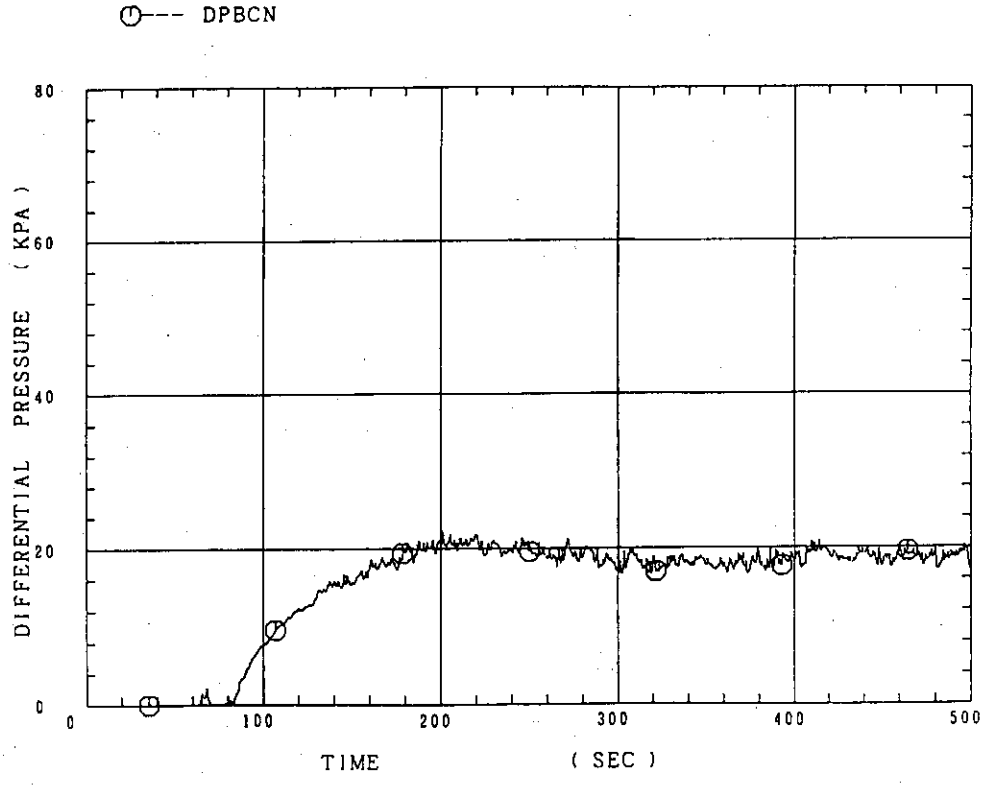

Fig. B-28 Differential pressure through broken cold leg nozzle

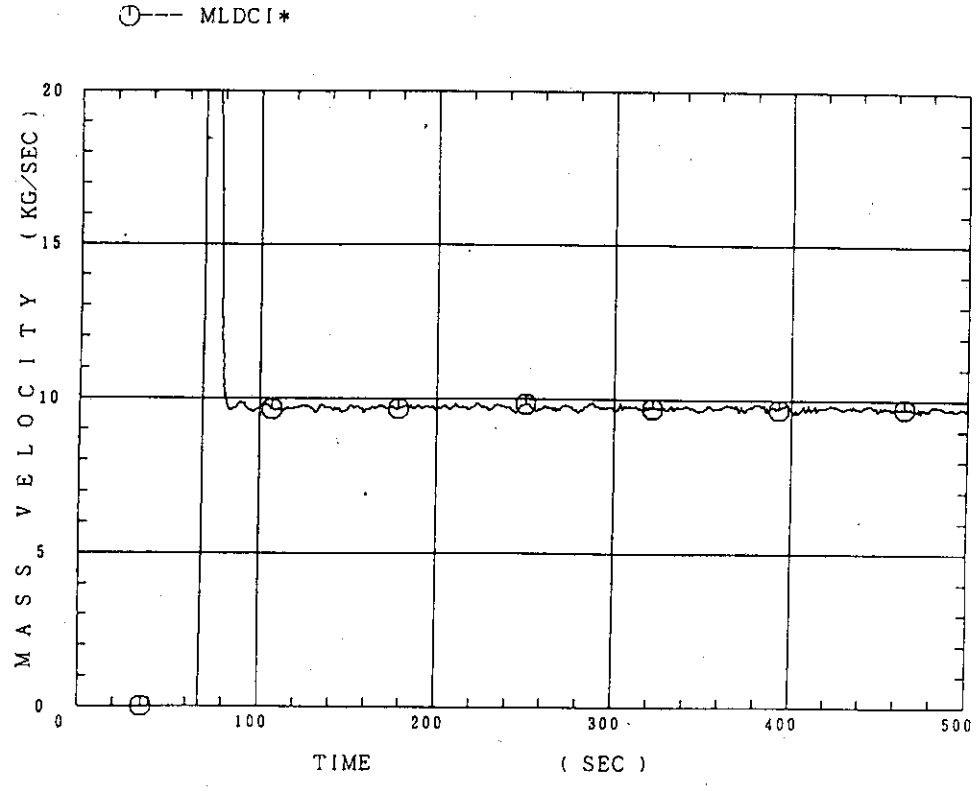

Fig. B-29 Total water mass flow rate from intact loops to downcomer

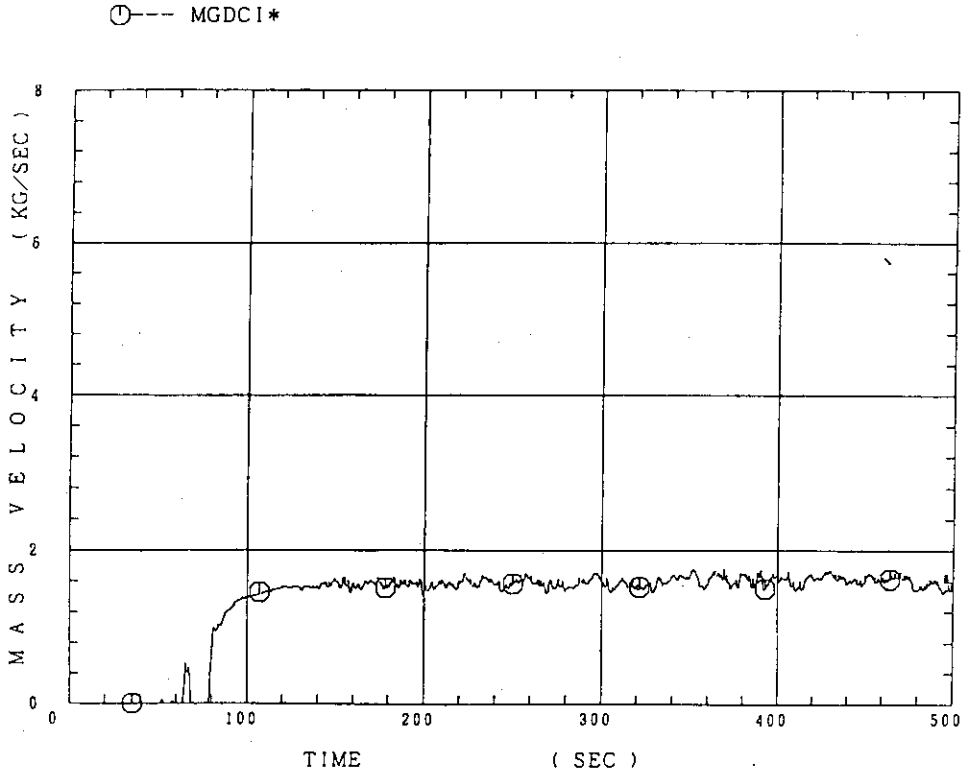

Fig. B-30 Total steam mass flow rate from intact loops to downcomer

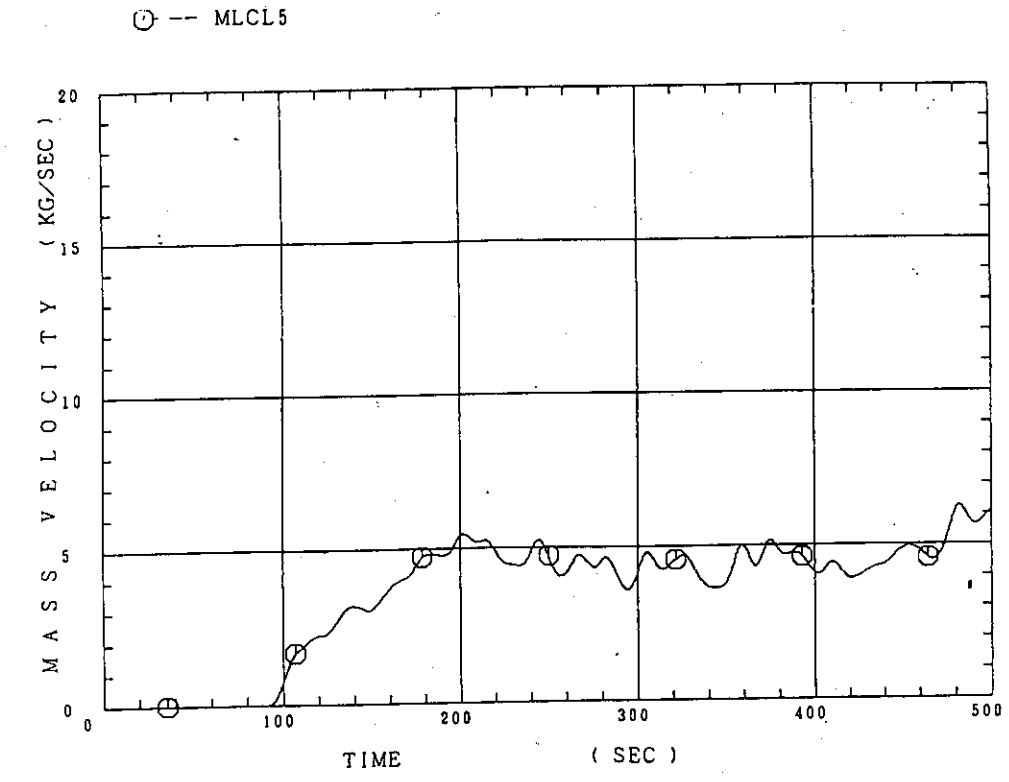

Fig. B-31 Water mass flow rate through broken cold leg nozzle

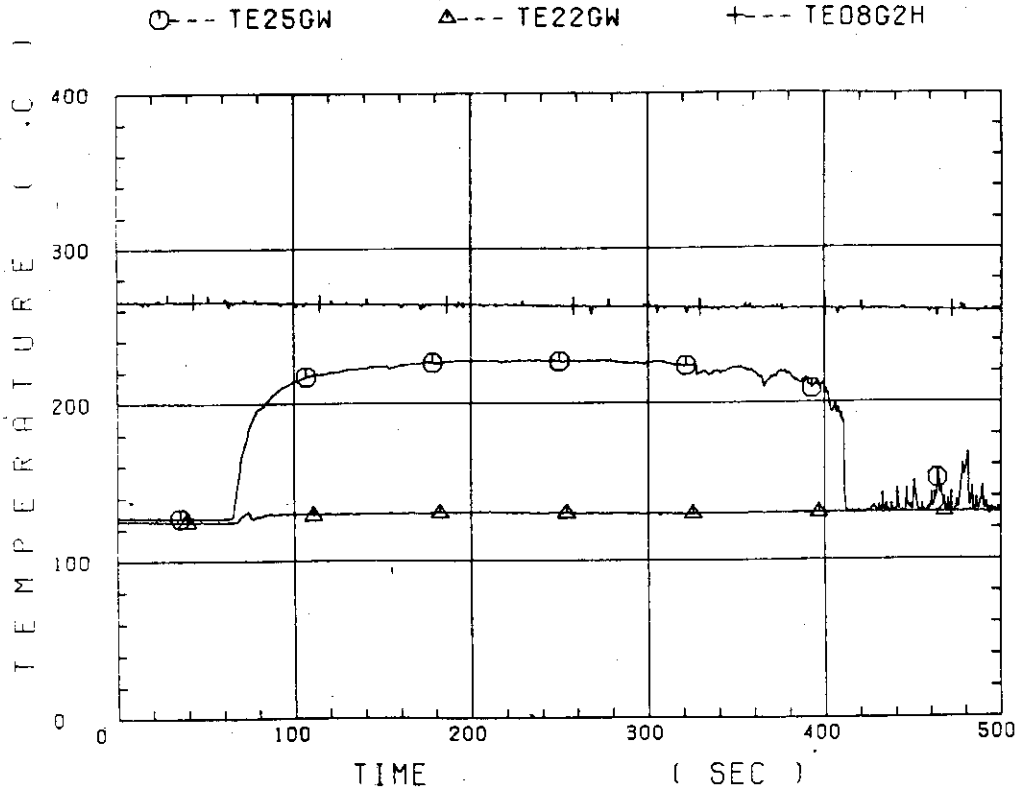

Fig. B-32 Fluid temperature in inlet plenum, outlet plenum, and secondary of steam generator 1

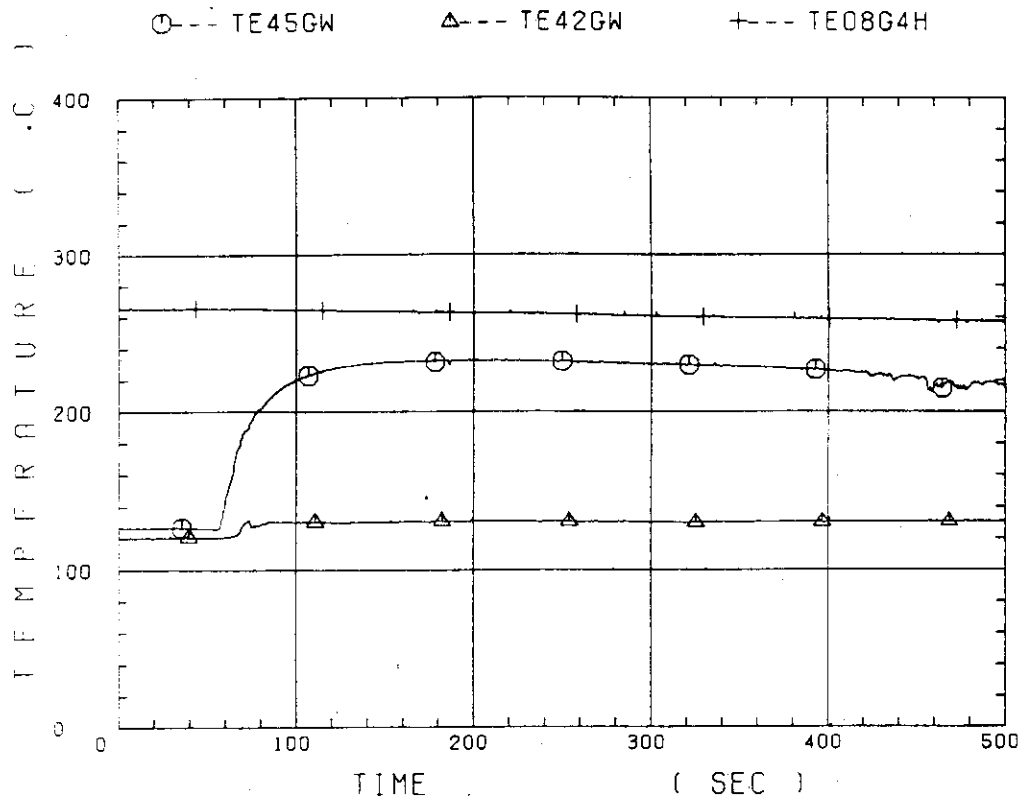

Fig. B-33 Fluid temperature in inlet plenum, outlet plenum, and secondary of steam generator 2

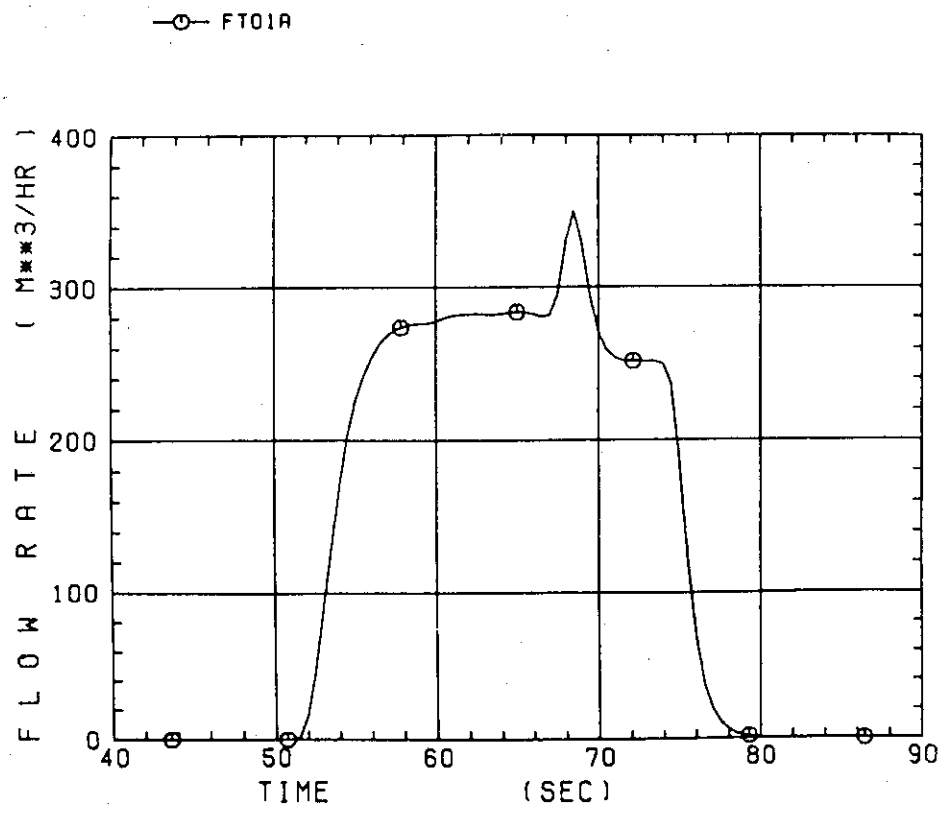

Fig. B-34 Total accumulator injection rate

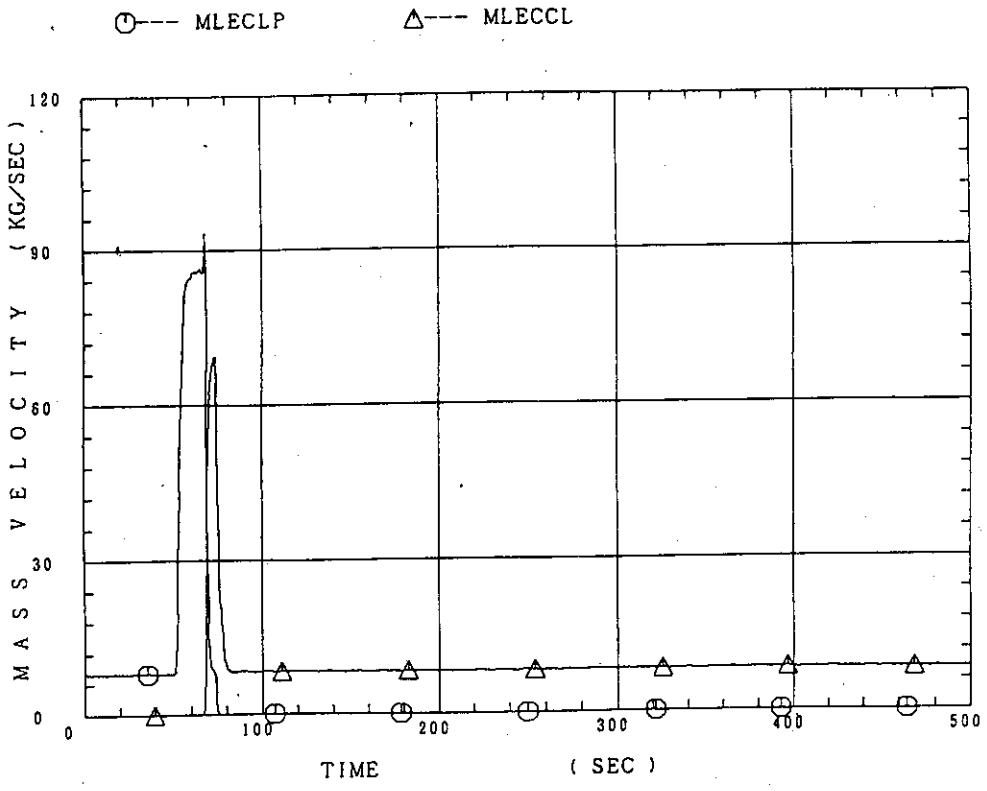

Fig. B-35 ECC water injection rates to lower plenum and to cold legs

Appendix C

Main results of test C1-20 (Run 39)

Table and Figure List

Table C-1 Summary of test conditions

1. TEST TYPE : ASSYMMETRIC CORE TEMPERATURE DISTRIBUTION TEST

2. TEST NUMBER : RUN 039 3. DATE : March 26, 1981

4. POWER : A: TOTAL: 9.39 MW; B:LINEAR: 1.41 KW/M

5. RELATIVE RADIAL POWER SHAPE :

A: ZONE: A B C

B: RATIO: 1.155 1.079 0.885

6. AXIAL POWER SHAPE : CHOPPED COSINE

7. PRESSURE (KG/CM^2A) :

A: SYSTEM: 2.04, B: CONTAINMENT 2.06,

C: STEAM GENERATOR SECONDARY: 53.3

8. TEMPERATURE (DEG.C) :

A: DOWNCOMER WALL 169, B: VESSEL INTERNALS 128,

C: PRIMARY PIPING WALL 121, D: LOWER PELNUM LIQUID 120,

E: ECC LIQUID 38.3, F: STEAM GENERATOR SECONDARY 265,

G: CORE TEMPERATURE AT ECC INITIATION MAX.788 MIN.227

9. ECC INJECTION TYPE: C

A: COLD LEG, B: LOWER PLENUM, C: LOWER PLENUM + COLD LEG

10. PUMP K-FACTOR : $\sim$ 15

11. ECC FLOW RATES AND DURATION :

A: ACCUMULATOR 281 M^3/HR FROM 0 TO 23.5 SECONDS

B: LPCI 30.1 M^3/HR FROM 23.5 TO 750 SECONDS

C: ECC INJECTION TO LOWER PLENUM : FROM 0 TO 17 SECONDS

(VALVE OPENING AND CLOSING TIMES ARE INCLUDED IN THE INJECTION DURATION)

12. INITIAL WATER LEVEL IN LOWER PLENUM : 0.90 M.

13. POWER CONTROL : ANS x 1.2 + ACTINIDE (30 SEC AFTER SCRAM)

14. EXPECTED BOCREC TIME FROM ECC INITIATION 12 SEC

15. EXPECTED PEAK TEMPERATURE AT BOCREC 886 C

Table C-2 Chronology of events

EVENT	TIME (sec)
Test Initiated (Heater Rods Power on) (Data Recording Initiated)	0
Accumulator Injection Initiated	20
Power Decay Initiated (Bottom of Core Recovery)	31.5 (31.0)
Accumulator Injection Switched from Lower Plenum to Cold Leg	37
Accumulator Injection Ended and LPCI Injection Initiated	43.5
All Heater Rods Quenched	608.5
Power Off	680
LPCI Injection Ended	770
Test Ended (Data Recording Ended)	972

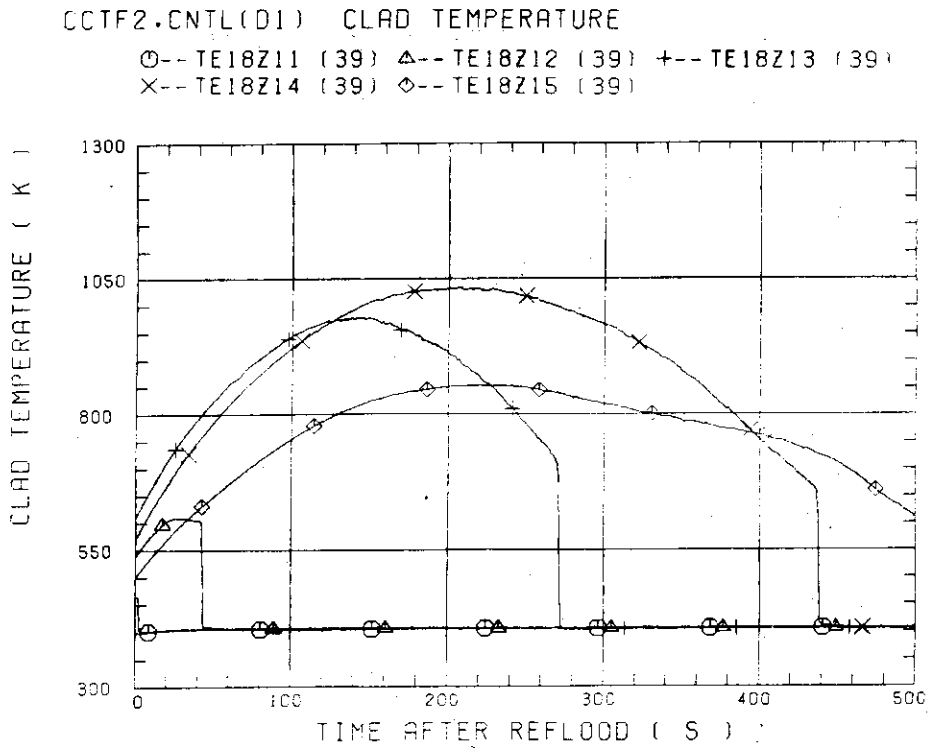

Fig. C-1 Surface temperature on low power rod (Z-rod) in medium power region (B region) (average power rod)

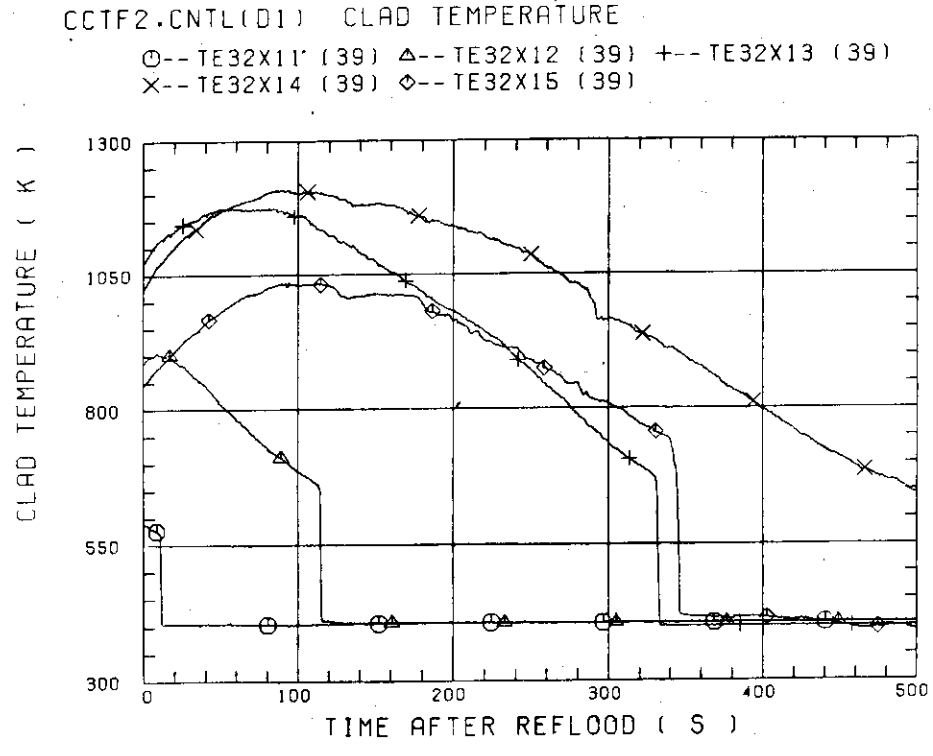

Fig. C-2 Surface temperature on high power rod (X-rod) in high power region (A region) (peak power rod)

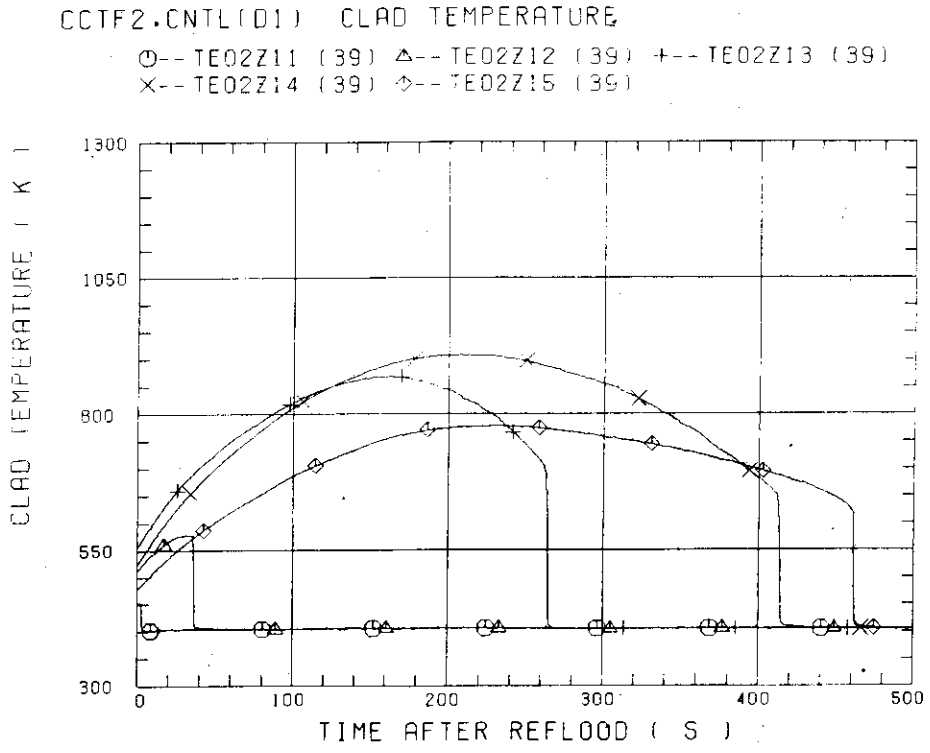

Fig. C-3 Surface temperature on low power rod (Z-rod) in low power region (C region) (lowest power rod)

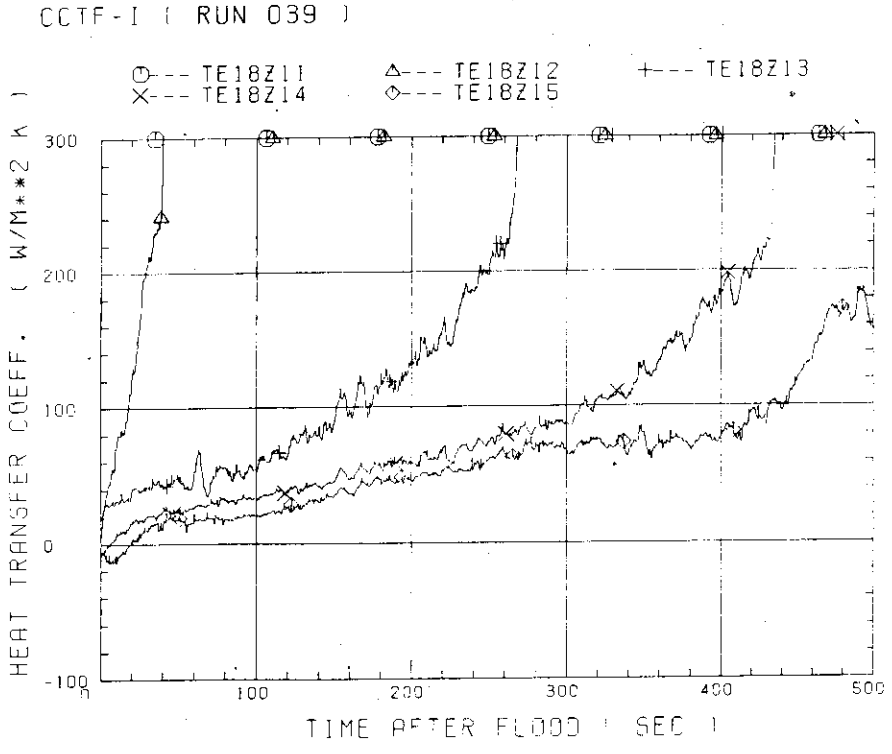

Fig. C-4 Heat transfer coefficient of low power rod (Z-rod) in medium power region (B region) (average power rod)

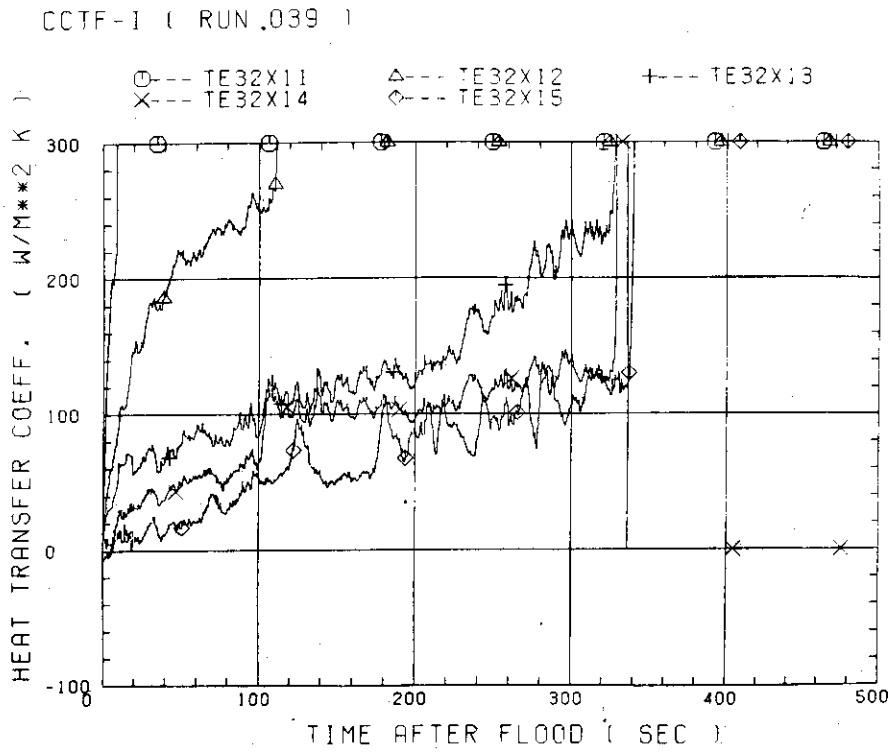

Fig. C-5 Heat transfer coefficient of high power rod (X-rod) in high power region (A region) (peak power rod)

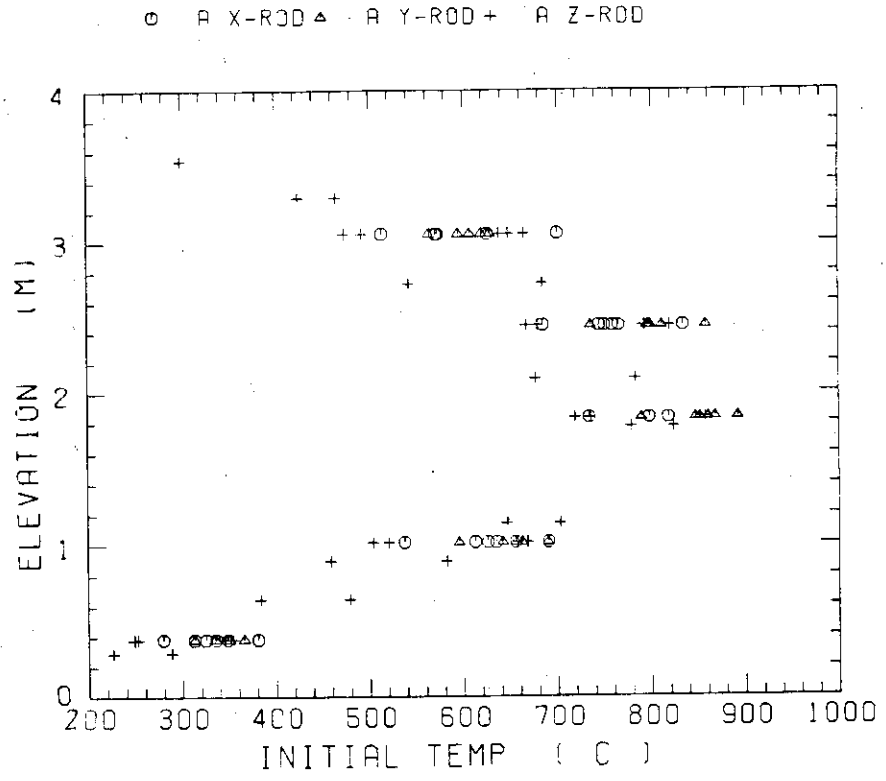

Fig. C-6 Initial rod surface temperature in high power region (A region)

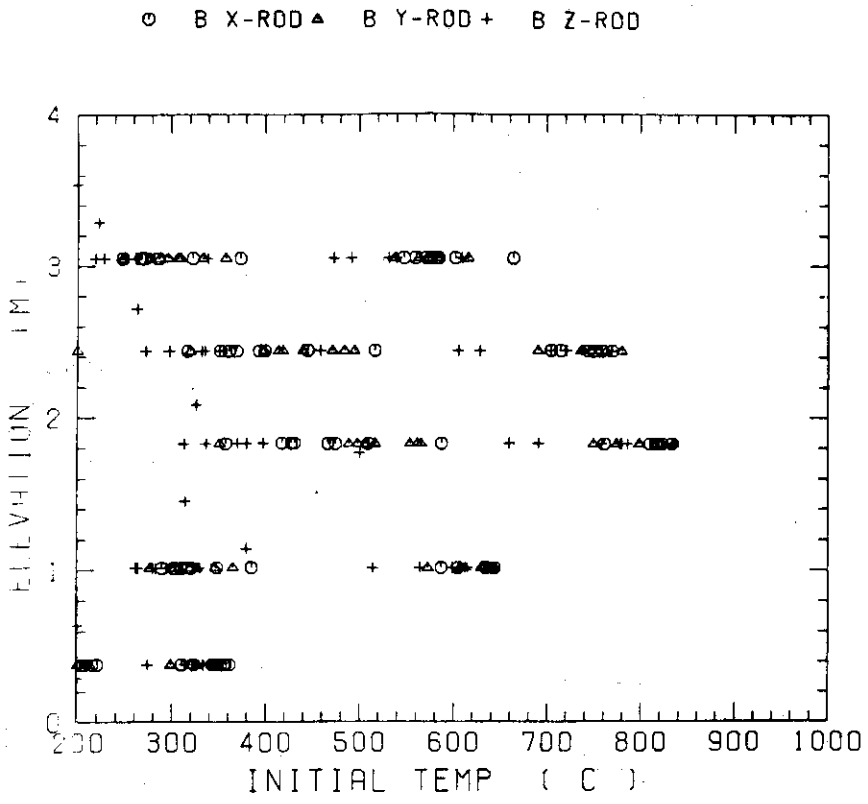

Fig. C-7 Initial rod surface temperature in medium power region (B region)

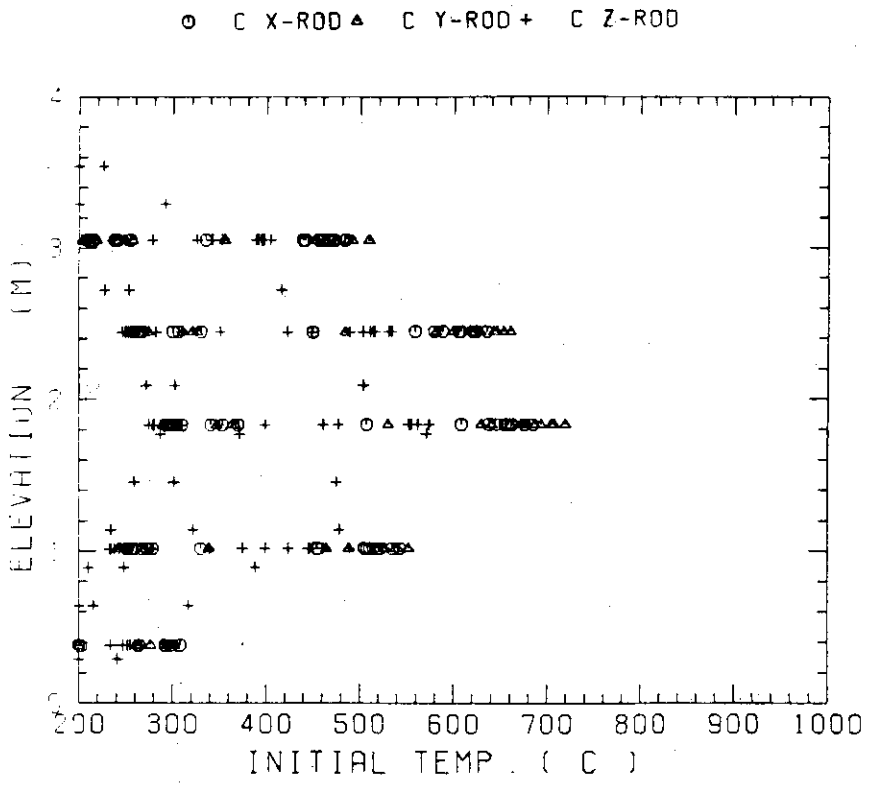

Fig. C-8 Initial rod surface temperature in low power region (C region)

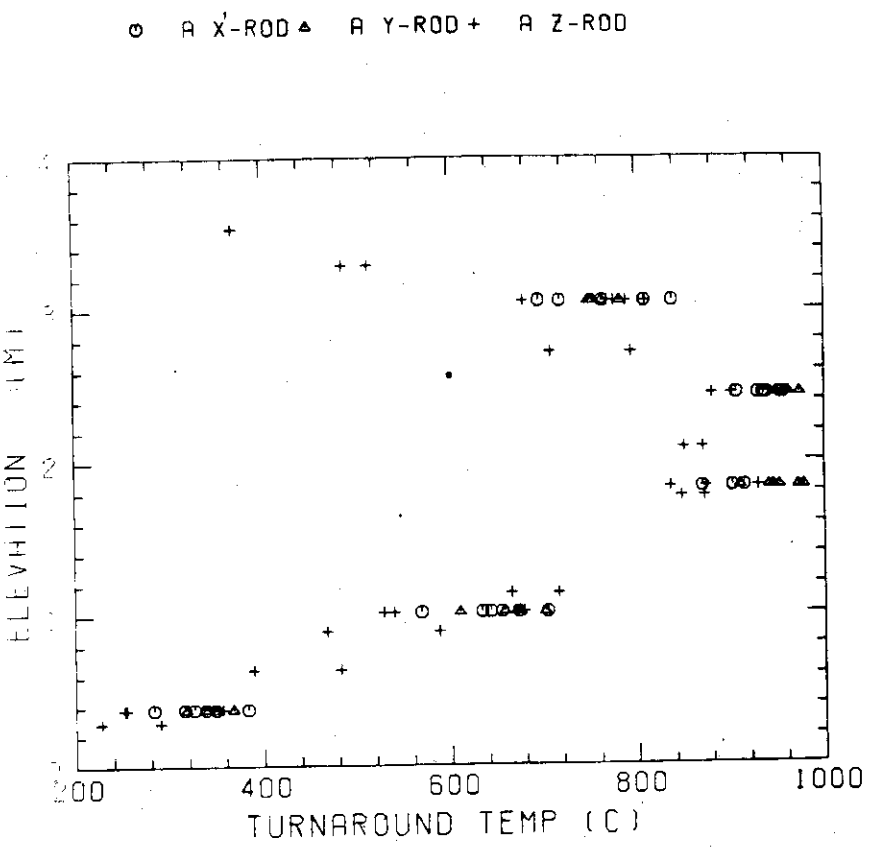

Fig. C-9 Turnaround temperature in high power region (A region)

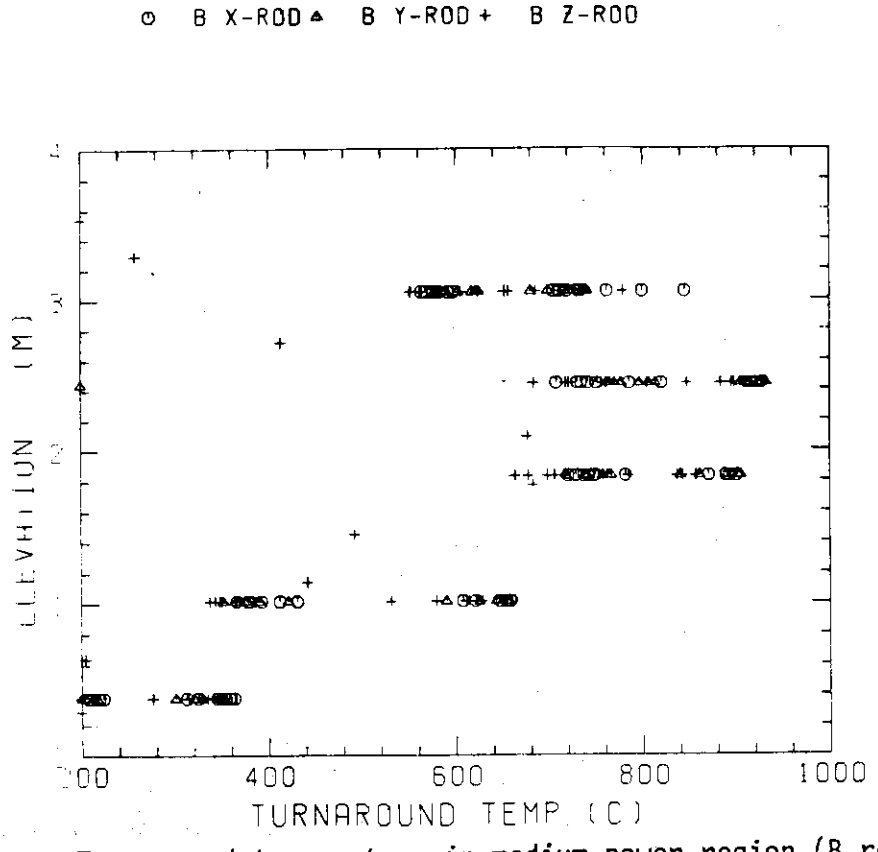

Fig. C-10 Turnaround temperature in medium power region (B region)

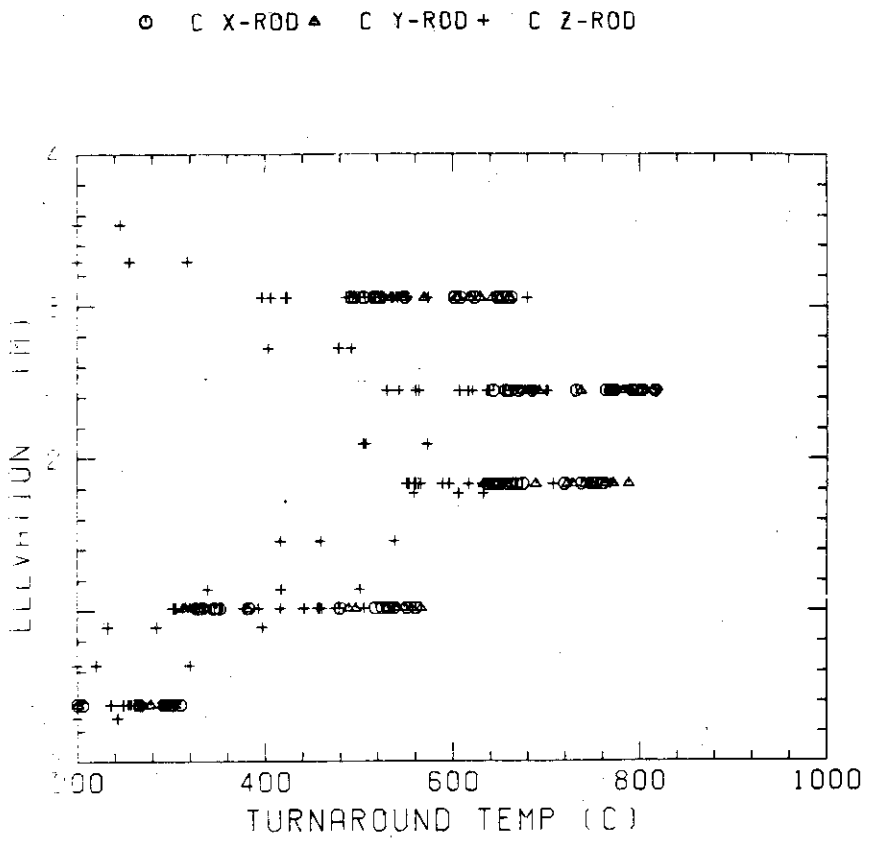

Fig. C-11 Turnaround temperature in low power region (C region)

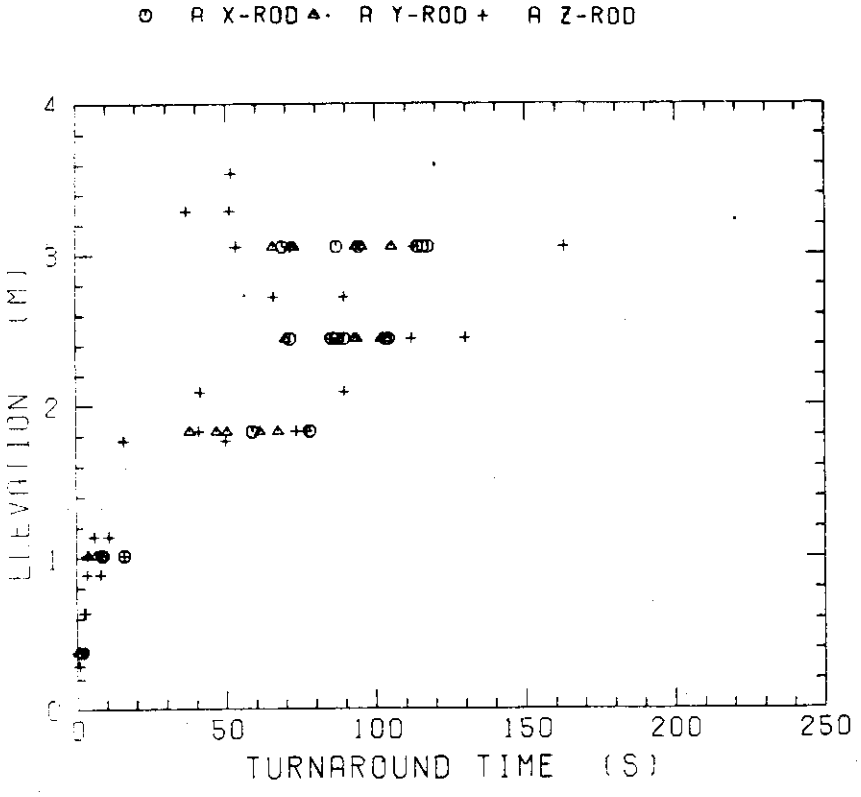

Fig. C-12 Turnaround time in high power region (A region)

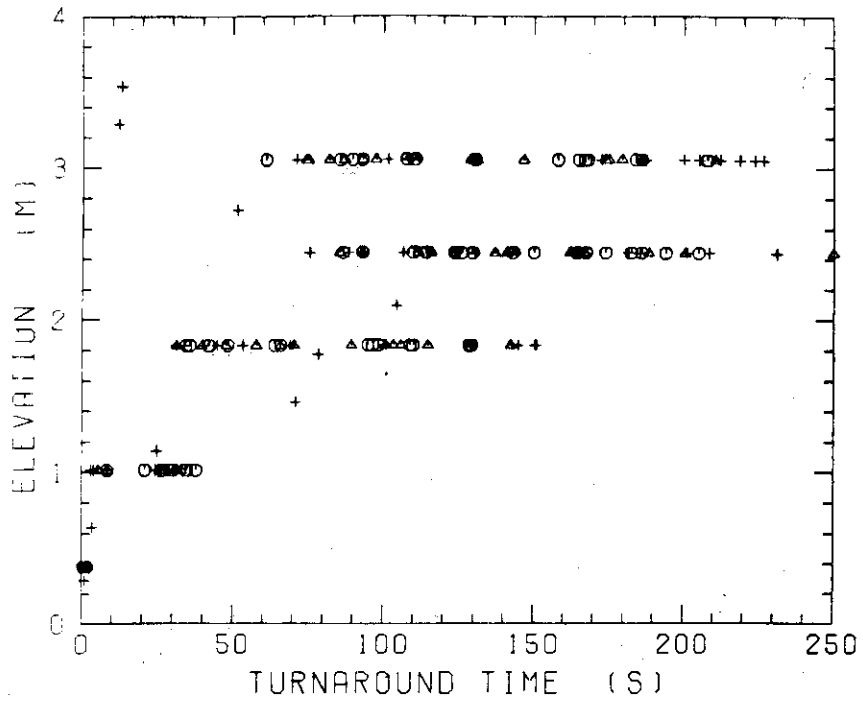

Fig. C-13 Turnaround time in medium power region (B region)

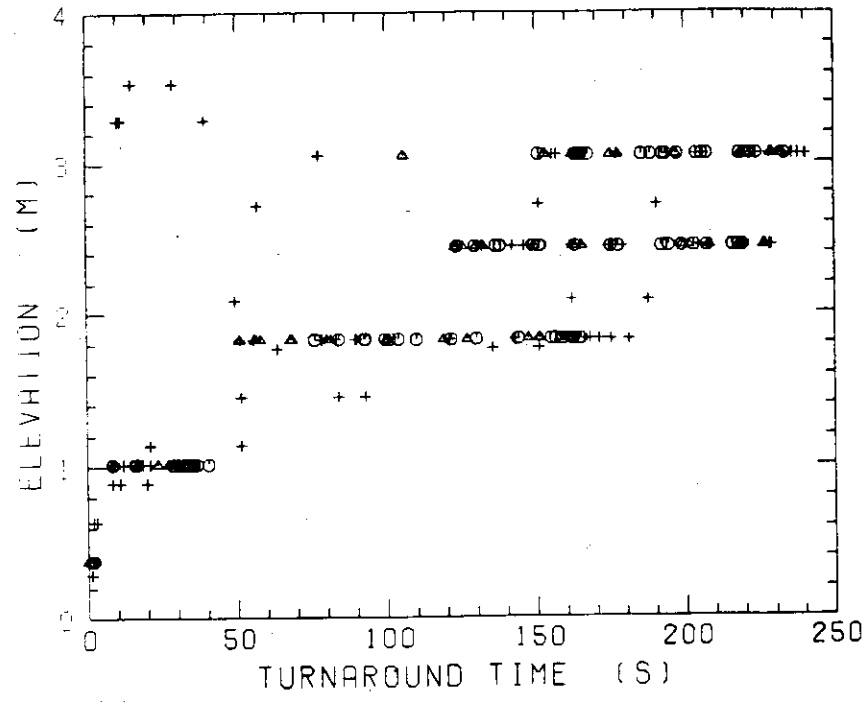

Fig. C-14 Turnaround time in low power region (C region)

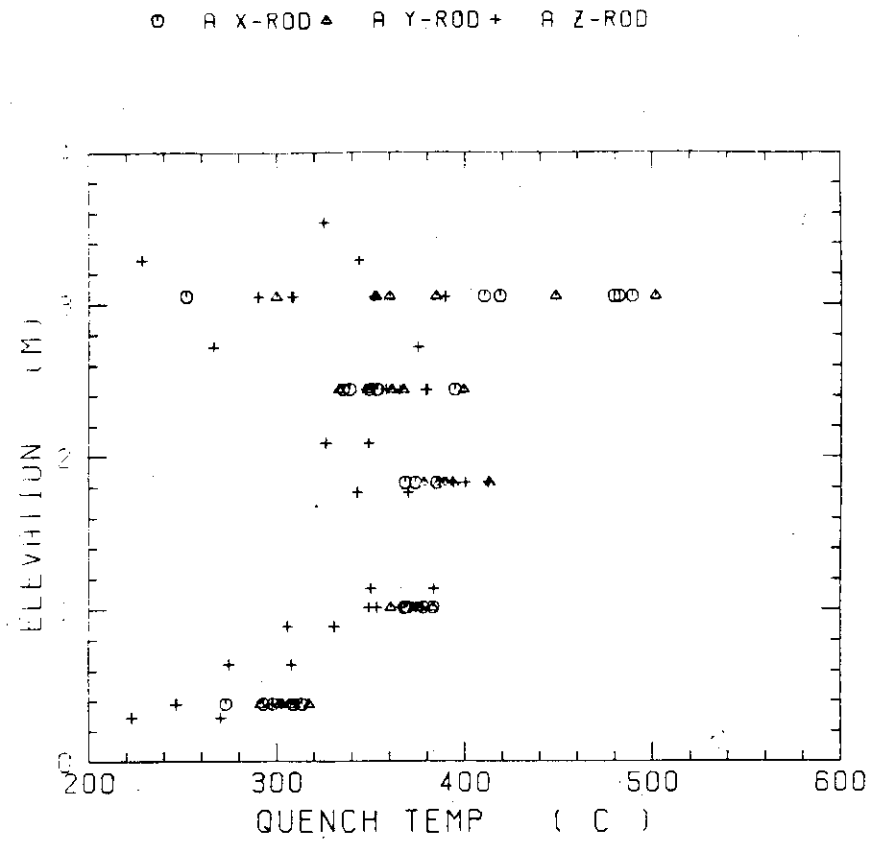

Fig. C-15 Quench temperature in high power region (A region)

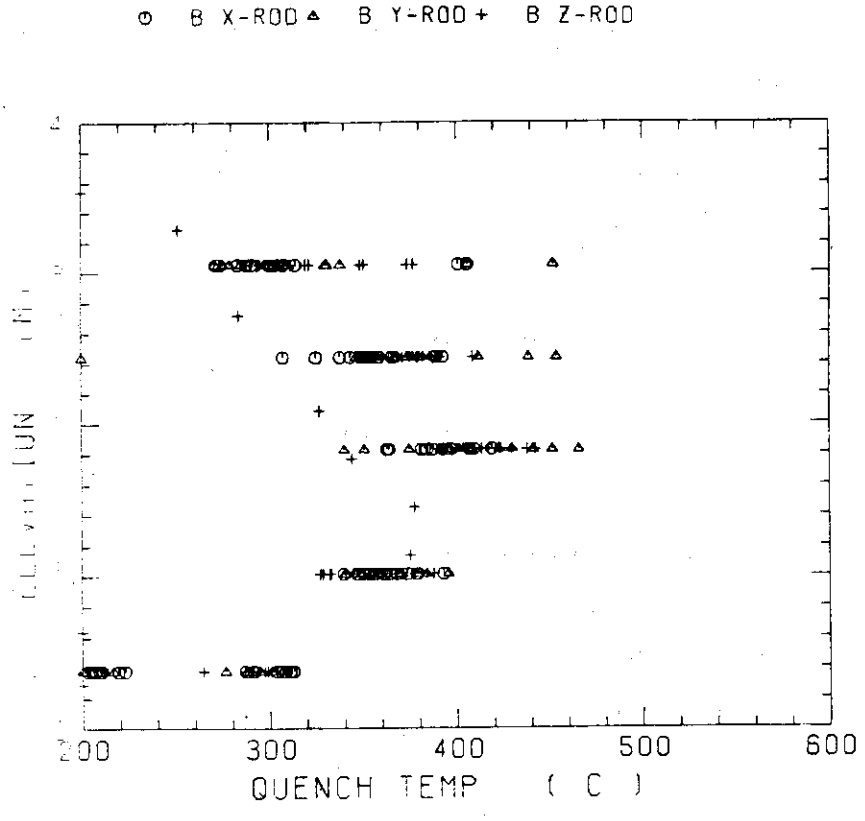

Fig. C-16 Quench temperature in medium power region (B region)

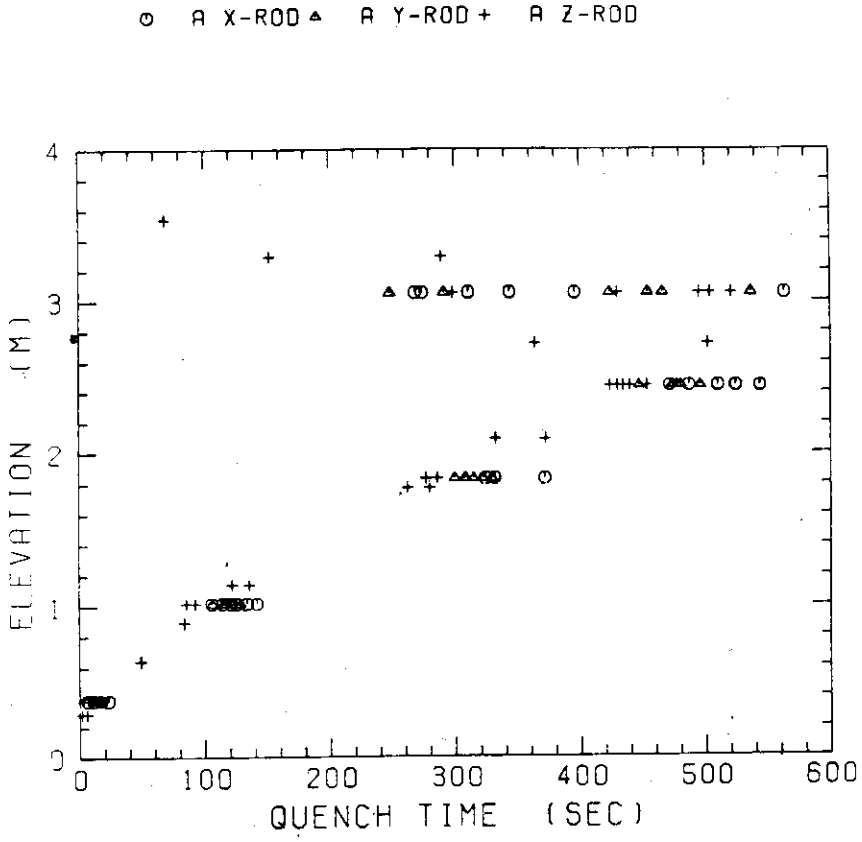

Fig. C-17 Quench temperature in low power region (C region)

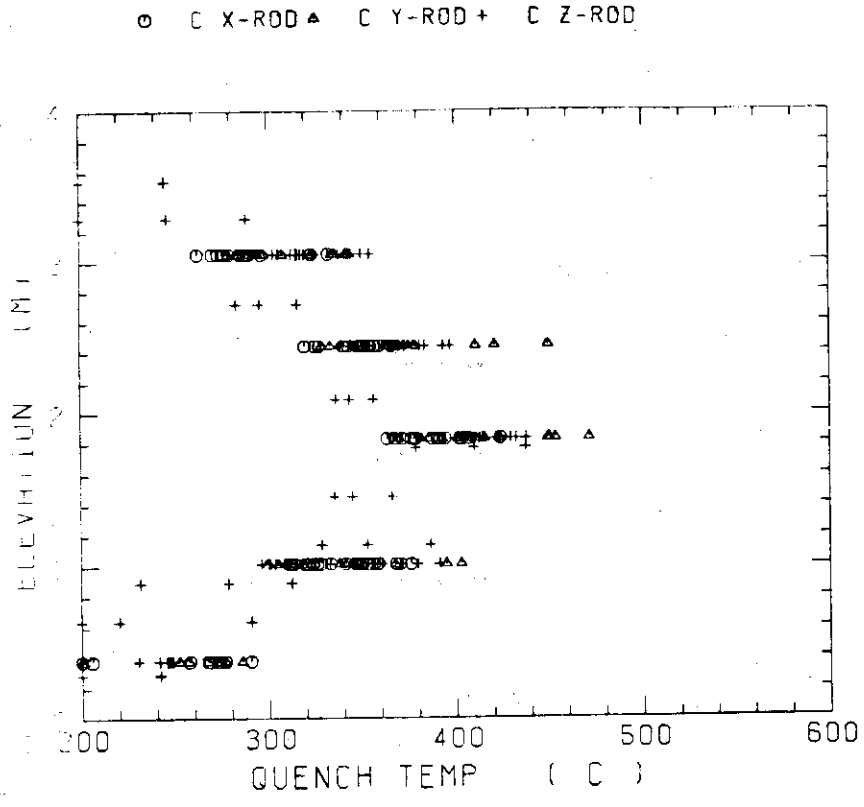

Fig. C-18 Quench time in high power region (A region)

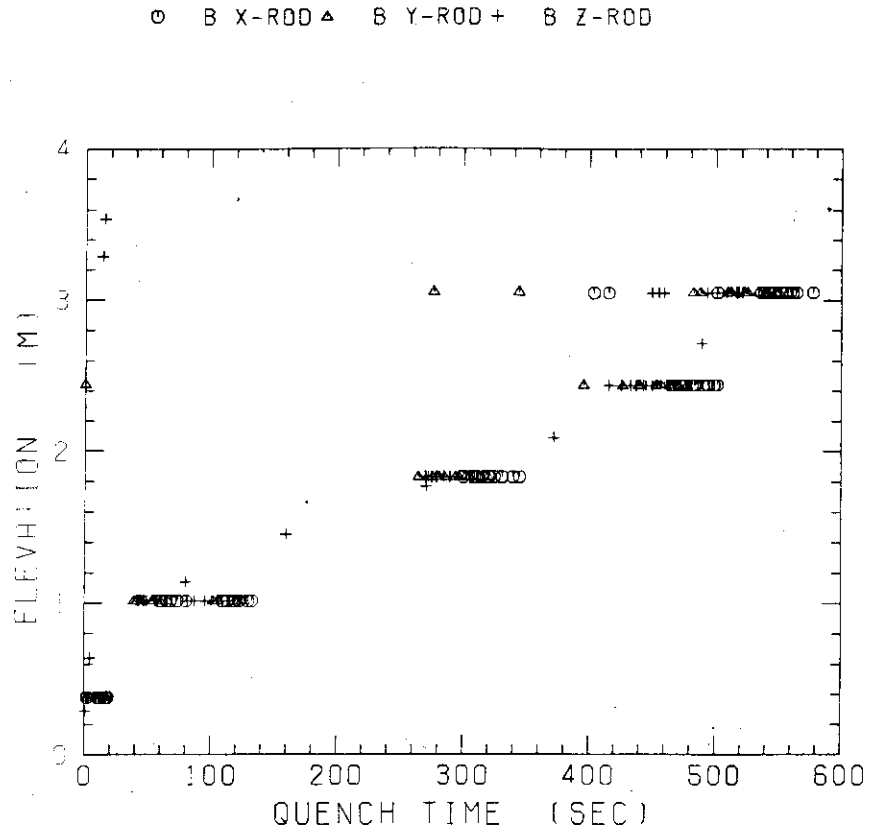

Fig. C-19 Quench time in medium power region (B region)

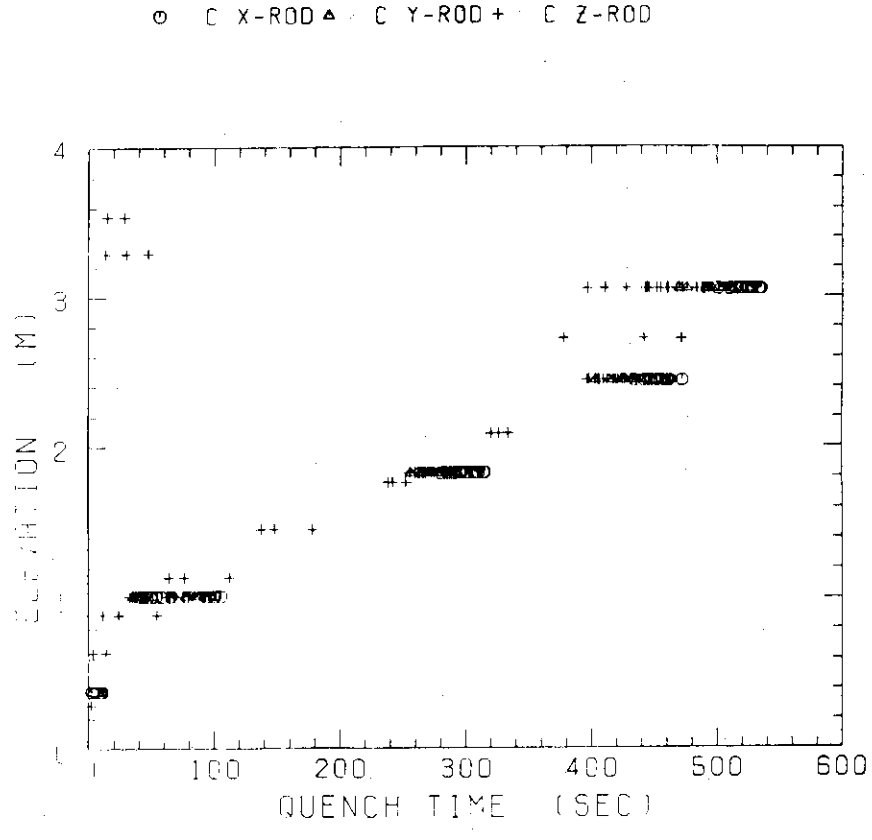

Fig. C-20 Quench time in low power region (C region)

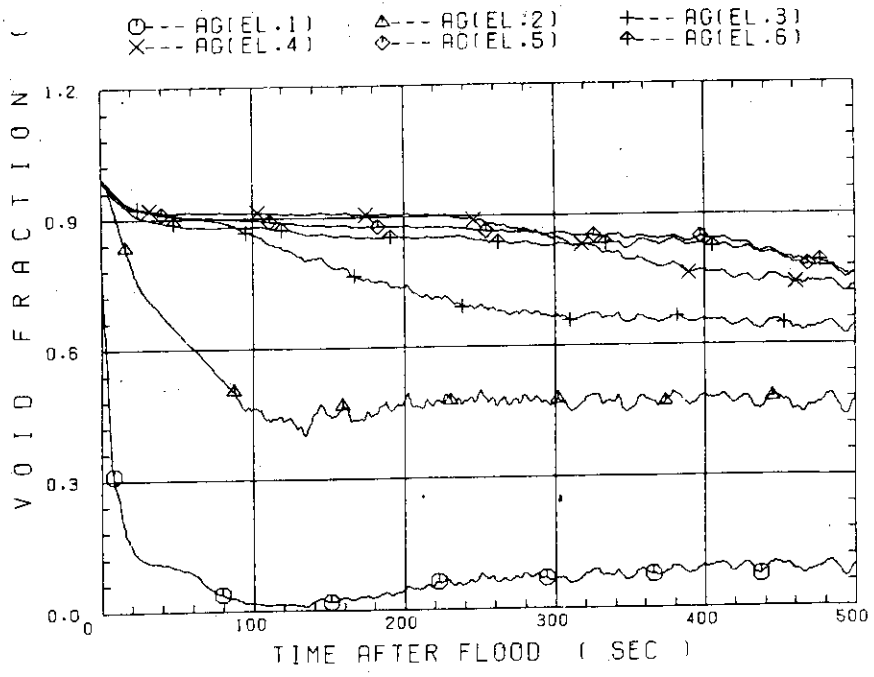

Fig. C-21 Void fraction in core

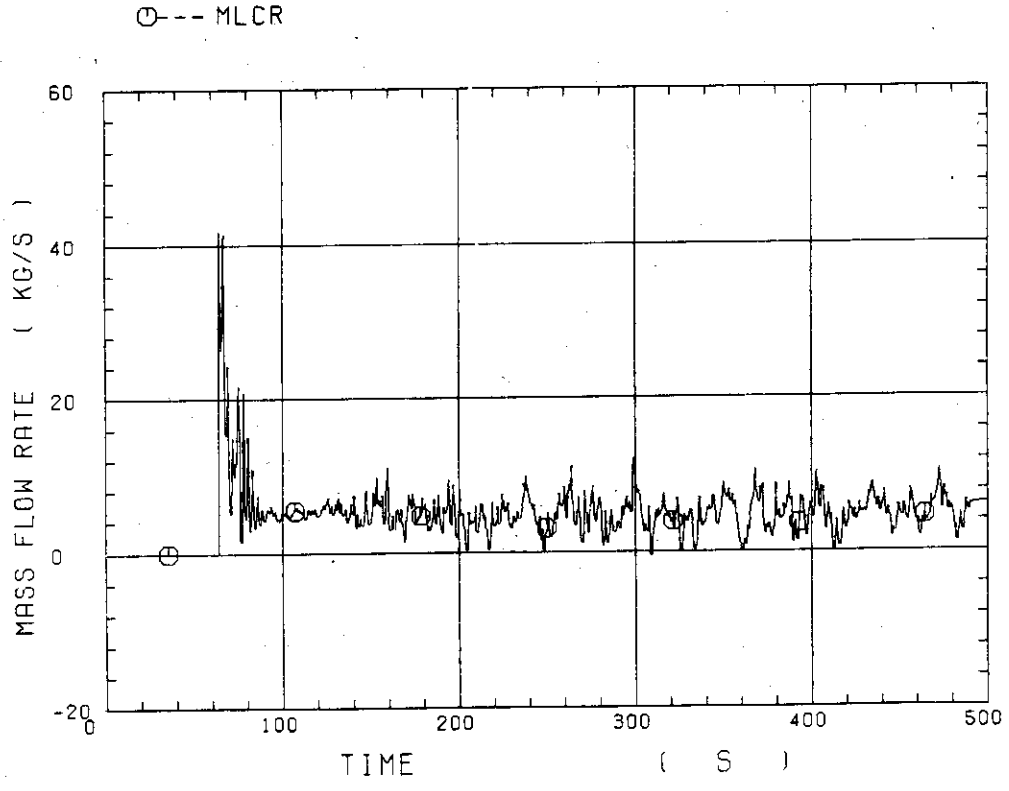

Fig. C-22 Core inlet mass flow rate

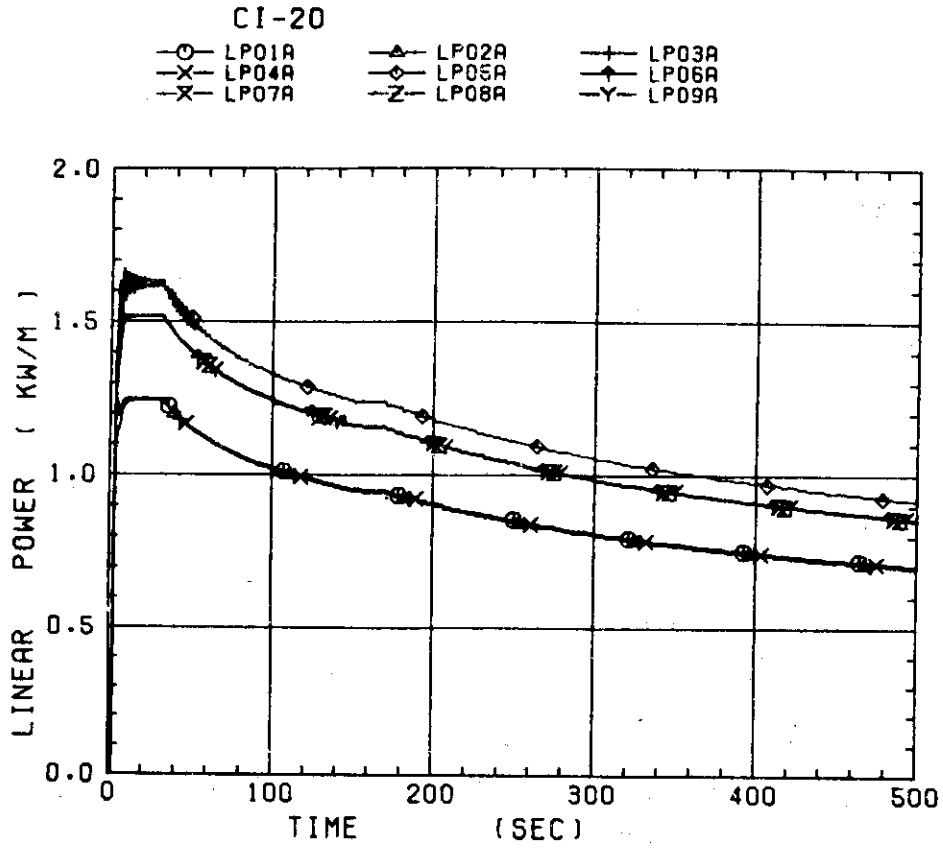

Fig. C-23 Average linear power of heater rod in each power unit zone

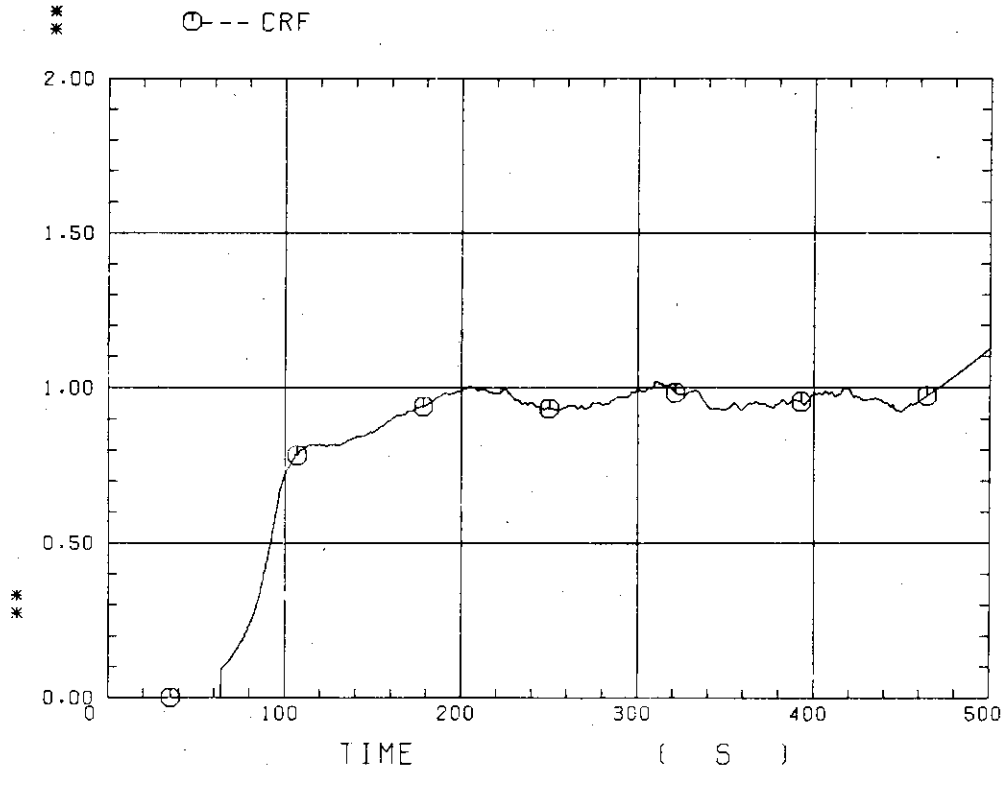

Fig. C-24 Carry-over rate fraction

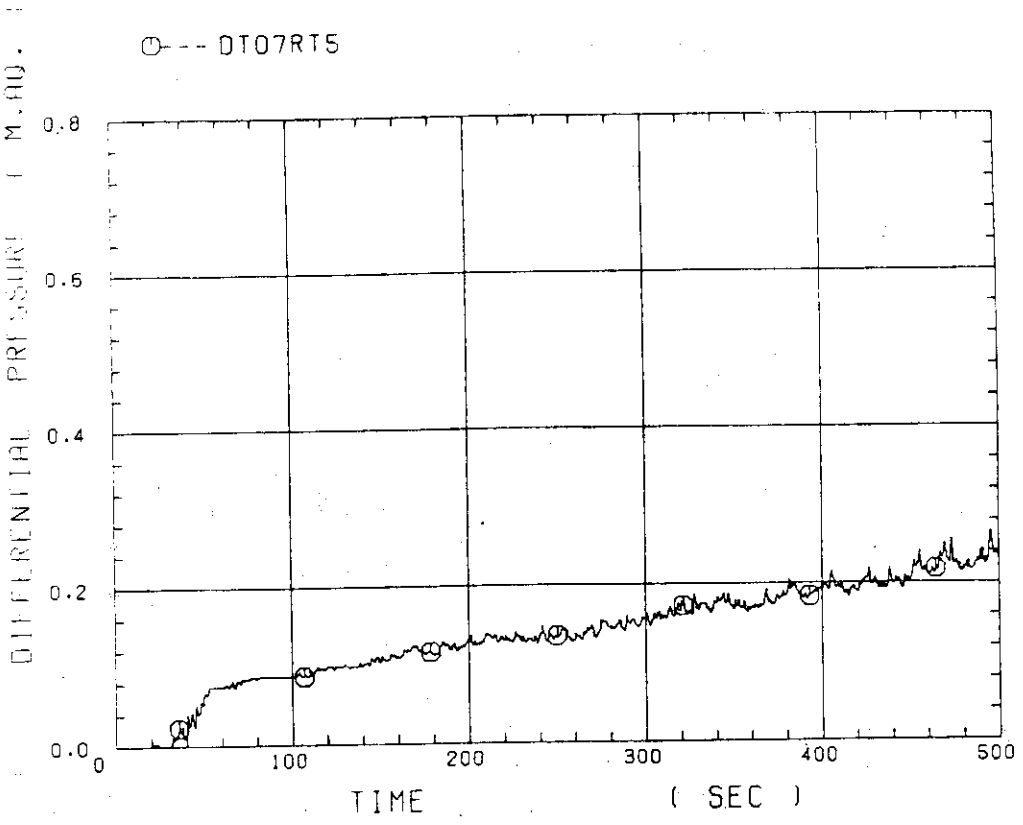

Fig. C-25 Differential pressure through upper plenum

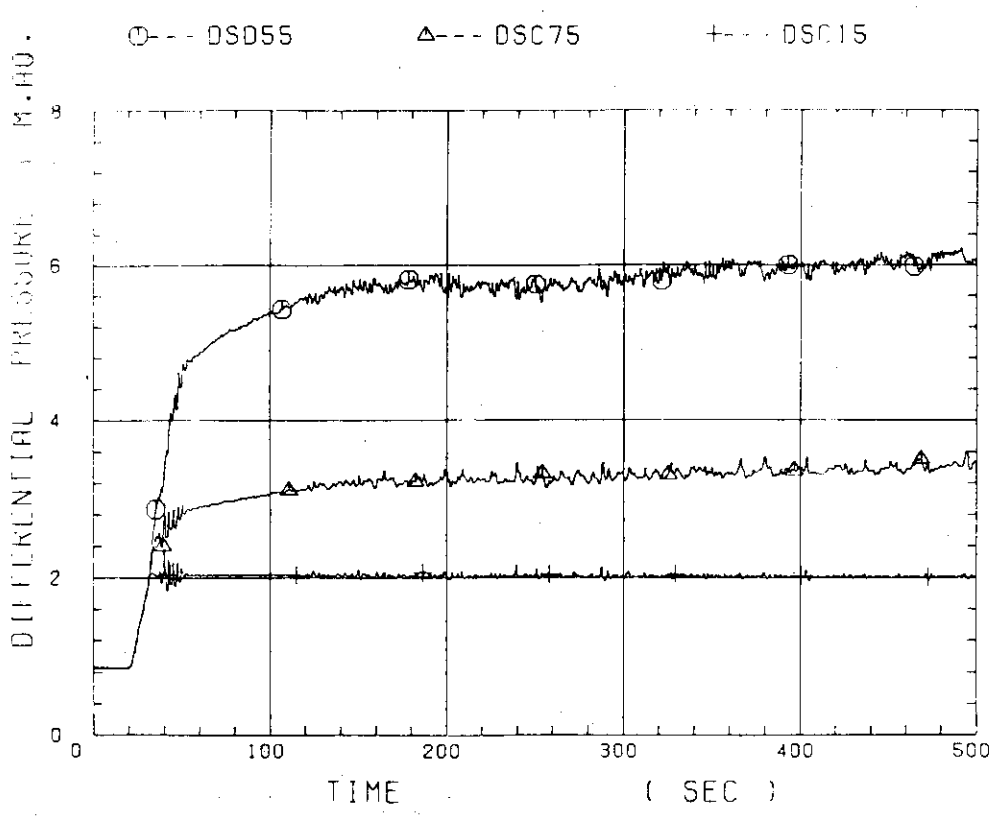

Fig. C-26 Differential pressure through downcomer, core, and lower plenum

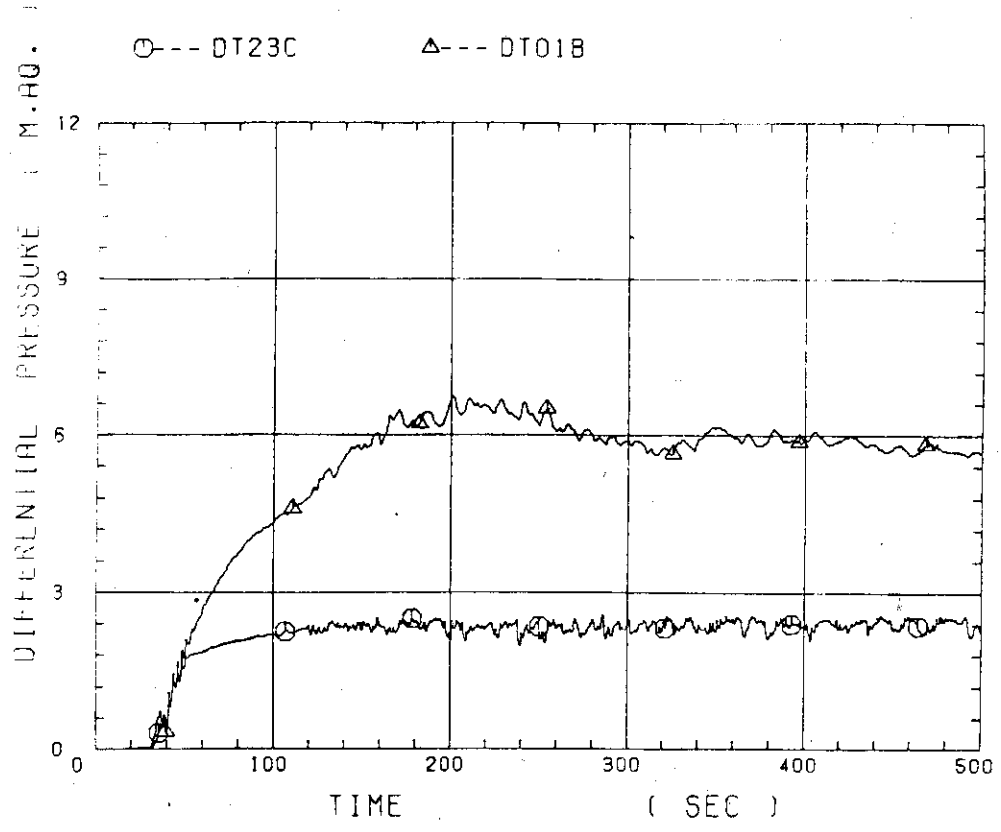

Fig. C-27 Differential pressure through intact and broken loops

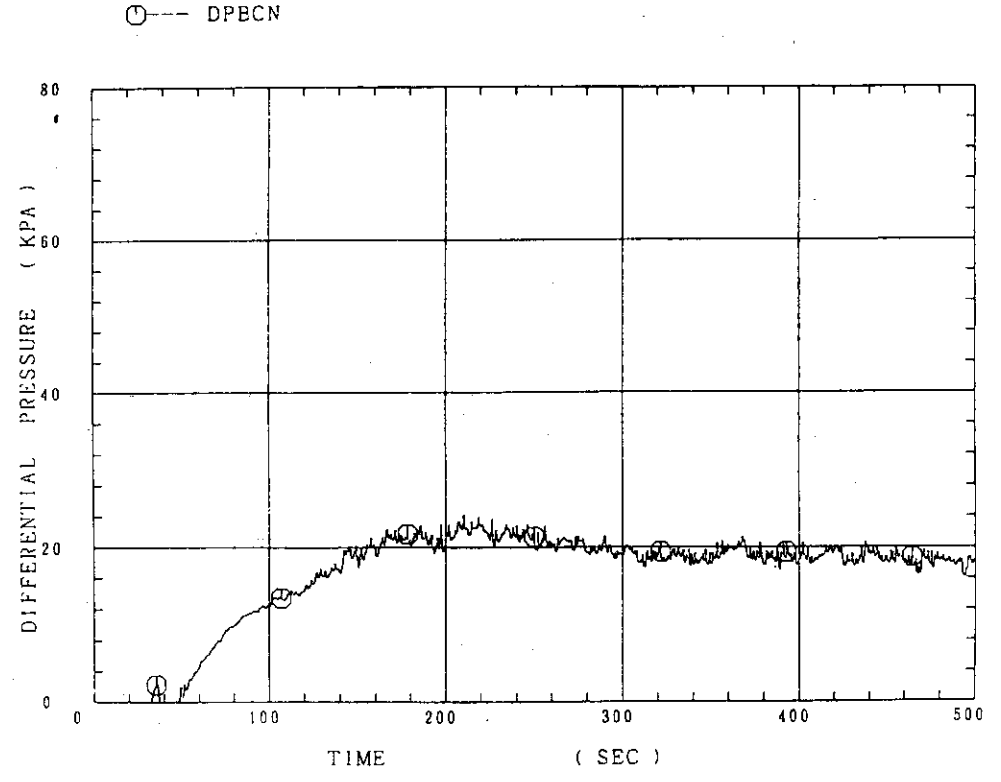

Fig. C-28 Differential pressure through broken cold leg nozzle

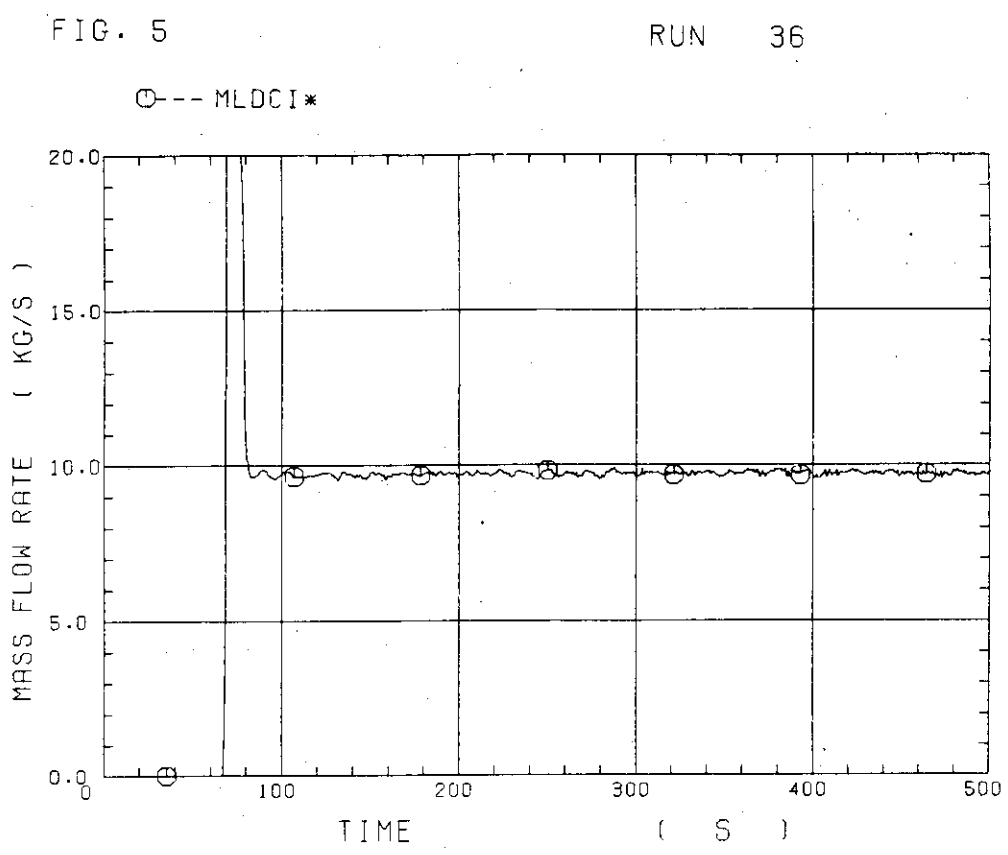

Fig. C-29 Total water mass flow rate from intact loops to downcomer

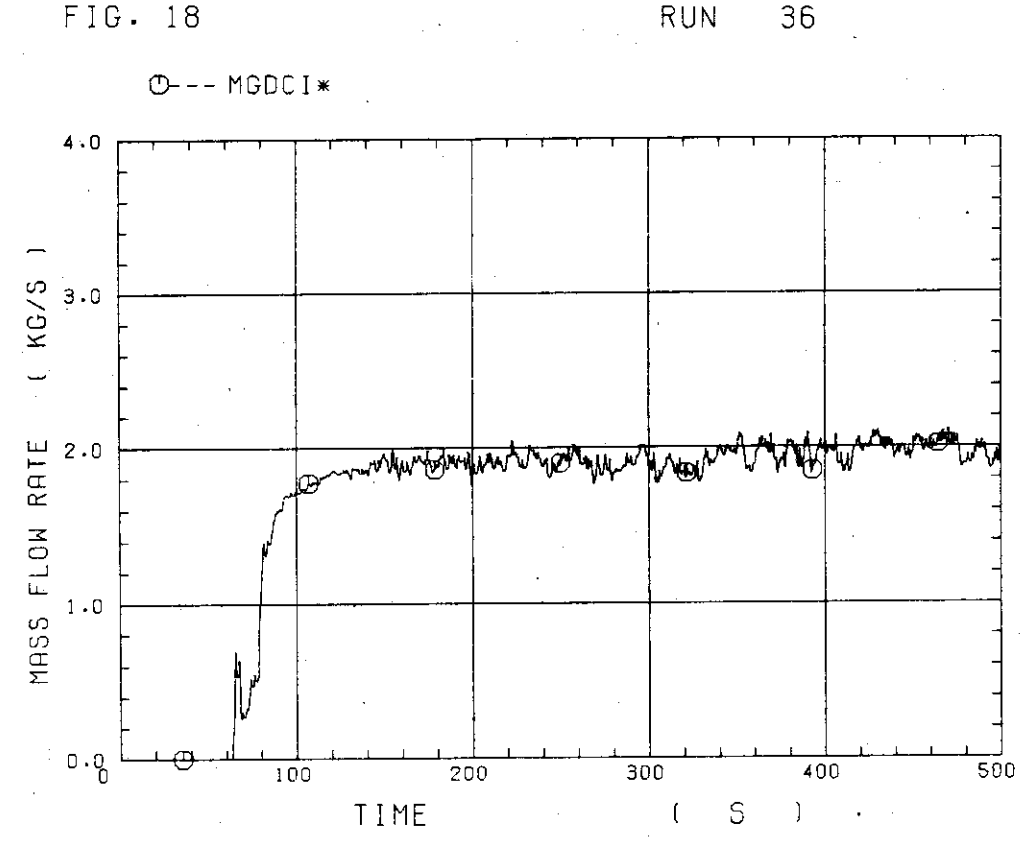

Fig. C-30 Total steam mass flow rate from intact loops to downcomer

FIG. 6 RUN 36

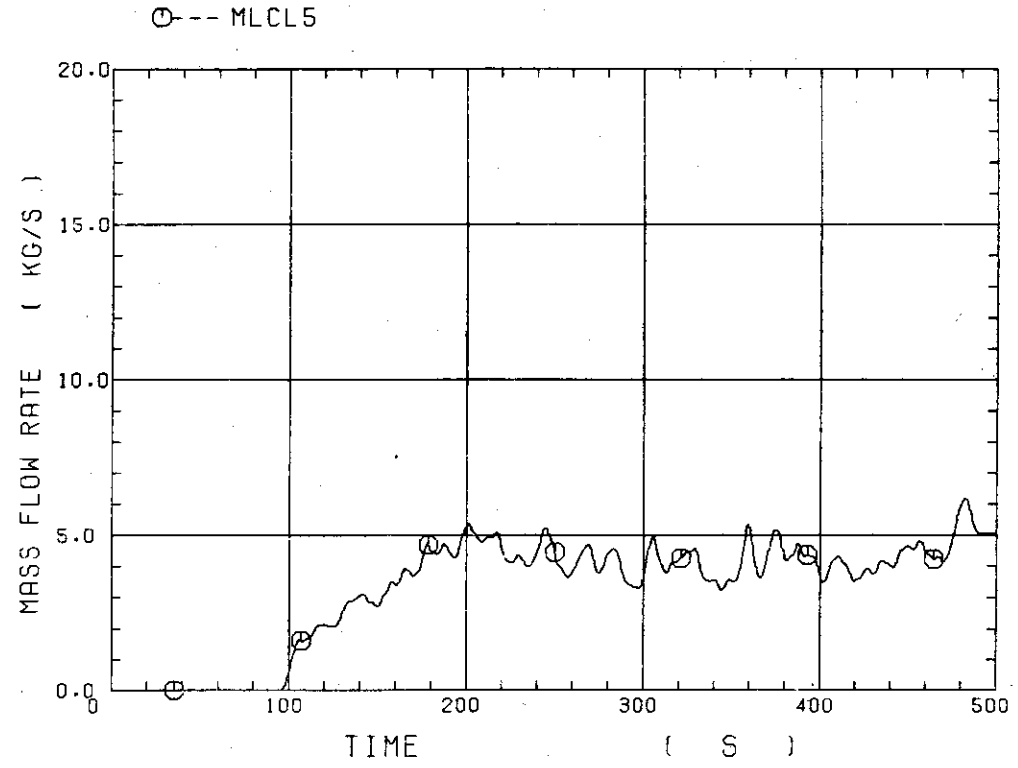

Fig. C-31 Water mass flow rate through broken cold leg nozzle

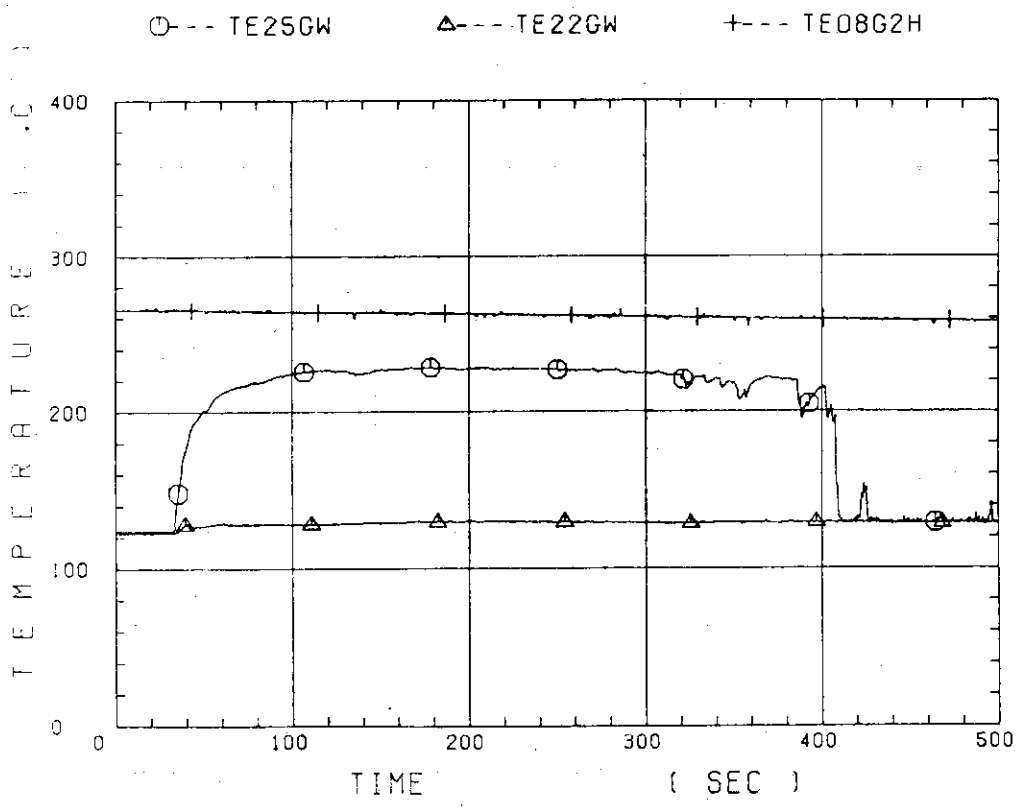

Fig. C-32 Fluid temperature in inlet plenum, outlet plenum, and secondary of steam generator 1

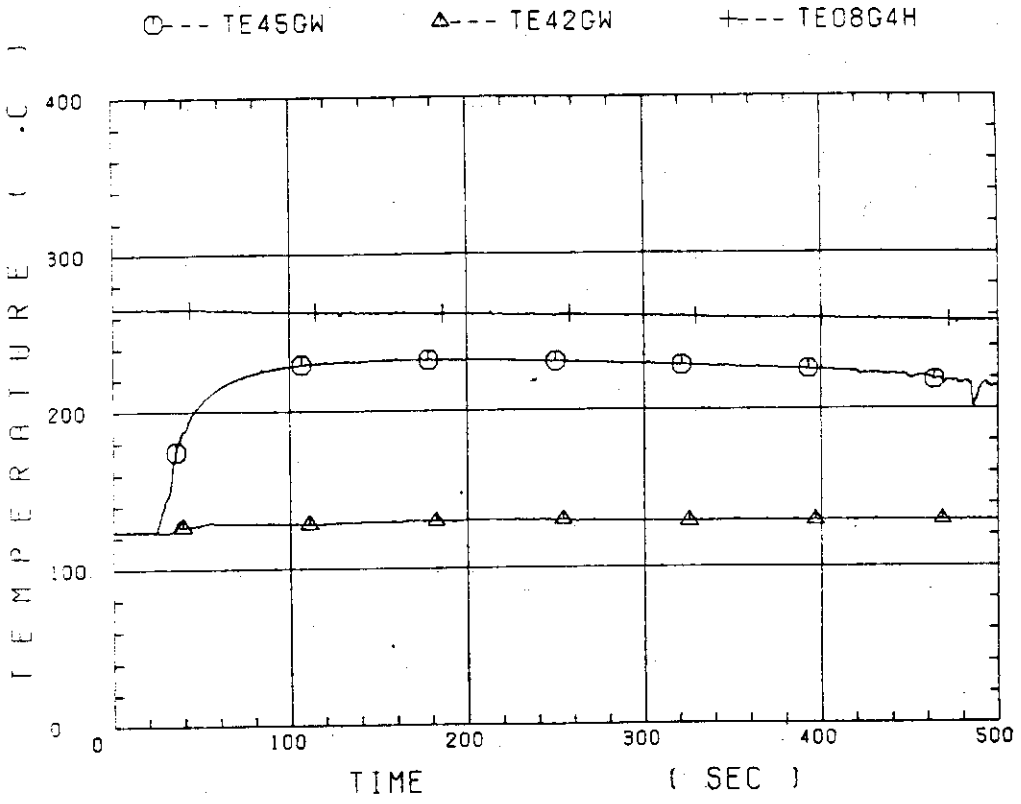

Fig. C-33 Fluid temperature in inlet plenum, outlet plenum, and secondary of steam generator 2

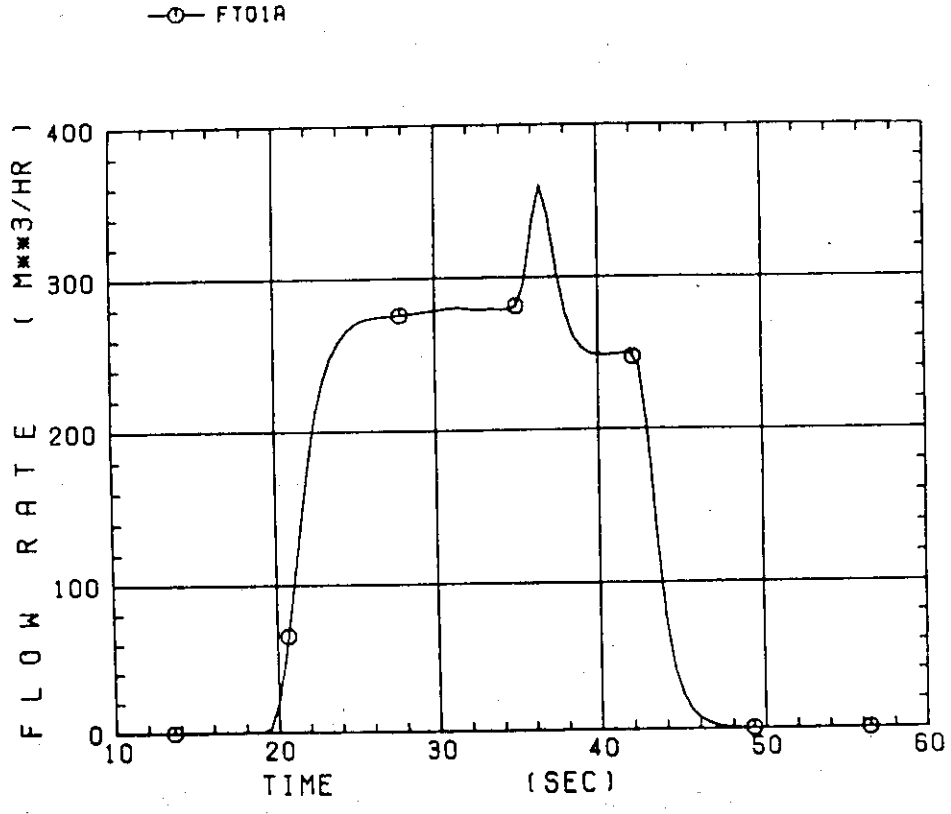

Fig. C-34 Total accumulator injection rate

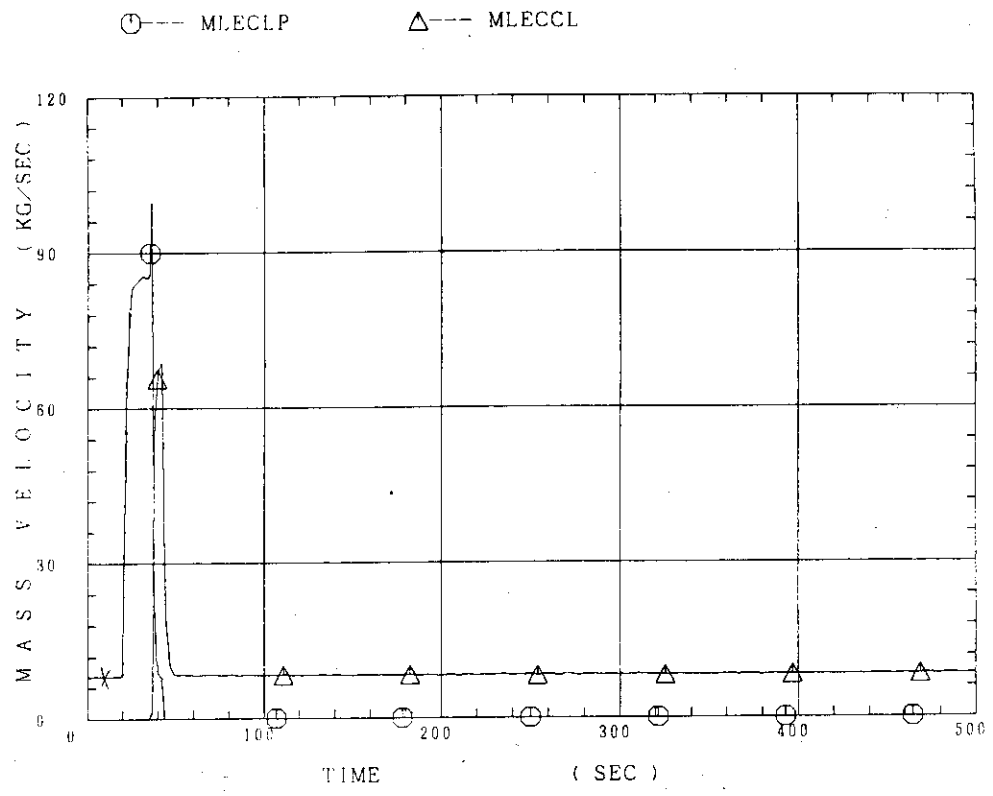

Fig. C-35 ECC water injection rates to lower plenum and to cold legs

Appendix D

Evaluation of core flooding mass flow rate

Figure list

The reflood phenomena is a relatively slow transient and is assumed to be a steady state condition. In a steady state condition, based on the mass balance relations of the system, the core flooding mass flow rates m_{FS} can be written as follows:

By using the data measured at the downstream of the core inlet, m_F is derived as,

$$\dot{m}_F = \dot{m}_C + \dot{m}_U + \dot{m}_B + \dot{m}_I, \tag{1}$$

where $\dot{m}_C$ and $\dot{m}_U$ are the mass accumulation rates in the core and the upper plenum respectively. The $\dot{m}_B$ and $\dot{m}_I$ are the mass flow rates in the broken loop and the intact loop, respectively.

By using the data measured at the upstream of the core inlet, $\dot{m}_F$ is derived as,

$$\dot{m}_F = \Sigma\dot{m}_{DL} - \dot{m}_D - \dot{m}_O + \dot{m}_{ECC/LP} , \tag{2}$$

where $\dot{m}_{DL}$, $\dot{m}_O$ and $\dot{m}_{ECC/LP}$ are the mass flow rates of the water flowing into and overflowing from the downcomer and the mass flow rate of the ECC water injected into the lower plenum, respectively.

The $\dot{m}_I$s and $\dot{m}_B$ can be obtained from the pressure drops at the pump simulators with orifices by accuming the K-factor of the orifice is constant or from the data of Pitot tubes. The values of $\dot{m}_C$, $\dot{m}_D$ and $\dot{m}_U$ can be evaluated with the differential pressure ΔP_C, ΔP_D and ΔP_U, respectively, as follows:

$$\dot{m}_n = d(\Delta P_n S_n/g)/dt \quad (n : C, D, U) , \tag{3}$$

where g is the gravitational acceleration and S_n is the cross sectional area. The value of $\dot{m}_O$ can be obtained from the liquid level X in the Containment tank 1 as,

$$\dot{m}_O = d(X\rho_\ell S_O)/dt , \tag{4}$$

where ρ_ℓ is the liquid density and S_O is the cross sectional area of the containment tank 1.

The value of $\dot{m}_{DL}$ is obtained from the following mass and energy

balance relations at each ECC port under the assumption of thermal equilibrium:

$$\dot{m}_{DV} + \dot{m}_{DL} = \dot{m}_{ECC} + \dot{m}_{I} \quad , \tag{5}$$

$$(\dot{m}_{DV} + \dot{m}_{DL})i = \dot{m}_{ECC} i_{ECC} + \dot{m}_{I} i_{I} \quad , \tag{6}$$

$$\left.\begin{array}{lll} \text{if} \quad i_g \geq i \geq i_\ell \quad , & (\dot{m}_{DV} + \dot{m}_{LD})i = \dot{m}_{DV} i_g + \dot{m}_{DL} i \\ \text{if} \quad i > i_g \quad , & m_{DL} = 0 \quad , \\ \text{if} \quad i < i_\ell \quad , & m_{DV} = 0 \quad , \end{array}\right\} \tag{7}$$

where i is enthalpy of fluid and i_ℓ and i_g are enthalpies of liquid and steam at the saturation temperature, respectively.

The fluid temperatures can be measured with thermocouples immersed in the fluid and the enthalpies i_I, i_{ECC} can be estimated.

Mass balance calculations were performed with Eqs. (1) and (2), since it was found that the water entering the steam generator was completely evaporated. In the differentiation, higher frequency components of the data tends to be amplified more. Therefore, in the differentiation of the differential pressure data, the smoothing procedure was used to suppress the high frequency components of the data. Figures D-1 and D-4 show the flooding mass flow rates, $\dot{m}_F$s, calculated from Eqs. (1) and (2) by averaging data in 20 seconds for tests C1-17 (Run 36) and C1-20 (Run 20), respectively.

In the Acc injection period, the calculated values, $\dot{m}_F$s, are significantly different from each other. This discrepancy may be caused by in-accuracy of the mass flow rate injected into the system and by the unaccounting of the storage of water in the cold leg pipe. The former might be introduced from the slow time response (time constant 1 second) and the change of the gas volume in the injection line. In this period, specially before the steam generation from the core became noticable, the mass flow rate, $\dot{m}_F$, calculated with Eq. (1) is reasonable, since the calculation needs the increasing rates of the masses in the core and the upper plenum and their accuracy is enough for our estimation.

In the LPCI injection period, the calculated values, $\dot{m}_F$s, are slightly different from each other. Judging from the time-integral values of both $\dot{m}_F$s, their average values are nearly proportional. The discrepancy was inferred to be caused by the disregard of the bypass of steam and liquid from the upper plenum without going through the hot legs in the calculation with Eq. (1). And additionally the discrepancy was caused by the disregard of the steam generation in the downcomer due to the hot wall of the pressure vessel in the calculation with Eq. (2). It was estimated that the disregard of the downcomer steam generation was caused the error of 0.25 kg/s on predicted $\dot{m}_F$. The estimation was made by comparing the results of the tests with hot and cold downcomer conditions. In the LPCI injection period except for the early period, the mass flow rate, $\dot{m}_F$, calculated with Eq. (2) is reasonable, since the error from the injected ECC flow rate measurement is negligible under the quasi-steady state condition appeared in this period and the error caused by the steam generation in the downcomer is small.

In order to obtain the best estimate core inlet mass flow rate, the calculation with Eq. (1) were performed by using the corrected values of

the loop mass flow rates, $\dot{m}_I$s and $\dot{m}_B$. The correction was made by multiplying $\dot{m}_I$s and $\dot{m}_B$ by a factor which yields identical $\dot{m}_F$s in the calculations with Eqs. (1) and (2). Figures D-2 and D-5 show the best estimate core inlet mass flow rate. In this calculation, the smoothing procedure was performed by averaging $\dot{m}_F$ in 10 seconds for tests C1-17 (Run 36) and C1-20 (Run 39), respectively. Therefore the core inlet velocity at the reflood initiation was slightly lowered. Since the by-pass of steam and water from the upper plenum is difficult to be evaluated quantitatively, this estimation involves at greatest about 15 % error. The relation between the integral core-flooded water mass evaluated with Eqs. (1) and (2) and best-estimated are shown in Figs. D-3 and D-6 for tests C1-17 (Run 36) and C1-20 (Run 39), respectively.

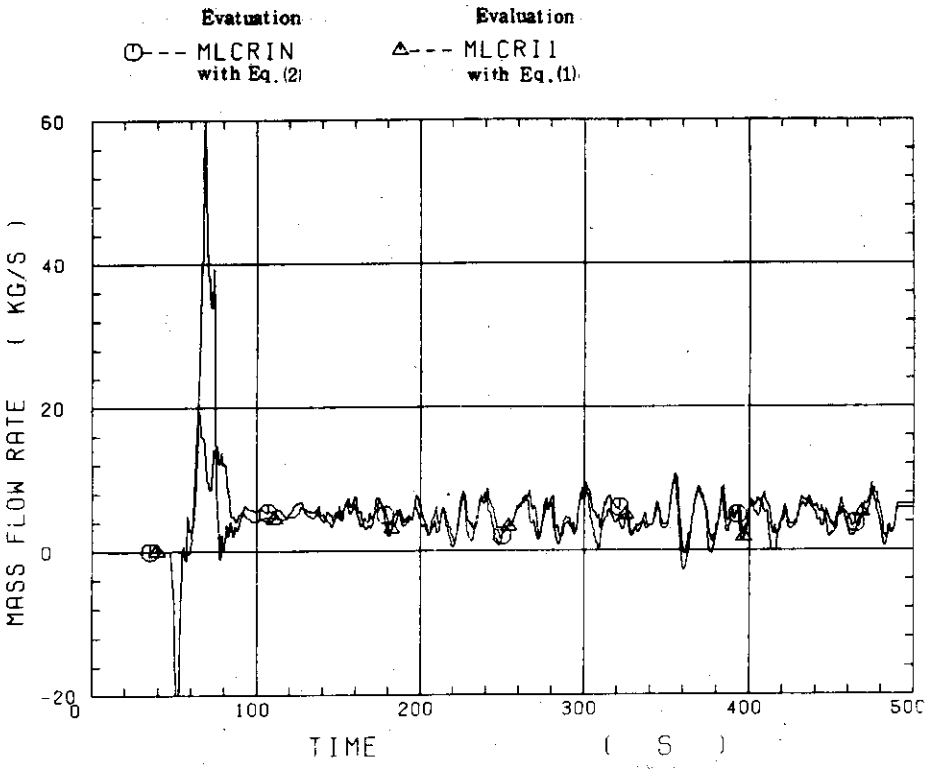

Fig. D-1 Core flooding mass flow rates evaluated with Eqs. (1) and (2) for C1-17 (Run 36)

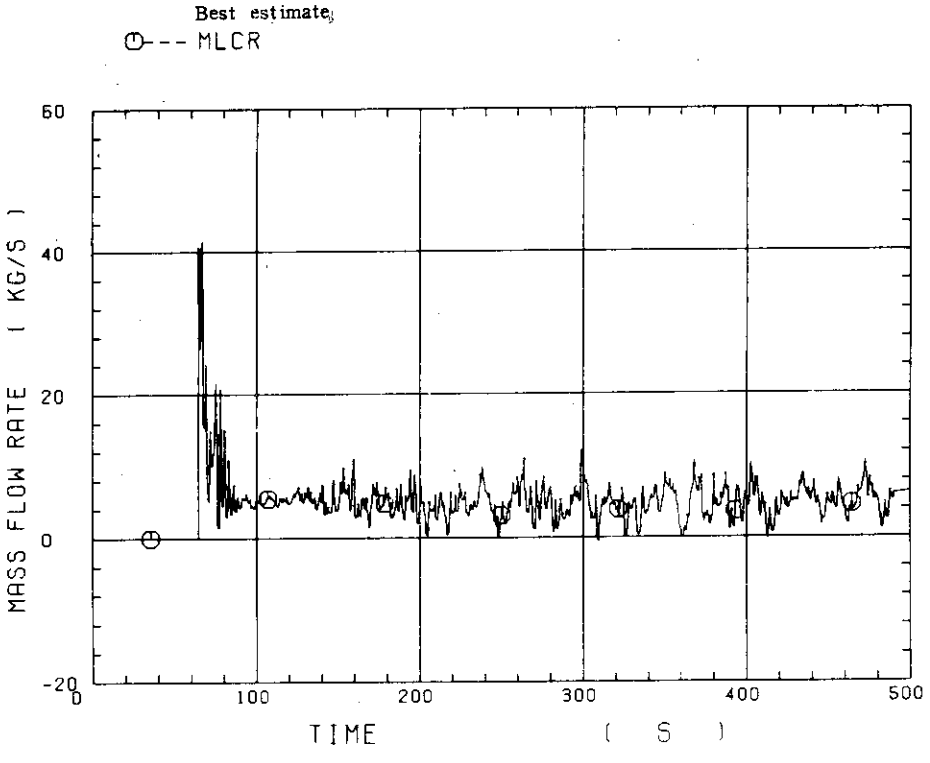

Fig. D-2 Best estimate core flooding mass flow rates for C1-17 (Run 36)

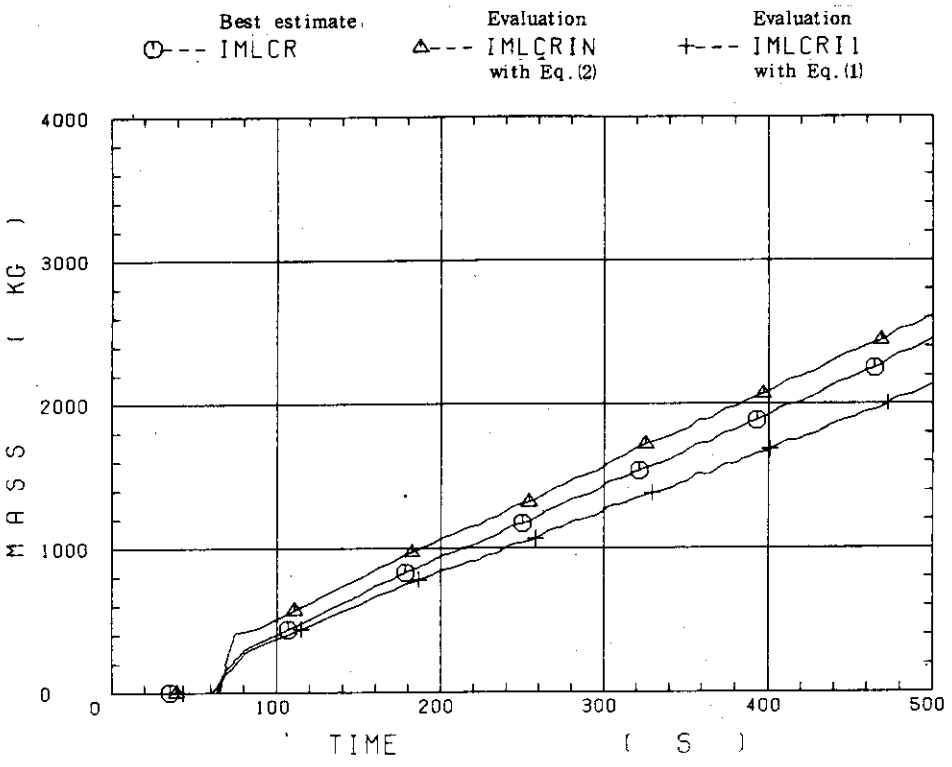

Fig. D-3 Integral masses flooded into core evaluated with Eqs. (1) and (2) and best-estimated for C1-17 (Run 36)

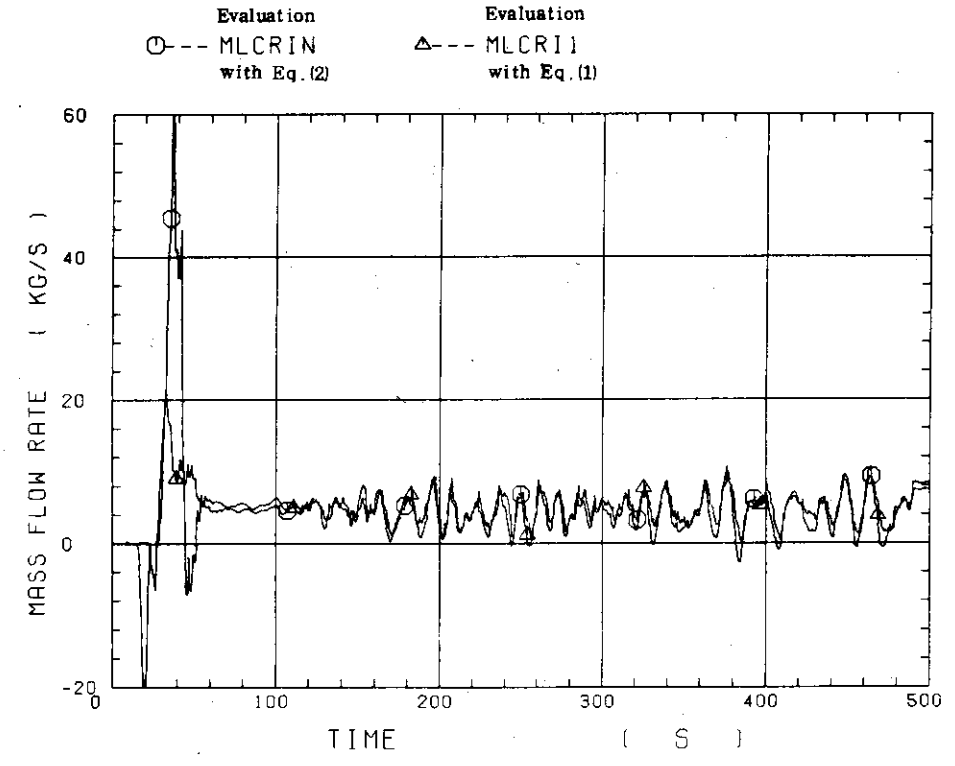

Fig. D-4 Core flooding mass flow rates evaluated with Eqs. (1) and (2) for C1-20 (Run 39)

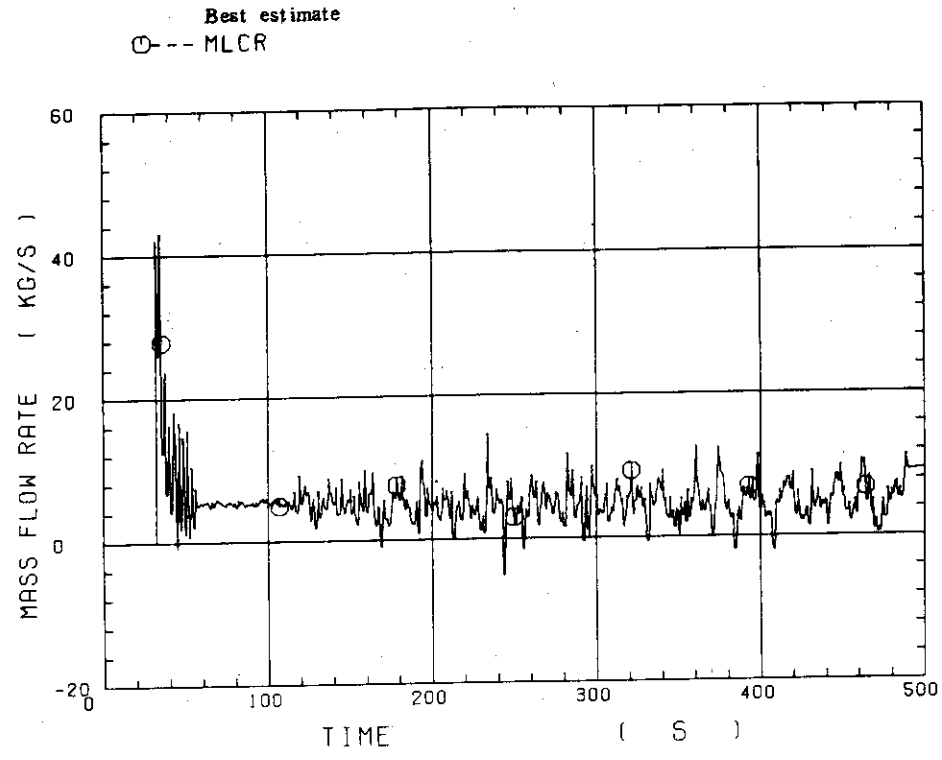

Fig. D-5 Best estimate core flooding mass flow rates for C1-20 (Run 39)

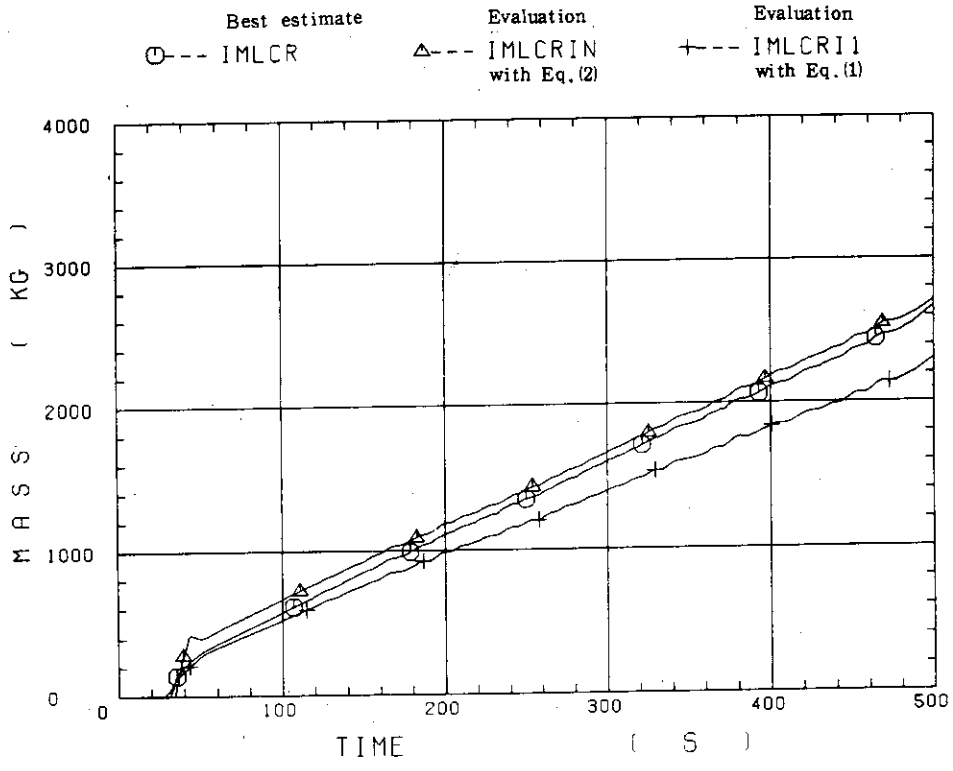

Fig. D-6 Integral masses flooded into core evaluated with Eqs. (1) and (2) and best-estimated for C1-20 (Run 39)